MODELING OF INERTIAL PARTICLE FLOW AND ENTRY GAS FLOW IN MICRO-CHANNELS

A THESIS

SUBMITTED TO

THE GRADUATE SCHOOL OF ENGINEERING AND SCIENCE

OF BILKENT UNIVERSITY

IN PARTIAL FULFILLMENT OF THE REQUIREMENTS

FOR THE DEGREE OF

MASTER OF SCIENCE

IN

MECHANICAL ENGINEERING

By

Reza RASOOLI

January, 2017

I certify that I have read this thesis and that in my opinion it is fully adequate, in scope and in quality, as a thesis for the degree of Master of Science.

Barbaros Çetin(Advisor)

I certify that I have read this thesis and that in my opinion it is fully adequate, in scope and in quality, as a thesis for the degree of Master of Science.

Assist. Prof. Dr. E. Yegân Erdem

I certify that I have read this thesis and that in my opinion it is fully adequate, in scope and in quality, as a thesis for the degree of Master of Science.

Prof. Dr. Zafer Dursunkaya
Middle East Technical University

Approved for the Graduate School of Engineering and Science:

Prof. Dr. Ezhan Karaşan
Director of the Graduate School

ABSTRACT

MODELING OF INERTIAL PARTICLE FLOW AND ENTRY GAS FLOW IN MICRO-CHANNELS

Reza RASOOLI
M.S. in Mechanical Engineering
Supervisor: Barbaros Çetin
January, 2017

Microfluidics is integration of micro-fabrication techniques together with the knowledge of flow behavior at micro scale to design and achieve particle manipulation, separation, sorting and etc. which is important for biomedical and biological applications. In this regard, analytical and numerical analysis and modeling play an important substantial role and serve as a basis for further and better understanding of basic and fundamental concepts and create a more transparent picture for an optimized design with desired properties. In the present thesis, behavior of both liquid type and gas type working fluid have been studied. For the liquid flow, finite Reynolds number flow regimes which is also known as inertial microfluidics has been considered. Inertial microfluidics have exhibited promising and rigorous abilities in size based particle separation due to existence of inertial lift force and secondary flow (for curved channels). For the gas flow, governing equations of an incompressible and isothermal flow have been analytically solved using a linearization technique proposed in the literature for the hydrodynamic entrance region due to its importance for excess pressure drop and heat transfer. For this purpose, simulation of particle focusing using Lagrangian particle tracking method has been carried out for both straight and spiral micro-channel. For simulation authentication, experimental investigation have also performed and compared with the simulation upshots.

Keywords: Microfluidics, Slip-flow, Langhaar solution, Inertial microfluidics, Lagrangian tracking method.

ÖZET

MİKRO-KANALLARDA ATALETSEL PARÇACIK AKIŞI VE GİRİŞ GAZ AKIŞI MODELLEMESİ

Reza RASOOLI
Makine Mühendisliği, Yüksek Lisans
Tez Yöneticisi: Barbaros Çetin
Ocak, 2017

Mikro-akışkanlar-dinamiği biyomedikal ve biyolojik uygulamalar için önemli olan parçacık manipülasyonu, ayrılması, sınıflandırılması vb. işlemlerin tasarlanması ve başarılamsı için mikro-üretim ve mikro-ölçekte akış davranış bilgisinin birleştirilmesidir. Bu bağlamda daha optimize sistemlerin tasarlanabilmesi ve temel kavramların daha iyi anlaşılması için analitik ve sayısal analiz ve modelleme çok önemli bir rol oynar. Bu tez çalışmasında, hem gaz hem de sıvı akışkanlar için modelleme teknikleri çalışılmıştır. Gaz akış için sıkıştırılamaz ve izotermal kanal akışı, hidrodinamik giriş bölgesi için analitik olarak lineerizasyon kullanarak çözülmüş ve girişi bölgesindeki basınç düşümü hesaplanmıştır. Sıvı akış modellemesinde ise ataletsel mikro-akışkanlar-dinamiği olarak bilinen sonlu Reynolds sayısı akış rejimi problemi ele alınmıştır. Ataletsel mikro-akışkanlar-dinamiği, kanal içerisinde oluşan ikincil akışlar ve parçacık üzerinde ortaya çıkan kaldırma kuvvetinin etkisi ile parçacıkları boyutlarına göre ayırma kabiliyetine sahiptir. Bu amaçla, Lagrange izleme yöntemi kullanılarak mikro-kanal içerisinde ataletsel mikro-akışkanlar-dinamiği uygulamarı için parçacık hareketinin modellenebildiği bir sayısal model geliştirilmiştir.

Anahtar sözcükler: Mikro-akışkanlar-dinamiği, kayan-akış, Langhaar çözümü, ataletsel mikro-akışkanlar-dinamiği, Lagrange izleme yöntemi.

Acknowledgement

First of all, I would like to thank my advisor Assist. Prof. Dr. Barbaros Cetin for his guidance, advice and patience during my master study. Undoubtedly, it was a great opportunity for me to work with him and develop my research skills under his supervision for further educational purposes and career.

I express my gratitude to every one who supported me throughout my Master: Dr. Göksel Durkaya, Mr. Hussein Kurtuldu and Dr. Besim Baranoğlu. I am grateful to them for helping and sharing their illuminating views.

Financial support from the Turkish Scientific and Technical Research Council (Grant No. 114M597) regarding the inertial microfluidics aspect of this thesis work is greatly appreciated.

I thank my friend Mr. Arsalan Nikdoost for helping in fabrication process, Mr. Hossein Alijani, Mohammad Asghari and Umutcan Çalışkan for laboratory training. My warmest thank goes to my real friend Masoud Ahmadi for his priceless spiritual supports throughout my hard moments.

Last but not the least, I would like to thank the special people of my life: my mother (Mahin), my father (Ahmad Reza), my brothers Masoud and Davood for their supports. At the end, I would like to thank the love of my life and the meaning and motivation of my life Hamide.

Contents

List of Figures

List of Tables

Chapter 1

Introduction

Tremendous advances in fabrication of micro and nano chips, have enabled scientists and researchers to discover a bunch of interesting phenomena occur at micro- and nano-scale. Implementation and application of these phenomena is another interesting story which researchers have performed in recent decades. For better understanding the concepts and fundamentals at micro-scale, analytical and numerical modeling play an important substantial role and serve as a basis for having a better design with optimum and desired properties.

The modeling of liquid and gas flows quite different. Typically, liquid flows are encountered in microfluidic systems for biomedical applications [1]. Although the fluid flow modeling is via conventional laminar form of Navier-Stokes equations, the flow can be generated with electrical field and/or the fluid itself may contain some bio-particles. The flow modeling can easily be coupled by another physic and/or the effect of the bio-particles on the flow field needs to be considered. On the other hand, for gas flows, neither the coupling with another physic nor the bio-particle presence is not typical. However, there are other additional effects such as rarefaction and compressibility that needs to be considered [2].

1.1 Particle Flow

The major application area of the particle flow in micro-channels is the microfluidic devices for biomedical applications (i.e. lab-on-a-chip) devices [1]. The flow speed is relatively low, therefore the flow is generally in the Stoke's flow regime if not laminar. Moreover, the flow can be induced by an electric field (electro-osmotic flow) and/or there may present an external flow field such as electric, acoustic, magnetic etc. To manipulate particle inside micro-channel. Therefore, the flow field may need to be solved with the presence of particle inside the micro-channel and/or with the presence of a coupled physic such as electro-magnetic, acoustic and/or optics. To come up with the optimum channel geometry and the operating conditions, on top of the flow field, the major interest is the bio-particle trajectory within the micro-channel in the design process of these microfluidic devices. There are basically two common approach for the simulation of particle motion inside a micro-channel:

(i) Point-particle approach: In this approach, the particles are treated as point particles, and Newton's Second Law motion is written for a point particle, and the force balance equation should be integrated which is known as Lagrangian discrete phase method (LDPM) (also known as Lagrangian tracking method or force balance integration). In this method, the volume fraction of particles needs to be less than 10% which dictates a dilute particulate solution. The field equations (flow, electric, acoustic etc) are solved without the presence of the particle. The forces acting on the particle is calculated using pre-derived equations based on the value of the field variables at the center location of the particle. Despite the ignorance of some these important effects such as particle-particle interaction, particle-wall interaction, rotational dynamics of the particle (all of which become negligible if the particle concentration is dilute), LDPM has been applied for the simulation of particle motion in the literature for both dielectrophoretic [3–9] and acoustophoretic applications [10, 11]. This approach does not require relatively high computational cost. The field variables can be obtained without the presence of the particle, and the particle trajectories can be evaluated at the post-processing step. Therefore, LDPM may allow statistical

analysis for the motion of many particles [10, 11].

(ii) Finite-sized particles: In this approach, the field variables are solved with the presence of the finite-sized particle. The field variables have to be re-calculated for each incremental movement of the particle. If small enough mesh is used, the particle-wall and particle-particle interactions can be captured with physical basis. Once the field variables are obtained with the presence of finite particle size, the stress tensor on the particle surface can be obtained and integrated to obtain the total force and moment acting on the particle. Although these forces needs to be known *a priori* for LDPM, in finite-sized particle approach these forces are the result of the computation. However, this approach challenging and computationally expensive. In general, the stress induced on the particle surface is the function of the gradient of the field variable which requires the determination of these filed gradient with high accuracy on the particle surface to be able to determine the force induced on the particle. Although numerical techniques based on domain meshing such as finite element and finite volume are challenging to capture the physics of the particle-particle interaction and the movement of the particle within the domain, several researchers have implemented different techniques such as arbitrary Lagrangian-Eulerian method [12–15], immersed interface method/immersed boundary method [16–18], fictitious domain method [19,20], sharp interface method [16–18] to apply finite-sized particles in a relative simple simulation settings. Recently, boundary element method (BEM), which is a numerical technique based on boundary discretization and does not need re-meshing as the particle moves in a micro-channel has been implemented for particulate flow in micro-channels [9, 21–25].

1.2 Inertial Microfluidics

Among other bio-particle manipulation techniques, hydrodynamic techniques are very convenient and robust considering size-based manipulation since they do not require sophisticated hardware [1]. Typically, the Reynolds number in conventional hydrodynamic based microfluidic applications is in the order of $10^{-2} - 1.0$

which dictates Stoke's flow and streamlines parallel to the channel walls. However, when Re reaches unity and beyond, the inertial effects come into picture and the flow characteristics changes. This regime is known as inertial microfluidics. In this regime, the flow streamlines no longer follows the solid walls and some secondary flows begin to occur within the channel which induces lift drag and forces on the particles flowing in the channel. The balance of these forces dictates motion of particles at some certain locations (both in the lateral and height direction) [26]. Likewise other hydrodynamic techniques, particle manipulation based inertial microfluidics is a passive technique which has many advantages such as simplicity, label free nature. Moreover, due to the relatively high Re nature automatically requires a high flow rate which leads to a ultra high-throughput (bio-particles processed per unit time) which is a very critical issue when the clinical applications where huge number of bio-particles need to be processed [1].

Regarding the simulation of the particle motion for inertial microfluidic, finite-sized particle approach is not an option considering the length scale of the problem. Typically the length over diameter ratio greater that 100, and the mean velocity of the flow is high and the velocity of the particle is high (i.e. particle travels couple hundred diameter distance per unit time). Therefore, LDPM becomes the only option for these kind of simulations. However, the bottom-neck of the LDPM is the requirement for the pre-defined expressions for the forces induced on the particle. Although there are several studies in the literature using inertial microfluidics for the sized-based manipulation, more specifically separation, in the literature [27–41], majority of the studies are experimental with a design process based on some order of magnitude estimates [27–29, 31–34, 36–38, 41], and few studies presents a computational model using some derived expressions from the literature for the induced forces [30, 35, 39, 40, 42, 43]. Although early studies considers very simple 2D models [44], with the burst of the recent studies on the topic, researchers have recently developed some computational models to predict induced forces on the particle as a result of the inertial effects in a 3D micro-channel set-up [39, 40, 42, 43]

1.3 Gas Flow

Micro-channels and micro-tubes are inseparable part of microfluidic devices and play a crucial role which necessitates the fundamental knowledge of flow behavior at micro-scale for the effective and optimal design of these devices. Many theoretical investigations have been made on the physics of fluid flow in channels and ducts at micro-scale [45–47]. The important effect considered at the micro-scale is the rarefaction. As the characteristic length (L) of the flow approaches to the mean-free-path (λ) of the fluid, the continuum approach fails to be valid, and the fluid flow modeling moves from continuum to molecular model. The rarefaction is characterized by the Knudsen number ($Kn = \lambda/L$). Continuum hypothesis applies for $Kn \lesssim 10^{-3}$. For $10^{-1} \lesssim Kn \lesssim 10$, the regime is known as transition regime in which continuum equations fail to model the fluid flow. Molecular models such as DSMC and MD or solutions of Boltzmann Transport equation is required. The regime where $10^{-3} \lesssim Kn \lesssim 10^{-1}$ is the slip-flow regime in which the continuum equations needs to be modified through the velocity-slip and temperature-jump boundary conditions to take into account the molecular interaction of the fluid particles with the walls within the Knudsen layer [45].

The general form of the velocity-slip boundary condition for an isothermal flow can be written as following a non-dimensionalization with a reference length and velocity scale as [47–50]:

$$U_s - U_{wall} = A_1 \mathrm{Kn} (\partial_n U)_{wall} + A_2 \mathrm{Kn}^2 (\partial_n^2 U)_{wall}, \tag{1.1}$$

where $(\partial/\partial n)$ is the gradient in the normal direction of the wall, A_1 and A_2 are the slip-coefficients. Many researchers suggest the use of different coefficients based on some theoretical considerations [48, pp. 74]. For a fully-diffuse reflection, the proposed coefficients in the literature are tabulated in Table 1.1.

The first term is called as the Maxwell's first-order slip, and the inclusion of the second-term turns the boundary condition to a second-order one. The approximation of the Boltzmann Transport equation up to $\mathcal{O}(Kn)$ (i.e. first order in Kn) results in compressible form of the Navier-Stokes equations which

Table 1.1: Coefficients for different slip models

Model	$\mathbf{A_1}$	$\mathbf{A_2}$
First-order Model	1.0	0
Schamberg Model	1.0	$-5\pi/12$
Cercignani Model	1.1466	–0.9756
Deissler Model	1.0	$-9/8$
Hsia Model	1.0	$-1/2$
Mitsuya Model	1.0	$-2/9$

require only first-order boundary conditions. The second-order models for second-order equations such as Burnett and Woods equations. However, researchers showed that the use of the second-order boundary condition with the first-order Navier-Stokes equations [46,51,52] or first-order Maxwell boundary condition with second-order quasi-hydyrodynamic equations [46] may extend the applicability of the slip-flow regime up to Kn ≈ 0.25.

The second-order term may introduce some numerical difficulties regarding the accurate calculation of the high-order derivatives, especially for complex geometries [48]. Therefore, some researchers introduced higher-order accurate boundary conditions which include only first-order derivatives [2, 53]. Beskok and Karniadakis [2] proposed a general velocity-slip boundary condition as (for a diffuse reflection of gas molecules):

$$U_s - U_{wall} = \frac{\mathrm{Kn}}{1 - b\mathrm{Kn}}(\partial_n U)_{wall}, \tag{1.2}$$

where b is a general slip coefficient. Strictly speaking parameter b is a function of Kn. For a general choice, (1.2) is first-order in Kn. However, for a specific choice of the parameter b, the boundary condition can be transform into a second-order one. For the slip-flow regime, [2] derived a condition to ensure the second-order accuracy of (1.2) as:

$$b = \left(\frac{1}{2}\frac{\partial_n^2 U_o}{\partial_n U_o}\right)_{wall}, \tag{1.3}$$

where U_o is the velocity-profile corresponds to the no-slip case (i.e. $Kn = 0$). Our model exploits incompressible assumption for the gas flow. However this assumption may seem not realistic for a gas flow, for Mach number less than 0.3 the

gas flow can be treated and modeled as incompressible [54]. On the other hand, entrance effects come into picture for short length micro-channels (length over diameter is not significantly high). Moreover, for short length micro-channels, the ratio of outlet to inlet pressure is small which confirms using incompressibility assumption. Altogether, our model is appropriate for gas flows with Mach number less than 0.3 which ensures incompressibility of gas behaviour and also for the short length micro-channels with low ratio of inlet/outlet pressure.

1.4 Objectives and Motivation

The mission of the present thesis is devoted to study two important topics in microfluidics which fill a gap in the literature. Inertial microfluidics and entry gas flow are two topics that will be studied in the present thesis. In the first part of the thesis, a general computational model for particle tracking in inertial microfluidics is developed. This computational model exploits Lagrangian discrete phase model (LDPM) which is an easy-to-use model with a clear structure. The flow field is treated as a continuum phase and the particles are introduced as a discrete phase. This model is based on the force balance integration for the discrete phase which necessitates the knowledge of all force fields acting on the discrete phase. Most of the studies performed in the literature are based on experimental observation and some order-of-magnitude for the channel design. This study develops a general computational model that can be applied in inertial microfluidics to find the optimized channel geometry with desired properties. The second part is dedicated to investigate the gas flow behavior at the hydrodynamic entrance of micro-channels. An analytical solution of a 2D incompressible, isothermal flow in a developing region of a micro-channel considered both in cylindrical and cartesian coordinates based on Langhaar's linearization [55] is presented. Rarefied gas flows are significantly important especially in vacuum technology since any small variation in pressure prediction of vacuum system may have a significant impact on the performance and accuracy of the system. Therefore, a correct and accurate prediction of pressure drop in rarefied gas flows is crucial and it makes the study of entrance effects crucial due to excess pressure drop occurs at entrance

region. For this purpose, the equations of motion are linearized using a linearization techniques proposed in the literature and the closed form velocity solution for the entrance region is obtained. In derivation of velocity solution, first order, second order and general slip models are implemented. Based on the obtained velocity solution, pressure drop and apparent friction factor which are the quantities of interest for engineering applications are derived and plotted along the channel.

The novelty of this thesis can be emphasized on two different parts. Reviewing the literature, a very limited number of studies can be found for numerical analyses of inertial microfluidics. Also, the lack of a general computational model for particle tracking in inertial microfluidics can be strongly understood. For this purpose, the present thesis present and develops s general computational model for prediction of particle tracking in inertial microfluidics. Furthermore, it exploits and implements the results from a very recent study for derivation of inertial lift in 3D Poiseuille flow. In this way, the present study fills a gap in the literature for the computational analyses in inertial microfluidicsapplications. The second part of the thesis is also very important in microfluidic applications. The effect of hydrodynamic entrance region is important due to the excess pressure drop occur in that region. There exist bunch of research studies in the literature which are devoted to the slip gas flows. However, these studies are mostly limited to the fully-developed region and neglect the effect of entrance region. In short micro-channels with low length over diameter ratio, the effect of entrance is significant and can not be neglected. Most of the studies in the literature for the hydrodynamic entrance region are limited to first order slip. In the present thesis, in addition to second order slip, general slip model proposed by Beskok is also implemented. Beskok model has shown excellent agreement for the velocity profile with DSMC results in the fully developed region. On the other hand, second order accuracy of Beskok model extends the applicability of Navier-Stokes equation for Kn up to 0.25.

1.5 Outline of the Thesis

The complete thesis includes the flowing main parts:

Chapter 1 presents a very brief introduction and background information about the modeling of fluid flow in micro-channels. Both the gas flow and liquid model flowing is discussed. More specifically, a background information about inertial microfluidics is also presented.

Chapter 2 presents a computational model for the simulation of particle motion for inertial microfluidic applications. LDP method is implemented, and the location of the particle focusing inside straight and spiral micro-channels are explored. The comparison of the different expressions for the induced forces on the particle is presented. The computational findings are also supported by the experimental results.

Chapter 3 presents an analytical model for gaseous flow at the hydrodynamic entrance region of 2D micro-channels. For this purpose, second-order slip models have been implemented for a gas flow at the entrance region of slit micro-channel, circular micro-channel and concentric annular micro-channels by exploitation of linearization proposed by Langhaar [55]. The complete mathematical model and formulations are given, and the results are discussed.

Chapter 4 summarizes and deduces remarkable conclusions observed in former chapters and also suggests different ideas for future research directions.

Chapter 2

Modeling of Inertial Particle Flow

Particle manipulation in microfluidic channels is an important problem since it is the basis of many microfluidic technologies for biomedical applications. Particle manipulation can be accomplished by means of many different techniques such as hydrodynamic, electrokinetic, magnetic and etc [1]. Hydrodynamic techniques are the most promising ones among them since it just uses the flow field which leads to a passive manipulation without any need for additional equipment. Particle separation based inertial microfluidics is a passive manipulation procedure which has many advantages such as high throughput, simple structure, label free and so forth. Furthermore, particle manipulation based inertial microfluidics is a harmless method which cause no damage to the cells and bio-particles which is important in biological applications. Particle manipulation can generally be accomplished through two different classes of active and passive techniques. This classification is based on the type of implemented forces that have been used for manipulating particles. Active methods usually exploit external forces such as dielectrophoresis [8, 56], acoustophoresis [57, 58], magnetophoresis [59], optical tweezers [60] and so forth which necessitate the utilization of additional equipments. However, passive techniques basically avail intrinsic hydrodynamic forces

and channel geometry to achieve particle manipulation. Three different and dominant passive techniques have been investigated in the literature as inertial microfluidics [26], pinched flow fractionation [61] and deterministic lateral displacement [62]. Among these techniques, inertial microfluidics has latterly received significant attention [27–41] due to its simplicity, low cost and high throughput.

Inertial microfluidics is typically assigned to the systems operating with intermediate Reynolds number between Stokes regime and Turbulent. Stokes flow regime is assigned to fluidic systems operating with very low Reynolds number. In such a case, the inertial effects become negligible and results in a linear equation of motion for the fluid element known as Stokes equation. Stokes equation can be readily derived from Navier-Stokes equation considering low Reynolds. For this purpose, axial equation of motion for a steady-state, incompressible and newtonian fluid in Cartesian coordinate can be written as:

$$\rho\left(u\frac{\partial u}{\partial x}+v\frac{\partial u}{\partial y}+w\frac{\partial u}{\partial z}\right)=-\frac{\partial p}{\partial x}+\mu\frac{\partial^2 u}{\partial x^2} \tag{2.1}$$

Following the dimensionless parameters below:

$$\lambda=\frac{u}{\bar{u}},\ \eta=\frac{v}{\bar{u}},\ \zeta=\frac{w}{\bar{u}},\ q=\frac{y}{D_h},\ \sigma=\frac{x}{D_h},\ h=\frac{z}{D_h},\ \tilde{p}=\frac{p}{p_0},\ p_0=\frac{\mu\bar{u}}{D_h}, \tag{2.2}$$

It should be pointed out that a different dimensionless parameter was chosen for the pressure based on viscosity. This selection is due to this fact that we want to investigate the role of inertia and Reynolds and therefore the dimensionless parameters should be independent of inertial parameters. By substituting dimensionless parameters 2.2 to Eq. (2.1) and defining the Reynolds number as $Re=\rho\bar{u}D_h/\mu$:

$$Re\left(\lambda\frac{\partial\lambda}{\partial\sigma}+\eta\frac{\partial\lambda}{\partial q}+\zeta\frac{\partial\lambda}{\partial h}\right)=-\frac{\partial\tilde{p}}{\partial\sigma}+\frac{\partial^2\lambda}{\partial\sigma^2} \tag{2.3}$$

Considering low Reynolds number (which is interpreted as the ratio of inertial forces over viscosity forces), the left hand side of the Eq. (2.3) which is the convective term vanishes and equation of Stokes is obtained. One may conclude the validity of Stokes equation for fully developed flow condition even at high Reynolds number which is correct. To clarify this, two different effects need to be explained. The effect of inertial term on the continuous phase flow at the absence of particle and the effect of inertial term in particle flow. For instance, in

straight channels with uniform cross sectional area, the Stokes equation is valid for the fully developed flow condition even at high Reynolds number. It should be taken into consideration that this equation describes the fluid elements behavior. By introducing the particle into the flow, the type of disturbances and vortices which the presence of particle creates in the flow is different in inertial and Stokes flow regime (due to different particle Reynolds number). This difference results in different type of forces acting on the particle. On the other hand, the effect of inertial term can be also understood on the fluid flow without the presence of particle. For example, by introducing a curvature for the channel path or changing the channel cross sectional area, different type of flow motion pattern (such as secondary flow) can be observed which is due to the inertial term. Altogether, it can be deduced that Stokes equation can also satisfy the fluid element behavior in some specific cases at high Reynolds number, however, the presence and motion of particle is significantly different in those cases due to effect of inertial term.

Due to finite Re in inertial microfluidics, inertial effects are sufficiently significant not to be neglected which consequently results in a non-linear equation of motion. In such a case, different physical phenomenon occur which are the basis of inertial microfluidics. One of the phenomenon that has been observed is the inertial migration of particles. Inertial migration is the motion of particles in lateral direction of channel due to the existence of inertial lift force. Lateral migration of particles consequently causes particles to fill some certain positions downstream in the channel which is called as equilibrium positions. Particle equilibrium was first reported by Segre and Silberberg [63, 64] in 1961 and 1962. They observed that randomly dispersed rigid spherical particles at inlet of a macro-tube migrate to a distance of 0.6 times radius of tube from center after a certain distance downstream. Later on, in order to investigate the mechanism of particle focusing, many experiment were performed using different geometry such as square channel [65, 66]. Inertial lift force which appears in inertial microfluidics due to the effect of inertia term in momentum equation, depends on many parameters such as channel Re, channel geometry, particle size and geometry and so forth. Therefore, finding a general solution for description of inertial lift force is most often cumbersome and even impossible. Different components of inertial lift force

has been categorized in the literature and a net inertial lift force is defined which is the sum of all these components. The components can be categorized as:

(1) Rotation induced lift force: The rotation induced lift force, which is also known as Magnus force, is the result of interaction of a rotational cylinder or sphere with a uniform upstream velocity profile. Considering no-slip velocity condition on the surface of cylinder or sphere, a pressure difference is generated due to the fluid velocity difference in lower and upper part of the sphere which leads to the Magnus force. Some mathematical expression has been also derived and proposed in the literature for description of Magnus force [67].

(2) Slip-shear induced lift force: The slip-shear induced lift force, which is called as Saffman force, is the resultant force due to interaction of a cylinder or sphere with unbounded simple shear flow [68]. In this case the shear gradient of flow is considered as zero.

(3) Shear gradient lift force: The shear gradient lift force is considered for the particle-flow interaction with non-zero shear gradient flows due to the flow velocity curvature

(4) Wall induced lift force: The wall induced lift force is the effect due to the presence of channel walls. Shear gradient lift force pushes the particle away from the center of channel due to the flow distribution curvature, however, wall induced lift force repels the particles away from the walls. Finally, for a viscous Poiseuille flow net inertial lift force is considered as the sum of these four inertial forces. However, the effect of first two components is negligible and the net inertial lift force can be considered as the effect of shear gradient lift together with wall induced lift force.

Some studies have been carried out to attempt to find a mathematical description for the net inertial lift force. Using matched asymptotic expansion method, Asmolov [44] could find an analytical solution for the net inertial lift force acting on a small rigid spherical particle flowing in a plane Poiseuille flow. The inertial

lift force coefficient was derived as:

$$f_L = \frac{F_L D_h^2}{\rho U^2 a^4} \tag{2.4}$$

where F_L is the net inertial lift force, D_h is the hydraulic diameter of channel, ρ is the fluid density, U is the maximum velocity of undisturbed velocity profile and a is the particle radius. Inertial lift force coefficient is a function of channel Reynolds number and transverse position of particle in the channel cross section. Equilibrium position of particles at the absence of secondary flow can be considered where the inertial lift coefficient is zero. Two different classes of equilibrium positions can be considered as stable and unstable equilibrium position where inertial lift force coefficient is zero. Any small deviation from unstable equilibrium positions causes particles never return to the initial position. In the other words, deflection of particles from unstable position causes particles migrate to stable positions. Based on this discussion, channel centerline in plane Poiseuille flow is a unstable equilibrium point, however, inertial lift coefficient is zero. Recently, an asymptotic model has been derived for the inertial lift force acting on rigid spherical particles flowing in a 3D Poiseuille flow in a square and rectangular (with aspect ratio of 2) cross-section micro-channels [42, 43]. Using immersed boundary integral method, the motion of a spherical rigid particle in a straight square channel was studied [69]. In this study, 8 equilibrium positions were reported for the spherical particle on the centers of the channel faces and near the corners of the channel cross section. It was also reported that the equilibrium positions on the centers of the channel faces are always stable, however, the ones near the corner of channel cross section are unstable for Reynolds numbers lower than a critical value. The effect of high Reynolds number was also studied (Reynolds up to 1000), which was not investigated in Hood study. More recently, a generalized formula was proposed for the inertial lift force on a spherical rigid particle in a straight rectangular channel with different aspect rations [70]. Direct numerical simulation was implemented and a fitting-analyses was performed to generalize the formula. Furthermore, using the simulation results, they have reported a good agreement of the particle focusing pattern in spiral and serpentine channels with the experimental results utilizing Lagrangian particle tracking method.

Utilizing these stable equilibrium positions, inertial microfluidics can be implemented for particle focusing and separation. To investigate the particle focusing and separation, different channel design with different geometries have been exploited experimentally. The most common and important channel designs in the literature can be classified as straight channel with uniform cross sectional area, straight channel with expansion-contraction or pillar arrays, spiral channel and serpentine channels. Straight channel is one of the simplest channel structures which have been abundantly utilized in the literature. Due to simplicity of micro-fabrication process, straight channels with square or rectangular cross section have been mostly investigated. In square straight channels, particles fill four focusing positions at symmetrical axes of the channel [71]. One the contrary, for rectangular straight channels, particles fill only two equilibrium positions placed on the short axis of the channel and away from the channel wall [72–74]. Particle focusing mechanism in three dimensional Poiseuille flow such as square and rectangular channel is basically different than two dimensional Poiseuille flow between parallel plates. A complete explanation describing the focusing mechanism in three dimensional Poiseuille flow can be found elsewhere [72]. Apart from exploitation of straight channels for investigation of fundamental inertial concepts and understanding [27–29, 33, 39], it has been also implemented for different microfluidic applications. Passive separation of pathogenic bacteria from diluted blood [31], purification of adrenal cortical progenitor from digestions of murine adrenal glands [34], particle ordering for cytometer systems [32] are a few number of straight channel applications in microfluidics.

In spite of simple and clear focusing mechanism in straight channels, it is unable to yield a fast particle separation and focusing process. As aforementioned, inertial lift force has an inverse proportion with the particle size. Consequently, inertial lift force drops drastically for small particles. Substantial reduction in inertial lift force also causes a significant drop in the magnitude of particle migration velocity in the lateral direction. Thus, high length of straight channel is required to achieve particle focusing which results in high footprint of the microchip. On the other hand, straight channel can not be considered as a size-based

particle separator. All aforementioned defects make straight channel not an efficient design for particle separation and focusing applications.

In order to improve the defects observed in straight channel for particle focusing and separation, curved micro-channels have been introduced and exploited. Among curved micro-channels, spiral channels have attracted great attentions of researcher due to their promising capabilities in size-based particle separation and compact architecture. Flow field pattern induced in spiral channels due to the existence of channel curvature can be considered as one of the basis in inertial microfluidics. The curvature introduced along the channel creates centrifugal pressure difference in the radial direction of the channel due to the velocity mismatch at the center of the channel and vicinity of the channel wall. This pressure difference induces two symmetric counter rotating vortices known as secondary or Dean flow in the channel cross section. Dean flow assists the particles to migrate faster in the lateral direction by exerting a drag force known as Dean drag on the particles in the cross section of channel. Dean drag plays an important substantial role in particle focusing and separation. An expression has been proposed in the literature for approximating the magnitude of Dean flow velocity such as [30]:

$$V_D = 1.8 \times 10^{-4} \times K^{1.63} \tag{2.5}$$

where

$$K = \sqrt{\frac{D_h}{2R_c}} Re \tag{2.6}$$

where D_h is the hydraulic diameter of channel, R_c is the radius of curvature of channel and Re is the channel Reynolds number. The equations above show the inverse relationship between Dean flow velocity and radius of curvature of channel. The greater radius of curvature, the weaker Dean vortices velocity.

Spiral micro-channels have been extensively exploited for particle separation and filtration. Spiral micro-channel with rectangular cross-section (with an aspect ratio 2) was exploited for particle separation [75]. In this study, a complete separation of two different particle of sizes 1.9 μm and 7.2 μm was reported and investigated for different channel Re. It was observed that larger particles migrate toward the inner wall while smaller particles move toward the outer wall. Furthermore, larger particles showed a narrower focusing line in comparison with

the smaller particles. An extension study [76] was also carried out to improve the capability of the former chip in particle separation. Moreover, for separation and enrichment of tumour cell from diluted peripheral whole blood, a passive double spiral micro-channel were utilized [35, 77]. In this design, spiral channels with width of 300 μm and height of 50 μm and the other one with height of 80 μm were considered for the particle separation. A numerical investigation was also performed using commercial software FLUENT by using Asmolov [44] inertial lift force. They reported that a double spiral channel has a better efficiency in particle separation than a single spiral.

Spiral micro-channels most often are designed with rectangular cross-section due to straightforward micro-fabrication process. However, spiral with different cross-section may exhibit better performance in comparison with rectangular cross-section. For this purpose, a novel spiral micro-channel with trapezoidal cross section was designed and experimentally investigated [78]. The chip was used to separate and recover polymorphonuclear leukocytes and mononuclear leukocytes from diluted human blood. This novel spiral design exhibited a higher resolution separation and efficiency in comparison with the rectangular design with the same dimensions. Later on, the same channel structure was implemented [79] and a sharp transition of equilibrium positions from inner half channel to outer half channel with a size-based critical flow rate was observed. Furthermore, slanted spiral channel with trapezoidal cross section [37] was successfully exploited for the enrichment of CTCs from blood samples. it was observed that the smaller hematologic components equilibrated near the outer wall while the larger CTCs were pushed toward the inner wall of the channel. One of key factor in an efficient inertial particle separation is the particle size. Ratio of particle size over hydraulic diameter of channel is a characteristic value which can determine the possibility of focusing of a specific particle size in an specific channel geometry. Different criteria have been proposed for practical design to evaluate the focusing possibility. These criteria relating the particle size to channel geometry and also the required flow rate can be found elsewhere [26]. These relations were derived for rectangular straight channel and have not been rigourously verified. Inertial separation of particles with high size variation has been carried out abundantly

in the literature [35, 77, 80]. The critical and challenging inertial separation is for the particle or bio-particles with low size variation. In such a case, particles typically equilibrate in locations close to each other which makes the separation hard and decreases the efficiency. For this purpose, different type of channel geometry need to be exploited to increase the efficiency. Recently, a multiplexing slanted spiral micro-channel chip with trapezoidal cross-section (which had shown a sharp size-based transition from inner to outer half channel [79]) was utilized for separation of red blood cell from blood plasma. This channel design yielded a high throughput with a high efficiency of red blood cell separation.

Many of the studies in the literature are experimental and the design of the micro-channel has been performed based on some order-of-magnitude estimates. One better way is to perform simulation and predict the equilibrium positions in the micro-channel for an optimized design. Numerical and mathematical study of single spherical rigid particle has been carried out in the literature using finite-size particle [39, 42–44, 69]. However, simulation of many particle motion is limited in the literature. For many particle inertial microfluidics simulation, finite-sized particle approach is not possible with today's computers, since the typical length over diameter of the micro-channel is very long and the particle travels couple hundred diameter in around one second. Moreover, to re-solve the interaction of the particle with the wall, the meshing of the problem is very critical. On the other hand, in finite-size approach, particle-particle interaction also needs to be taken into consideration which makes the problem even impossible. A few studies have been carried out in the literature which have claimed acceptable simulation results for many particle inertial simulation in line with experimental observations. Sun and etal [35, 77] have reported a numerical model based on force balance integration known as Lagrangian particle tracking method. In these studies, results of inertial lift derived by Asmolov [44] were utilized and good agreement with experiment results was reported. Inertial lift derived by Asmolov is valid for a rigid spherical particle in a 2D poiseuille flow. In this results, shear gradient and wall induced lift forces have been taken into consideration. On the other hand, in a 3D poiseuille flow, the focusing mechanism is significantly different than 2D Poiseuille flow since Safmann force comes into picture and plays

a substantial role in focusing mechanism. Ergo, the agreement of sun and etal numerical results for a 3D spiral channel with experimental observations is quit questionable. Recently, the same group [70] have proposed a generalized formula for the inertial lift acting on a rigid spherical particle in 3D poiseuille flow using direct numerical simulation and data fitting analyses. Finally, they have exploited the obtained inertial lift to track the particle using Lagrangian tracking method. An excellent agreement was obtained with the simulation and numerical results.

In this chapter, a computational model is developed for particle tracking in inertial microfluidics. This model is based on the Lagrangian Discrete Phase model (LDPM). In this method, point size particle approach is implemented. However, the forces acting on the particle needs to be quantified as a function of Re and the location of the particle within the micro-channel. The continuum phase characteristics which is the fluid flow in our simulation needs to be obtained without the presence of discrete phase (particle). Once the flow field is obtained in the micro-channel, the trajectory of the particle can be obtained in the post-processing step. In the post-processing step, LDP method which utilizes the Newton's second law and force balance integration for the discrete phase is implemented to model the particle motion in a straight and spiral micro-channel with different aspect ratios. The continuous phase (flow field) is solved without the presence of the particle using COMSOL Multi-physics commercial software. The trajectory of the particles are obtained using LDPM via COMSOL-MATLAB interface. To resemble the random inlet position of the particles, many particles are simulated with random initial locations from the inlet of the micro-channel. The authenticity of the computational model is verified with experimental results from literature [75]. After verification, the computational model was utilized for particle motion in a high aspect ratio spiral channel with different flow rates. Finally, experimental investigations were also carried out for the high aspect ratio spiral channel and the results are compared with the simulation predictions.

2.1 Computational Model

In this section, a computational model for predicting particle trajectories in inertial microfluidics is developed. This model is based on Lagrangian discrete phase model which exploits force balance integration for particle tracking. In this model, the continuous phase which is fluid flow field is solved without presence of discrete phase which is the particle flow. Finally, the particle tracking is performed by temporal integration of force balance relations for the discrete phase.

2.1.1 Generalized Model for Particle Tracking

To track the particle, discrete phase method which is based on force balance integration is implemented. For this purpose, force balance relations for the discrete phase need to be obtained. According to the Newton's second law, the force balance can be written as:

$$\sum \mathbf{F} = M_p \mathbf{a_p} \tag{2.7}$$

where M_p is the mass of particle, $\mathbf{F}$ is the equivalent force acting on the particle and $\mathbf{a_p}$ is the particle acceleration. The forces acting on the particle for an inertial microfluidics application can be written as follows:

$$\mathbf{a_p} = \frac{1}{M_p}\mathbf{F_D} + \frac{1}{M_p}\mathbf{F_L} + \frac{1}{M_p}\mathbf{F_B} + \frac{1}{2}\frac{\rho_f}{\rho_p}(\mathbf{a_f} - \mathbf{a_p}) \tag{2.8}$$

The first, second, third and last terms are acceleration due to the drag force, inertial lift force, body force and virtual mass force, respectively. The formulation above can be rearranged as:

$$\mathbf{a_p} = \frac{1}{1 + \frac{1}{2}\frac{\rho_f}{\rho_p}} \left[\frac{1}{M_p}\mathbf{F_D} + \frac{1}{M_p}\mathbf{F_L} + \frac{1}{M_p}\mathbf{F_B} + \frac{1}{2}\frac{\rho_f}{\rho_p}\mathbf{a_f} \right] \tag{2.9}$$

The equation above is an initial value problem that can be solved using temporal integration methods. For this purpose, the next part is devoted to briefly review the temporal integration methods.

2.1.1.1 Temporal Integration Methods

A simple initial value problem can be stated as:

$$\frac{dx}{dt} = f(x,t) \tag{2.10}$$

where f is a function of unknown dependent variable x and independent variable t. To solve the Eq. (2.10), a temporal discretization can be made as $t_0, t_0 + \Delta t, t_0 + 2\Delta t, ...$ where t_0 is the initial time where the value of x is known. Now, the temporal derivative in Eq. (2.10) can be discretized. Based on this discretization, different integration methods can be established.

(i) Explicit Euler's Method: In this method, the temporal derivative in Eq. (2.10) is discretized as:

$$\left(\frac{dx}{dt}\right)^k = \frac{x^{k+1} - x^k}{\Delta t} \tag{2.11}$$

The equation above can be arranged to be written as:

$$x^{k+1} = x^k + \left(\frac{dx}{dt}\right)^k \Delta t \tag{2.12}$$

Using Eq. (2.10), the temporal derivative at step k can be replaced by $f(x^k, t^k)$ and the final version of the equation can be written as:

$$x^{k+1} = x^k + \Delta t \; f(x^k, t^k) \tag{2.13}$$

One of the advantages of explicit methods is the simple structure. However, the stability of explicit methods are very critical. Explicit methods are conditionally stable. This means that the time step needs to be chosen sufficiently small to ensure the stability. The criterion most often increases the number of time steps which consequently results in higher computational time.

(ii) Implicit Euler's Method: In this method, the temporal derivative in Eq. (2.10) is approximated as:

$$\left(\frac{dx}{dt}\right)^k = \frac{x^k - x^{k-1}}{\Delta t} \tag{2.14}$$

and the final version can be stated as:

$$x^k = x^{k-1} + \Delta t \; f(x^k, t^k) \tag{2.15}$$

where the term x^k which is unknown appears in both side of the equation. One of the advantages of implicit Euler's method is its unconditionally stability which allows us to choose larger time steps without any convergence problems. This issue helps us to reduce the number of time steps and consequently the computational time. However, due to the appearance of unknown values in both side of the integration equation, sometimes solution of a system of equations is required which may be problematic and time-consuming.

(iii) Crank-Nicolson Method: This method can be considered as a combination of explicit and implicit Euler's method. This method for the evaluation of step $k+1$ can be written as:

$$x^{k+1} = x^k + \frac{1}{2}\Delta t \; \left[f(x^k, t^k) + f(x^{k+1}, t^{k+1})\right] \tag{2.16}$$

Likewise implicit methods, it is unconditionally stable and has a higher accuracy in comparison with implicit Euler's method. In this method, most often a system of equations need to be solved. In more complicated cases, an initial predictor such as explicit Euler is used to predict the value of unknown x at step $k+1$. Then, by using Crank-Nicolson, the value of x at step $k+1$ is updated and finally in a trial and error procedure, the final value of x at step $k+1$ is obtained as the converged value.

2.1.2 Generalized Model in Cartesian Coordinates

The selection of coordinate system is dependent on problem geometry. Cartesian coordinates system is appropriate for particle tracking in straight channel. For this purpose, a function $\mathbf{G}$ can be defined as:

$$\mathbf{G} = \frac{1}{1 + \frac{1}{2}\frac{\rho_f}{\rho_p}} \left[\frac{1}{M_p}\mathbf{F_D} + \frac{1}{M_p}\mathbf{F_L} + \frac{1}{M_p}\mathbf{F_B} + \frac{1}{2}\frac{\rho_f}{\rho_p}\frac{d\mathbf{u_f}}{dt}\right] \tag{2.17}$$

and consequently, the Eq. (2.9) can be re-written as:

$$\frac{d\mathbf{u_p}}{dt} = \mathbf{G} \tag{2.18}$$

The Eq. (2.18) is an initial value problem which a temporal integration technique needs to be implemented to solve the equation. Due to superiority of Crank-Nicolson temporal integrator over explicit and implicit Euler's method, this technique is utilized in the present study. For this purpose, the temporal integrator formula can be written as:

$$\mathbf{u_p}^{k+1} = \mathbf{u_p}^{k} + \frac{1}{2}(\mathbf{G}^k + \mathbf{G}^{k+1})\Delta t \tag{2.19}$$

where the superscript $(k+1)$ shows the values at time $t + \Delta t$ and superscript k shows the values at time t. Using Eq. (2.19), once the velocity of the particle is known, the new position of particle can be found as:

$$\mathbf{x}_p^{k+1} = \mathbf{x}_p^k + \frac{1}{2}(\mathbf{u}^k + \mathbf{u}^{k+1})\ \Delta t \tag{2.20}$$

Now, the values of $\mathbf{G}^k$ and $\mathbf{G}^{k+1}$ need to be evaluated for the Crank-Nicolson method. The first term in the function $\mathbf{G}$ that needs to be evaluated is the drag force. Drag force is a function of both particle velocity and location. So, it can be written as:

$$\mathbf{F_D^k} = \mathbf{F_D}(\mathbf{x^k}, \mathbf{u_p^k}) \tag{2.21}$$

and for the step $k+1$:

$$\mathbf{F_D^{k+1}} = \mathbf{F_D}(\mathbf{x^{k+1}}, \mathbf{u_p^{k+1}}) \tag{2.22}$$

The second term is the inertial lift force. Inertial lift is a function of particle location only and can be written as:

$$\begin{aligned} \mathbf{F_L^k} &= \mathbf{F_L}(\mathbf{x^k}) \\ \mathbf{F_L^{k+1}} &= \mathbf{F_L}(\mathbf{x^{k+1}}) \end{aligned} \tag{2.23}$$

The body force $\mathbf{F_B}$ is solely dependent on particle properties and is independent of particle velocity and location. For this purpose, the term $\frac{1}{M_p}\mathbf{F_B}^k$ is considered constant and named as $\mathbf{f}$. The last term which needs to be considered is virtual mass force. This force is due to the difference in the acceleration of particle and fluid elements surrounding the particle. Since in the Eq. (2.9), the particle

acceleration was separated from this force, the last term is only a function of particle location. For convenience, the term $\frac{1}{2}\frac{\rho_f}{\rho_p}\frac{d\mathbf{u_f}}{dt}$ is called as $\mathbf{f_v}$ and the discretized form can be written as:

$$\begin{aligned}(\frac{1}{2}\frac{\rho_f}{\rho_p}\frac{d\mathbf{u_f}}{dt})^k &= \mathbf{f_v}(\mathbf{x^k}) \\ (\frac{1}{2}\frac{\rho_f}{\rho_p}\frac{d\mathbf{u_f}}{dt})^{k+1} &= \mathbf{f_v}(\mathbf{x^{k+1}})\end{aligned} \tag{2.24}$$

Now, the temporal integration using Crank-Nicolson method for the particle velocity can be written as:

$$\begin{aligned}\mathbf{u_p}^{k+1} = \mathbf{u_p}^k + \frac{1}{2}\big[&\mathbf{F_D}(\mathbf{x^k}, \mathbf{u_p^k}) + \mathbf{F_D}(\mathbf{x^{k+1}}, \mathbf{u_p^{k+1}}) + \mathbf{F_L}(\mathbf{x^k}) + \mathbf{F_L}(\mathbf{x^{k+1}}) + 2\mathbf{f} \\ &+ \mathbf{f_v}(\mathbf{x^k}) + \mathbf{f_v}(\mathbf{x^{k+1}})\big]\Delta t\end{aligned} \tag{2.25}$$

As it can be seen in the Eq. (2.25), particle velocity at the step $k+1$ appears in both side of the equation and therefore a solution of system of equations is required. On the other hand, the location of particle at step $k+1$ also appears in the right hand side of the Eq. (2.25). In this case, an initial predictor using explicit Euler's method is utilized to predict the particle location at step $k+1$ such as:

$$\mathbf{x^{k+1}} = \mathbf{x^k} + \Delta t \mathbf{u_p^k} \tag{2.26}$$

Using the obtained particle location from initial predictor, the velocity of particle at step $k+1$ is found using Eq. (2.25) and then the particle location at step $k+1$ is corrected by Eq. (2.20). A chart for the illustration of methodology is depicted in Figure 2.1.

2.1.3 Generalized Model in Cylindrical Coordinates

Cylindrical coordinates system is appropriate for curvilinear channels such as spiral channel. In this section, the force-acceleration relations are stated in cylindrical coordinates considering the centrifugal effects. For this purpose, particle

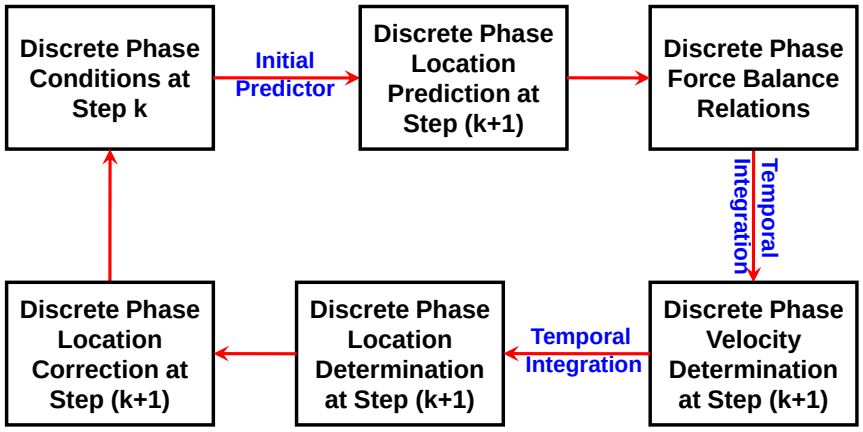

Figure 2.1: Methodology chart for the present computational model

velocities in radial, tangential and z direction are defined as:

$$\begin{aligned} u_{pr} &= \dot{r} \\ u_{p\theta} &= r\dot{\theta} \\ u_{pz} &= \dot{z} \end{aligned} \tag{2.27}$$

Where u_{pr}, $u_{p\theta}$ and u_{pz} are the particle velocity in radial, tangential and z direction respectively. Vector r is defined as the distance between particle and origin and θ as the angle between vector r and the x-axis. The acceleration in cylindrical coordinate can be expressed as:

$$\begin{aligned} a_{pr} &= \ddot{r} - r\dot{\theta}^2 \\ a_{p\theta} &= r\ddot{\theta} + 2\dot{r}\dot{\theta} \\ a_{pz} &= \ddot{z} \end{aligned} \tag{2.28}$$

The acceleration can be expressed in terms of particle velocity. For this purpose, the formulations below can be used :

$$\begin{aligned} \ddot{r} &= \dot{u}_{pr} \\ r\dot{\theta}^2 &= \frac{u_{p\theta}^2}{r} \\ r\ddot{\theta} &= \dot{u}_{p\theta} - \frac{u_{pr}u_{p\theta}}{r} \\ \dot{r}\dot{\theta} &= \frac{u_{pr}u_{p\theta}}{r} \end{aligned} \tag{2.29}$$

and the final version for acceleration formulations can be re-written as follows:

$$\begin{aligned} a_{pr} &= \dot{u}_{pr} - \frac{u_{p\theta}^2}{r} \\ a_{p\theta} &= \dot{u}_{p\theta} + \frac{u_{pr}u_{p\theta}}{r} \\ a_{pz} &= \dot{u}_{pz} \end{aligned} \tag{2.30}$$

The Eq. (2.9) can be re-written based on the definitions presented for Cartesian coordinates as:

$$\mathbf{a_p} = \frac{1}{1+\frac{1}{2}\frac{\rho_f}{\rho_p}}\left[\frac{1}{M_p}\mathbf{F_D} + \frac{1}{M_p}\mathbf{F_L} + \mathbf{f} + \mathbf{f_v}\right] \tag{2.31}$$

Using Eq. (2.30), Eq. (2.31) can be re-written as:

$$\begin{aligned} \dot{u}_{pr} - \frac{u_{p\theta}^2}{r} &= \frac{1}{1+\frac{1}{2}\frac{\rho_f}{\rho_p}}\left[\frac{1}{M_p}\mathbf{F_D}_r + \frac{1}{M_p}\mathbf{F_L}_r + \mathbf{f}_r + \mathbf{f_v}_r\right] \\ \dot{u}_{p\theta} + \frac{u_{pr}u_{p\theta}}{r} &= \frac{1}{1+\frac{1}{2}\frac{\rho_f}{\rho_p}}\left[\frac{1}{M_p}\mathbf{F_D}_\theta + \frac{1}{M_p}\mathbf{F_L}_\theta + \mathbf{f}_\theta + \mathbf{f_v}_\theta\right] \\ \dot{u}_{pz} &= \frac{1}{1+\frac{1}{2}\frac{\rho_f}{\rho_p}}\left[\frac{1}{M_p}\mathbf{F_D}_z + \frac{1}{M_p}\mathbf{F_L}_z + \mathbf{f}_z + \mathbf{f_v}_z\right] \end{aligned} \tag{2.32}$$

Writing Eq. (2.32) with respect to particle velocity temporal derivative yields:

$$\begin{aligned} \dot{u}_{pr} &= \frac{1}{1+\frac{1}{2}\frac{\rho_f}{\rho_p}}\left[\frac{1}{M_p}\mathbf{F_D}_r + \frac{1}{M_p}\mathbf{F_L}_r + \mathbf{f}_r + \mathbf{f_v}_r\right] + \frac{u_{p\theta}^2}{r} = G_r \\ \dot{u}_{p\theta} &= \frac{1}{1+\frac{1}{2}\frac{\rho_f}{\rho_p}}\left[\frac{1}{M_p}\mathbf{F_D}_\theta + \frac{1}{M_p}\mathbf{F_L}_\theta + \mathbf{f}_\theta + \mathbf{f_v}_\theta\right] - \frac{u_{pr}u_{p\theta}}{r} = G_\theta \\ \dot{u}_{pz} &= \frac{1}{1+\frac{1}{2}\frac{\rho_f}{\rho_p}}\left[\frac{1}{M_p}\mathbf{F_D}_z + \frac{1}{M_p}\mathbf{F_L}_z + \mathbf{f}_z + \mathbf{f_v}_z\right] = G_z \end{aligned} \tag{2.33}$$

The Eq. (2.33) is in the from of an initial value problem which needs to be integrated over time. For this purpose, functions G_r, G_θ and G_z should be evaluated at steps k and $k+1$. For this purpose, they can be written as:

$$\begin{aligned} G_r^k &= \frac{1}{1+\frac{1}{2}\frac{\rho_f}{\rho_p}}\left[\frac{1}{M_p}\mathbf{F_D}(\mathbf{r^k}, \mathbf{u_p^k})_r + \frac{1}{M_p}\mathbf{F_L}(\mathbf{r^k})_r + \mathbf{f}_r + \mathbf{f_v^k}_r\right] + \frac{(u_{p\theta}^2)^k}{r^k} \\ G_\theta^k &= \frac{1}{1+\frac{1}{2}\frac{\rho_f}{\rho_p}}\left[\frac{1}{M_p}\mathbf{F_D}(\mathbf{r^k}, \mathbf{u_p^k})_\theta + \frac{1}{M_p}\mathbf{F_L}(\mathbf{r^k})_\theta + \mathbf{f}_\theta + \mathbf{f_v^k}_\theta\right] - \frac{u_{pr}^k u_{p\theta}^k}{r^k} \\ G_z^k &= \frac{1}{1+\frac{1}{2}\frac{\rho_f}{\rho_p}}\left[\frac{1}{M_p}\mathbf{F_D}(\mathbf{r^k}, \mathbf{u_p^k})_z + \frac{1}{M_p}\mathbf{F_L}(\mathbf{r^k})_z + \mathbf{f}_z + \mathbf{f_v^k}_z\right] \end{aligned} \tag{2.34}$$

where $\mathbf{r}$ is the position vector of particle location in the form of (r, θ, z). The mentioned functions at step $k+1$ can be written similarly:

$$
\begin{aligned}
G_r^{k+1} &= \frac{1}{1+\frac{1}{2}\frac{\rho_f}{\rho_p}} \left[\frac{1}{M_p} \mathbf{F_D}(\mathbf{r^{k+1}}, \mathbf{u_p^{k+1}})_r + \frac{1}{M_p} \mathbf{F_L}(\mathbf{r^{k+1}})_r + \mathbf{f}_r + \mathbf{f_v^{k+1}}_r \right] + \frac{(u_{p\theta}^2)^{k+1}}{r^{k+1}} \\
G_\theta^{k+1} &= \frac{1}{1+\frac{1}{2}\frac{\rho_f}{\rho_p}} \left[\frac{1}{M_p} \mathbf{F_D}(\mathbf{r^{k+1}}, \mathbf{u_p^{k+1}})_\theta + \frac{1}{M_p} \mathbf{F_L}(\mathbf{r^{k+1}})_\theta + \mathbf{f}_\theta + \mathbf{f_v^{k+1}}_\theta \right] - \frac{u_{pr}^{k+1} u_{p\theta}^{k+1}}{r^{k+1}} \\
G_z^k &= \frac{1}{1+\frac{1}{2}\frac{\rho_f}{\rho_p}} \left[\frac{1}{M_p} \mathbf{F_D}(\mathbf{r^{k+1}}, \mathbf{u_p^{k+1}})_z + \frac{1}{M_p} \mathbf{F_L}(\mathbf{r^{k+1}})_z + \mathbf{f}_z + \mathbf{f_v^{k+1}}_z \right]
\end{aligned}
\tag{2.35}
$$

Using Eq. (2.19), the velocity can be updated based on definition of functions G presented in Eq. (2.34) and (2.35). Finally, the particle location is updated using equations below:

$$
\begin{aligned}
r^{k+1} &= r^k + \frac{1}{2}(u_{pr}^{k+1} + u_{pr}^k)\Delta t \\
\theta^{k+1} &= \theta^k + \frac{1}{2}(\frac{u_{p\theta}^{k+1}}{r^{k+1}} + \frac{u_{p\theta}^k}{r^k})\Delta t \\
z^{k+1} &= z^k + \frac{1}{2}(u_{pz}^{k+1} + u_{pz}^k)\Delta t
\end{aligned}
\tag{2.36}
$$

2.1.4 Drag Force Model

Due to the relative motion of an object in a fluid medium, a resistive force acts on the object in opposite direction of the motion known as drag force. Due to strong dependency of drag force on object properties, it is somehow impossible to propose a general model for drag force. For some specific geometries, some relations have been proposed in the literature to estimate the drag force. For a rigid spherical particle flowing in a fluid medium, the drag force was proposed as [81]:

$$
\mathbf{F_D} = \frac{1}{2}\, \rho\, (\mathbf{u_f} - \mathbf{u_p})^2\, A\, C_D\, sign(\mathbf{u_f} - \mathbf{u_p}) \tag{2.37}
$$

where ρ is the fluid density, $\mathbf{u_f}$ is the undisturbed flow stream velocity, $\mathbf{u_p}$ is the particle velocity, A is the particle cross sectional area and C_D is the drag coefficient. Following the mentioned paper [81], drag coefficient is proposed as:

$$
C_D = \frac{a_1}{Re_s} + \frac{a_2}{Re_s^2} + a_3 \tag{2.38}
$$

Table 2.1: Coefficients for the drag force expression

a_1	a_2	a_3	Re_s
24.0	0	0	< 0.1
22.73	0.0903	3.69	$0.1 - 1$
29.1667	-3.8889	1.222	$1 - 10$
46.5	-116.67	0.6167	$10 - 100$
98.33	-2778	0.3644	$100 - 1000$

where a_1, a_2 and a_3 are coefficients which depends on relative Reynolds number of particle and fluid element. Values of these coefficients based on relative Reynolds number are tabulated in Table 2.1. Alternatively, for low relative Reynolds number, the equation of Stokes drag for a spherical particle can be exploited:

$$\mathbf{F_D} = 6\pi\mu R_p(\mathbf{u_f} - \mathbf{u_p}) \tag{2.39}$$

where μ is the dynamic viscosity of fluid medium and R_p is the particle radius. Stokes drag expression is accurate enough for small relative Reynolds numbers ($\lesssim 1$) for the particle.

2.1.5 Inertial Lift Model

Inertial lift force field is an phenomena which can be observed in finite Reynolds fluidic systems. Obtaining a solution for the inertial lift force in a desired channel is a cumbersome issue due to the dependency of inertial lift force to many parameters such as channel geometry, channel reynolds number, particle size and properties. Some studies have been carried out to obtain a solution for inertial lift force in simple and basic channel geometries. Unlike drag force, inertial lift force is strongly dependent on velocity profile and channel geometry. As it was discussed in the introduction section, for a rigid spherical particle flowing in a plane Poiseuille flow, Asmolov [44] derived an analytical solution for the inertial lift force based on matched asymptotic expansion. In this study, inertial lift force is expressed in the form of:

$$f_L = \frac{F_L D_h^2}{\rho U^2 a^4} \tag{2.40}$$

where f_l is the lift force coefficient, F_L is the lift force acting on the particle, D_h is the hydraulic diameter of the channel, ρ is the density of fluid, U is the maximum velocity in undisturbed velocity profile and a is the radius of particle. Inertial lift coefficient is a function of channel Reynolds number and the lateral position of particle. In this case, inertial lift force is normal to the walls. According to the discussion in introduction, Shear gradient induced and wall induced lift force are two dominant inertial forces acting on a particle in a plane Poiseuille flow. Shear gradient induced lift force pushes the particles away from the centerline of channel due to the curvature of velocity profile. On the other hand, wall induced lift force repels the particles away from the channel walls. In a plane Poiseuille flow, the balance of two aforementioned forces determines the focusing or equilibrium positions of particles in a parallel plates channel. f_L indicates the net inertial lift coefficient which is equal to zero in equilibrium positions. According to this formulation, inertial lift force is higher for larger particles which results in a faster focusing process. On the contrary, inertial lift force drastically reduces for small particles and causes particles reach to their equilibrium positions much slowly. Reynolds number is also a key factor in determination of equilibrium positions. It was observed that for high Reynolds numbers, equilibrium positions shift toward the channel walls. The solution derived by Asmolov for the inertial lift in plane Poiseuille flow shows a size independent equilibrium position. In the other words, this solution predicts same focusing positions for different size particles. In the case of square channel, Asmolov solution can be implemented for inertial lift force. For this purpose, two different inertial lift components need to be defined. Horizontal and vertical walls make two inertial lift forces. Resultant inertial lift force field using Asmolov solution is depicted in Figure 2.2-(a). Blue arrays show the direction and also magnitude of inertial lift force on each point. All the circles included in the figure show the positions where the inertial lift force is zero. As it can be observed from the figure, red and black circles indicate stable and unstable equilibrium positions in the channel respectively. Stability of equilibrium positions can be readily understood from the inertial lift force arrays in the vicinity of the points. For the red circles which indicate stable equilibrium points, inertial lift force arrays are inward to the points and consequently it causes the particles return to the initial point with any deflection. Similarly,

any deviation of particles from the black points causes particles never return to the unstable points. According to this discussion, four equilibrium points placed on the channel cross-section corners are determined for a square channel using Asmolov inertial lift force. However, experiments conducted in the literature show different focusing positions for particles in square and rectangular channels. For a rectangular channel with aspect ratio of 2, particles focus on the short axis at a distance of 0.2 times height from the wall. This issue shows that Asmolov solution is unable to predict the correct equilibrium positions in square and rectangular channels. In a plane Poiseuille flow, velocity and shear gradient is non-zero only in the lateral direction, however, in square and rectangular channel it is only zero in the axial direction since the flow is bounded by four solid walls. This feature makes Asmolov solution unable to capture the correct properties of rectangular channel flows. Furthermore, shear gradient induced and wall induced inertial lift forces are only two dominant forces in a plane Poiseuille flow, however, Saffman inertial lift force significantly comes into picture for rectangular channels and alters the focusing mechanism in rectangular channels. Moreover, for a rectangular cross-section channel, 4 equilibrium points near channel cross-section corners are predicted using Asmolov inertial lift. On the contrary, different experimental studies carried out for straight rectangular channels [72–74], show two equilibrium positions on the short axis of the channel. These observations clearly confirm inability of Asmolov inertial lift model for prediction of correct equilibrium positions in a 3D Poiseuille flow.

Recently, a study carried out by Hood *et. al.* [42] could obtain inertial lift force acting on a spherical particle in a 3D Poiseuille flow. Derivation of inertial force was performed for a straight channel with square cross-section using asymptotic theory. Resultant inertial lift force field acting on a spherical particle using Hood solution can be seen in Figure 2.2-(b). Again, blue arrays indicate the inertial lift force direction and magnitude, red circles and black circles indicate stable and unstable equilibrium points. Comparison of figures **??** and **??** clearly shows that stable points achieved using Hood study is practically the same as unstable points predicted by Asmolov study extended to square channel. This issue can be justified considering effect of different inertial lift forces. Shear gradient induced

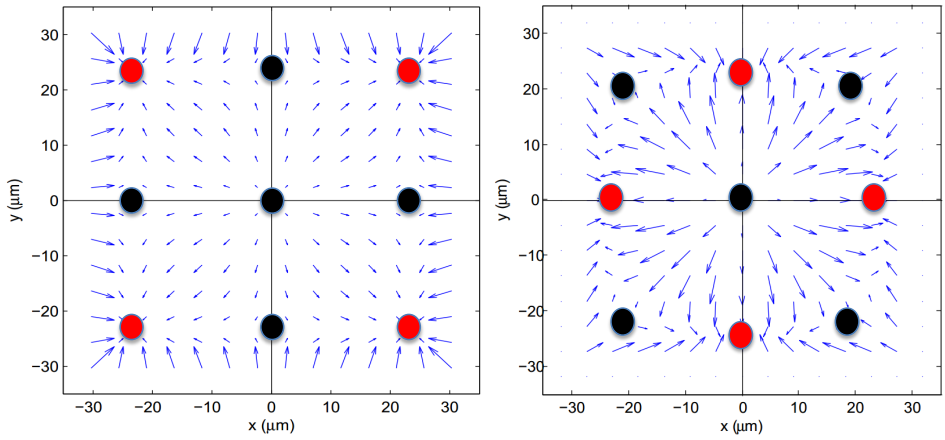

Figure 2.2: Inertial force field together with stable and unstable equilibrium points in square channel: **(a)** Asmolov's study, **(b)** Hood's study

and wall induced lift forces which are dominant forces cause the particles settle in spaces between channel centerline and walls. In Asmolov solution which only considers shear gradient and wall induced lift forces, these spaces would be the final positions of particles. However, in a square channel in addition to two aforementioned forces, Saffman force also comes into picture and alters the positions of particles due to the effect of shear gradient and wall induced lift forces. Finally, predicted stable positions by shear gradient and wall effects become unstable and cause particles migrate to new stable positions. Further experimental studies using a combination of sub-pixel accurate particle tracking and velocimetric reconstruction of the depth dimension was conducted by Hood [43] for a straight rectangular channel with aspect ratio of 2 shows well agreement of the experimental results with solution obtained using asymptotic theory. More recently, the inertial lift force for a single spherical particle in rectangular cross-section channel with different aspect ratios has been derived using direct numerical simulation [70]. In this study, the inertial lift variation is investigated on different axes of the channel and finally the results are utilized for particle tracking using Lagrangian particle tracking method in spiral and serpentine channels and excellent agreement is reported for simulation and experiment results.

2.1.6 Formulation for Particle Tracking

In this section, particle tracking formulations are presented using specific expressions for the force elements. As it was discussed formerly, Crank-Nicolson temporal integration method is superior in comparison with explicit and implicit Euler's method in terms of accuracy and stability. Due to the presence of unknown values in Crank-Nicolson formulation, it is hard to implement the general expression for the drag force [81] in the formulation. For this purpose, we use Stokes drag force in our formulation to be able to use Crank-Nicolson method. It is acceptable to use Stokes drag since the lateral migration velocity of particles is relatively small which results in small relative Reynolds number for particle. It may seem not acceptable to implement Stokes drag in the axial direction of straight channel due to high flow rate. To justify this issue, we assume that the particle is released at the inlet with the same velocity as fluid. By this assumption, the relative velocity of particle with respect to fluid element in axial direction becomes relatively small and makes the exploitation of Stokes drag for axial direction acceptable. Moreover, due to the same density of particle and fluid medium, the body forces are neglected. Consequently, same density is considered for both particle and fluid medium and the density ratio is considered as unity.

2.1.7 Formulation in Cartesian Coordinates

Drag force using Stokes expression can be written as:

$$\mathbf{F_D}^k = 6\pi\mu R_p(\mathbf{u_f}^k - \mathbf{u_p}^k) \tag{2.41}$$

The temporal derivative of the fluid element velocity can be approximated using a backward finite difference scheme:

$$\frac{d\mathbf{u_f}^k}{dt} = \frac{\mathbf{u_f}^k - \mathbf{u_f}^{k-1}}{\Delta t} \tag{2.42}$$

Now, the function $\mathbf{G}$ at the step k can be written as:

$$\mathbf{G}^k = \frac{2}{3}\left(\frac{1}{M_p}6\pi\mu R_p(\mathbf{u_f}^k - \mathbf{u_p}^k) + \frac{1}{M_p}\mathbf{F_L}^k + \frac{1}{2}\frac{\mathbf{u_f}^k - \mathbf{u_f}^{k-1}}{\Delta t}\right) \tag{2.43}$$

Similarly, the expression for $\mathbf{G}^{k+1}$ can be written as:

$$\mathbf{G}^{k+1} = \frac{2}{3}\left(\frac{1}{M_p}6\pi\mu R_p(\mathbf{u_f}^{k+1} - \mathbf{u_p}^{k+1}) + \frac{1}{M_p}\mathbf{F_L}^{k+1} + \frac{1}{2}\frac{\mathbf{u_f}^{k+1} - \mathbf{u_f}^{k}}{\Delta t}\right) \tag{2.44}$$

By substituting the Eq. (2.43) and (2.44) into the Eq. (2.19) we obtain:

$$\begin{aligned}\mathbf{u_p}^{k+1} = \mathbf{u_p}^{k} + \frac{1}{3}\Bigg(\frac{1}{M_p}6\pi\mu R_p(\mathbf{u_f}^{k} + \mathbf{u_f}^{k+1} - \mathbf{u_p}^{k} - \mathbf{u_p}^{k+1}) + \frac{1}{M_p}(\mathbf{F}_L^k + \mathbf{F}_L^{k+1}) + \\ \frac{1}{2}\frac{\mathbf{u_f}^{k+1} - \mathbf{u_f}^{k-1}}{\Delta t}\Bigg)\Delta t\end{aligned} \tag{2.45}$$

By rearranging the equation above according to the particle velocity we can obtain:

$$\begin{aligned}\mathbf{u_p}^{k+1} = \frac{1}{1 + \frac{1}{3}\frac{1}{M_p}6\pi\mu R_p\Delta t}\Bigg[\mathbf{u_p}^{k} + \frac{1}{3}\Bigg(\frac{1}{M_p}6\pi\mu R_p(\mathbf{u_f}^{k} + \mathbf{u_f}^{k+1} - \mathbf{u_p}^{k}) + \\ \frac{1}{M_p}(\mathbf{F}_L^k + \mathbf{F}_L^{k+1}) + \frac{1}{2}\frac{\mathbf{u_f}^{k+1} - \mathbf{u_f}^{k-1}}{\Delta t}\Bigg)\Delta t\Bigg]\end{aligned} \tag{2.46}$$

Finally, Eq. (2.20) is utilized for updating the particle location.

2.1.8 Formulation in Cylindrical Coordinate

Fluid element acceleration in cylindrical coordinates using acceleration formulations can be written as:

$$\begin{aligned} a_{fr} &= \dot{u}_{fr} - \frac{u_{f\theta}^2}{r} \\ a_{f\theta} &= \dot{u}_{f\theta} + \frac{u_{fr}u_{f\theta}}{r} \\ a_{fz} &= \dot{u}_{fz} \end{aligned} \tag{2.47}$$

By implementation of Stokes drag expression, we can write:

$$\begin{aligned} \dot{u}_{pr} - \frac{u_{p\theta}^2}{r} &= \frac{2}{3}\left[\frac{1}{M_p}6\pi\mu R_p(u_{fr} - u_{pr}) + \frac{1}{M_p}F_{Lr} + \frac{1}{2}\left(\dot{u}_{fr} - \frac{u_{f\theta}^2}{r}\right)\right] \\ \dot{u}_{p\theta} + \frac{u_{pr}u_{p\theta}}{r} &= \frac{2}{3}\left[\frac{1}{M_p}6\pi\mu R_p(u_{f\theta} - u_{p\theta}) + \frac{1}{M_p}F_{L\theta} + \frac{1}{2}\left(\dot{u}_{f\theta} + \frac{u_{fr}u_{f\theta}}{r}\right)\right] \\ \dot{u}_{pz} &= \frac{2}{3}\left[\frac{1}{M_p}6\pi\mu R_p(u_{fz} - u_{pz}) + \frac{1}{M_p}F_{Lz} + \frac{1}{2}\dot{u}_{fz}\right] \end{aligned} \tag{2.48}$$

The equations above can be arranged to be written as:

$$\dot{u}_{pr} = \frac{2}{3}\left[\frac{1}{M_p}6\pi\mu R_p(u_{fr} - u_{pr}) + \frac{1}{M_p}F_{Lr} + \frac{1}{2}\left(\dot{u}_{fr} - \frac{u_{f\theta}^2}{r}\right)\right] + \frac{u_{p\theta}^2}{r} = G_r$$
$$\dot{u}_{p\theta} = \frac{2}{3}\left[\frac{1}{M_p}6\pi\mu R_p(u_{f\theta} - u_{p\theta}) + \frac{1}{M_p}F_{L\theta} + \frac{1}{2}\left(\dot{u}_{f\theta} + \frac{u_{fr}u_{f\theta}}{r}\right)\right] - \frac{u_{pr}u_{p\theta}}{r} = G_\theta$$
$$\dot{u}_{pz} = \frac{2}{3}\left[\frac{1}{M_p}6\pi\mu R_p(u_{fz} - u_{pz}) + \frac{1}{M_p}F_{Lz} + \frac{1}{2}\dot{u}_{fz}\right] = G_z \tag{2.49}$$

By evaluation of G functions, the equations above can be written as:

$$u_{pr}^{k+1} = u_{pr}^k + \left[\frac{1}{3}\left(\frac{1}{M_p}6\pi\mu R_p(u_{fr}^{k+1} - u_{pr}^{k+1} + u_{fr}^k - u_{pr}^k\right) + \frac{1}{M_p}\left({F_{L_r}}^{k+1} + {F_{L_r}}^k\right)$$
$$+\frac{1}{2}\left((\dot{u}_{fr} - \frac{u_{f\theta}^2}{r})^{k+1} + (\dot{u}_{fr} - \frac{u_{f\theta}^2}{r})^k\right)\right) + \frac{1}{2}\left((\frac{u_{p\theta}^2}{r})^{k+1} + (\frac{u_{p\theta}^2}{r})^k\right)\Bigg]\Delta t$$
$$u_{p\theta}^{k+1} = u_{p\theta}^k + \left[\frac{1}{3}\left(\frac{1}{M_p}6\pi\mu R_p(u_{f\theta}^{k+1} - u_{p\theta}^{k+1} + u_{f\theta}^k - u_{p\theta}^k\right) + \frac{1}{M_p}({F_{L_\theta}}^{k+1} + {F_{L_\theta}}^k)\right.$$
$$\left.+\frac{1}{2}\left(\dot{u}_{f\theta}^{k+1} + \frac{u_{fr}^{k+1}u_{f\theta}^{k+1}}{r^{k+1}} + \dot{u}_{f\theta}^k + \frac{u_{fr}^k u_{f\theta}^k}{r^k}\right)\right]\Delta t$$
$$u_{pz}^{k+1} = u_{pz}^k + \frac{1}{3}\left[\frac{1}{M_p}6\pi\mu R_p\left(u_{fz}^{k+1} - u_{pz}^{k+1} + u_{fz}^k - u_{pz}^k\right) + \right.$$
$$\left.\frac{1}{M_p}\left({F_{L_z}}^{k+1} + {F_{L_z}}^k\right) + \frac{1}{2}\left(\dot{u}_{fz}^{k+1} + \dot{u}_{fz}^k\right)\right]\Delta t \tag{2.50}$$

The first two equations above are non-linear coupled equations. To solve the equation for new step velocity, a modified Newton-Raphson method was implemented. Velocity values at the previous step were assigned as an initial guess for the method. Finally, the particle position can be updated using Eq. (2.36).

2.2 Model Verification

In this section, the authenticity of developed computational model is examined. For this purpose, the experimental results from a case study research paper in the literature [75] are compared with our computational results. In the mentioned

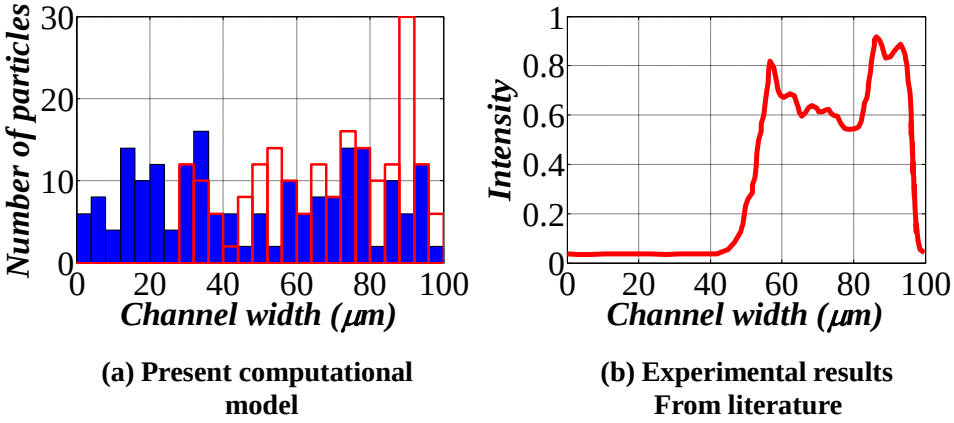

(a) Present computational model

(b) Experimental results From literature

Figure 2.3: Comparison of particle distribution for 1.9 μm particles

paper, a spiral micro-channel with rectangular cross-section is studied. The spiral cross-section has a width of 100 μm and width of 50 μm. The starting radius of the spiral is 3 mm and the spacing between two adjacent turns is 200 μm. The spiral channel consists of five turns. For this purpose, a spiral channel with mentioned characteristics is modeled. The flow field at the absence of particles is first simulated with FEM based simulation environment COMSOL Multi-physics. Finally, using computational model discussed in the former section, the particle tracking is carried out. 100 particles are released at the inlet with a random distribution. The simulation is carried out for the upper half of the channel due to the symmetry in the height. The same velocity as fluid elements is assigned for particles at the inlet to ensure a low relative Reynolds number. For the channel inlet, laminar inflow with flow rate of 0.6 mL/h is assigned in accordance to the experimental conditions. No-slip velocity boundary condition and zero pressure are assigned for the channel walls and channel outlet respectively. According to the experiment, two different size particles with size of 1.9 and 7.2 μm are considered for the simulation.

Figures 2.3 and 2.4 show the comparison between simulation and experimental results of [75] for 1.9 μm and 7.2 μm particles respectively. As it can be observed, our model is able to predict the particle behavior and focusing pattern. According to the experimental results, smaller particles tend to focus near the outer wall of channel and larger particles tend to focus in the vicinity of inner channel wall

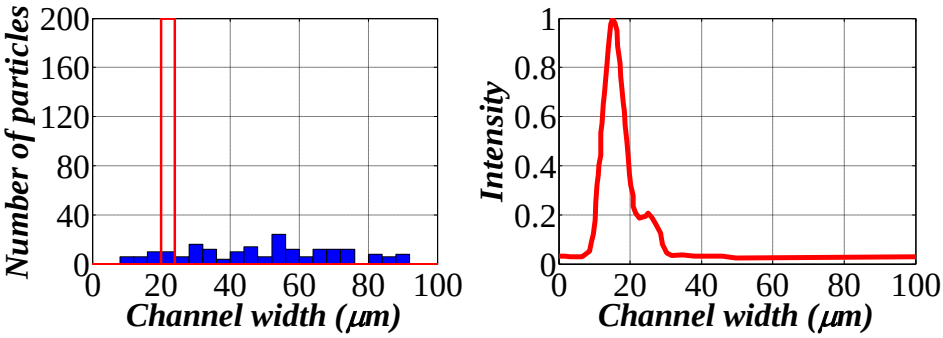

(a) Present computational model

(b) Experimental results From literature

Figure 2.4: Comparison of particle distributio for 7.2 μm particles

which is well predicted by our computational model.

2.3 Computational Results

The validity of the our developed computational model was examined and confirmed in the former section for a specific case study. In this section, using our computational model, we have simulated different cases for particle tracking. The simulations are carried out both for straight and spiral channels with different aspect ratios to investigate the focusing pattern of different size particles both at the presence and absence of channel curvature. Furthermore, the simulations are performed for different flow rates and consequently different channel Reynolds number to investigate the relation of Reynolds number with focusing pattern and mechanism of particles.

2.3.1 Numerical Parameters

The governing equations of motion for a steady-state, incompressible, laminar and Newtonian fluids can be written as:

$$\boldsymbol{\nabla} \cdot \boldsymbol{u} = 0, \tag{2.51}$$

$$\boldsymbol{u} \cdot \boldsymbol{\nabla} \boldsymbol{u} = \frac{1}{\rho} \partial_x p + \nu \boldsymbol{\nabla}^{\mathbf{2}} \boldsymbol{u}, \tag{2.52}$$

where $\boldsymbol{u}$ is the velocity field, p is the pressure field, ρ is the fluid medium density and ν is the dynamic viscosity of fluid. The equations above are solved in computational fluid dynamics commercial software COMSOL multiphysics. Laminar inflow with the specified flow rate is assigned at the channel inlet, zero pressure is assigned at the channel outlet and no-slip velocity boundary condition is assigned as boundary conditions for the channel walls. The fluid properties are assigned the same as water from COMSOL library. If the flow is symmetric in the height direction, half of the channel can be simulated with symmetry boundary condition. Free triangular grids with custom properties as with maximum element size of 5 μm, minimum element size of 1 μm, maximum element growth rate of 1.2, curvature factor of 0.7 and resolution of narrow regions of 0.6 are utilized to generate mesh for the channel inlet. Finally, using swept option, the generated mesh is created along the channel. The flow data is used through MATLAB-COMSOL LiveLink interface. For the particle tracking, the selection of time step is dependent on the channel flow rates. For low flow rates, a smaller time step needs to be assigned since the particle motion is slower in comparison with higher flow rates.

2.3.2 Straight Channel with AR 2

In this part, we intend to discuss about the focusing of different size particles in straight rectangular micro-channels with aspect ratio of 2. The micro-channel has a width of 100 μm and height of 50 μm. The length of channel was considered as 20 cm. Flow rates of 0.6 mL/h, 2 mL/h, 5 mL/h and 10 mL/h which correspond to channel Reynolds numbers of 3, 11, 27 and 55 respectively are assigned for the inlet. In order to reduce the computational time, just a short length of micro-channel is simulated in COMSOL and the data is used for the rest of micro-channel due to fully developed velocity profile. Two different size particles with the size of 1.9 and 7.2 μm are released with a random distribution at the inlet with the same velocity as fluid flow. For each case, 100 particles are released. The channel design and also selection of particle size are taken from a paper in

literature [75] for a spiral channel. The purpose of this section is to investigate the focusing pattern of different size particles in straight channel with aspect ratio 2.

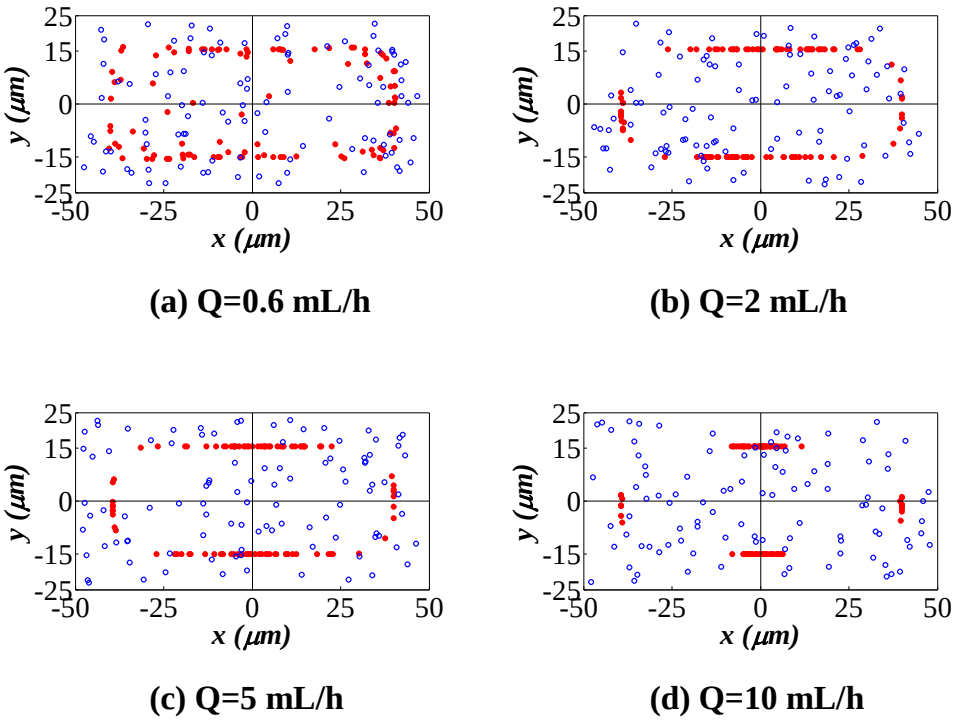

Figure 2.5: Particle distributions at the inlet and the outlet cross-sections for different flow rates (Straight channel with AR 2, 1.9 μm particles)

Particles spatial positions inside the micro-channel for 1.9 μm and 7.2 μm can be observed in Figure 2.5 and 2.7 respectively. In these figures, the hollow blue circles show the initial position of particles at the inlet and solid red circles show the final position of particles at the outlet. The outlet is placed at the end of 20 cm length of the channel. In order to get a better picture about particle spatial distribution, bar plots for particle distribution both in width and height of channel are depicted in Figures 2.6 and 2.8 for 1.9 and 7.2 μm particles respectively. In these figures, hollow red bars indicate the particle distribution at the outlet and solid blue bars show the particles position at the inlet of the channel. The different mechanisms for different size particles can be clearly observed in these figures. For 1.9 μm particle which can be considered as small particle size, focusing process is much slower in comparison with the 7.2 μm particles which is larger in size. With

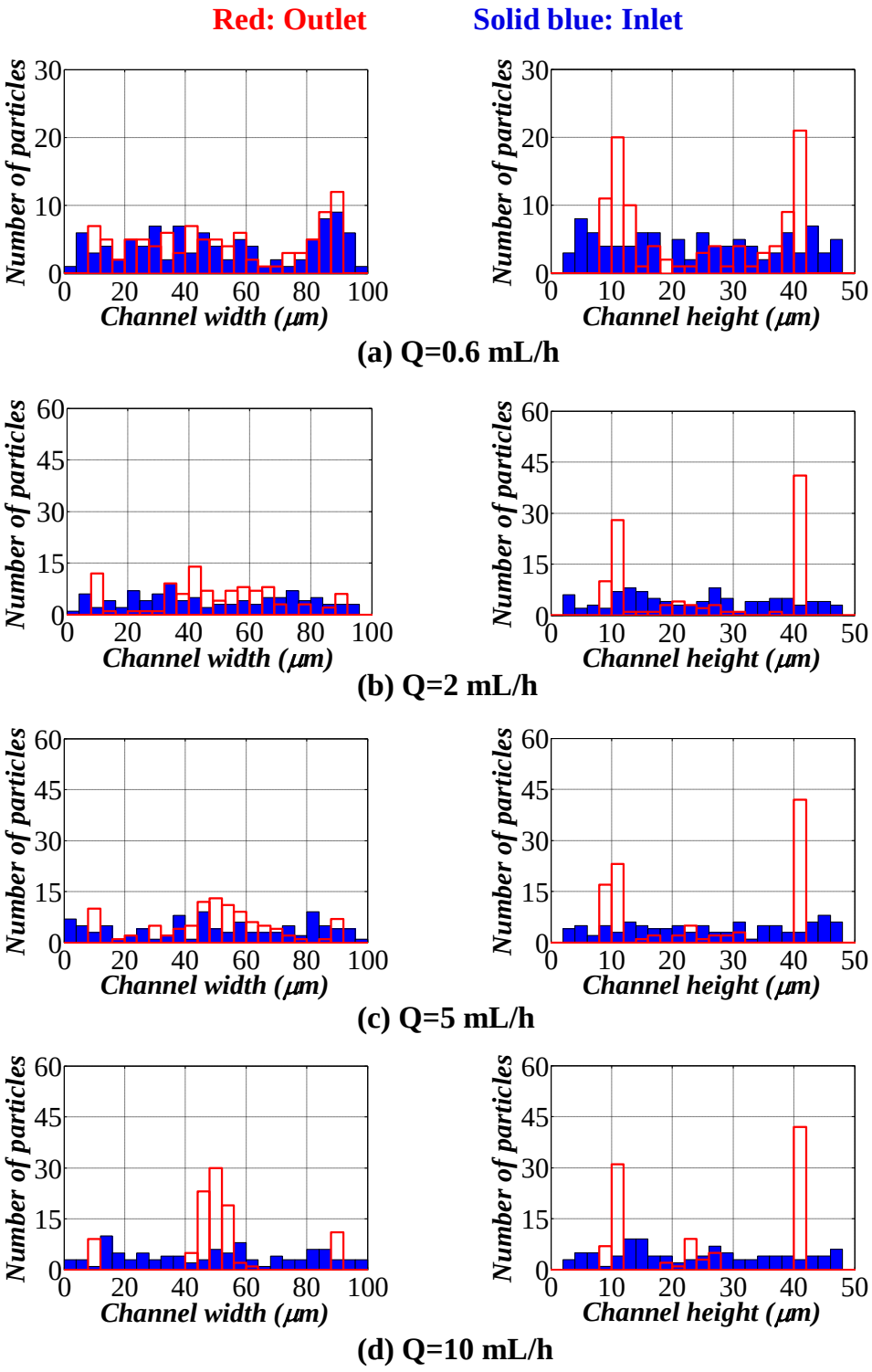

Figure 2.6: Particle distribution at the inlet and the outlet in the height and width directions for different flow rates (Straight channel with AR 2, 1.9 μm particles)

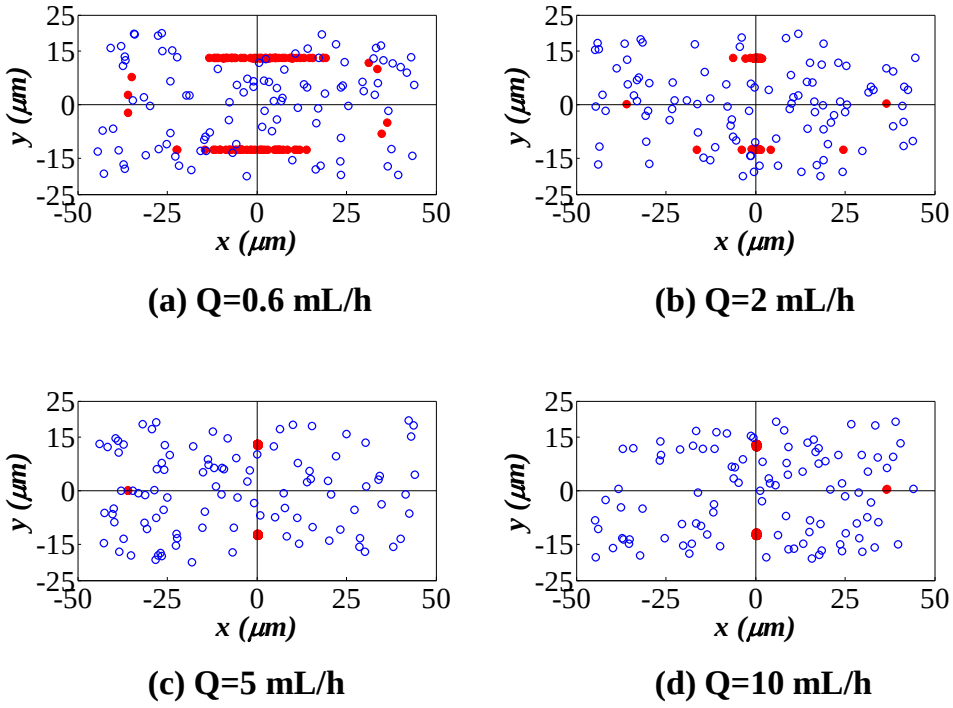

Figure 2.7: Particle distributions at the inlet and the outlet cross-sections for different flow rates (Straight channel with AR 2, 7.2 μm particles)

the same flow rate, larger particles are focused much faster than smaller particles due to the higher inertial lift force acting on larger particles. Higher inertial lift force causes particles migrate faster in the lateral direction and consequently makes the focusing process faster. Another important observation that can be made from these figures is the focusing of particles in height and width of the channel. As it can be clearly seen, particle focusing in height of channel is much faster than the width of channel. In Figure 2.5 and 2.6 which is the cross sectional view for 1.9 μm particles, efficient focusing in height of channel is achieved with low flow rate, however, no focusing can be observed in the width of channel. Furthermore, by increasing the flow rate, an improvement can be observed in the focusing in width of channel. It is due to this fact that by increasing the flow rate, channel Reynolds number increases. Consequently, inertial lift force which is a function of channel Reynolds number increases and finally the lateral migration velocity of particles rises in magnitude. Final observation can be made about the position of focusing for particles in a rectangular channel with aspect ratio of 2.

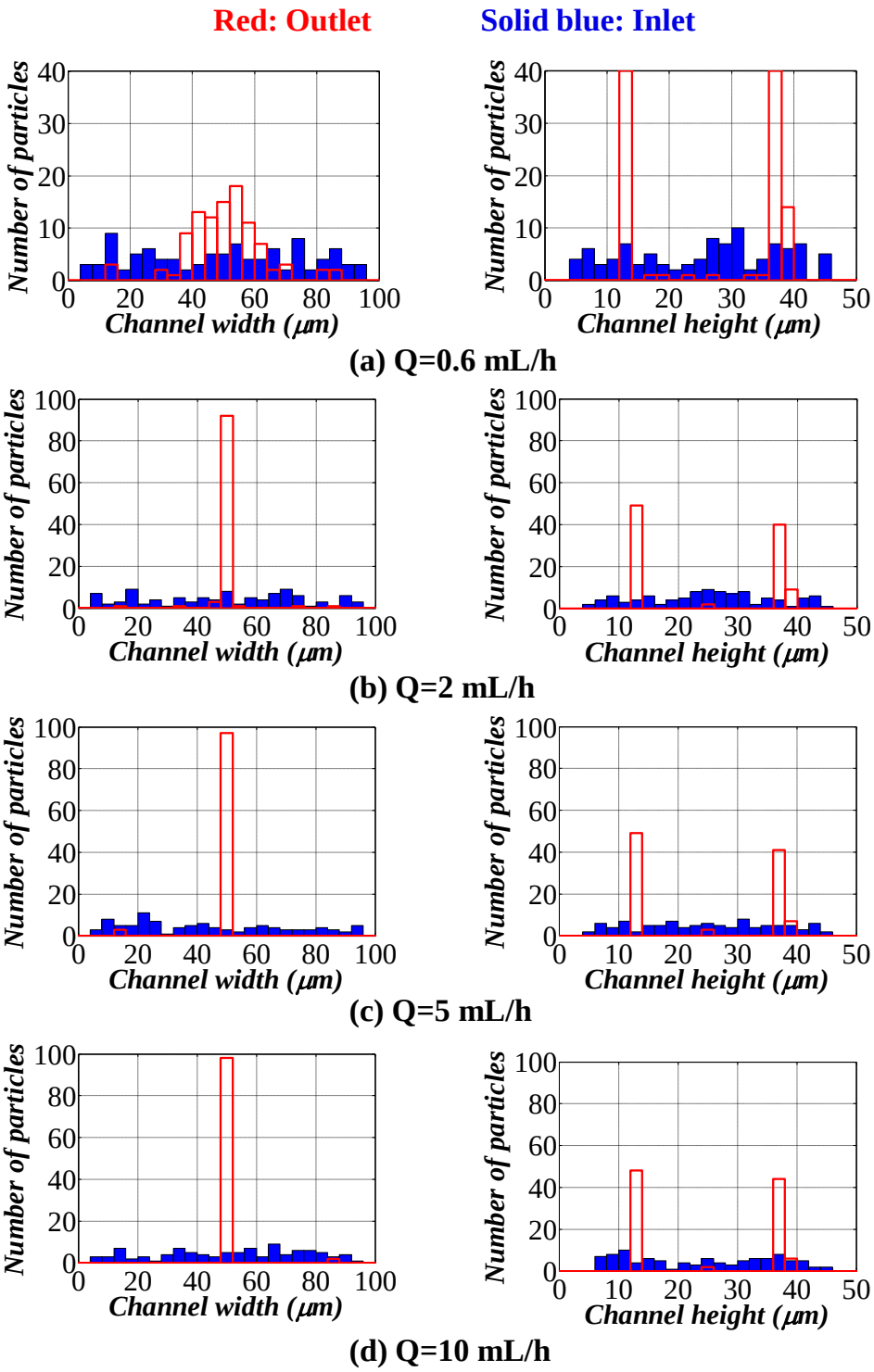

Figure 2.8: Particle distribution at the inlet and the outlet in the height and width directions for different flow rates (Straight channel with AR 2, 7.2 μm particles)

According to the aforementioned figures, both 1.9 and 7.2 μm particles intend to focus on the short axis of the channel. Larger particles focus on the short axis and a little lower in height than smaller particles. This fact shows the inefficiency of straight channel with aspect ratio 2 in separating different size particles.

2.3.3 Straight Channel with AR 9

In this part the simulation results of particle focusing in a rectangular straight channel with aspect ratio 9 for different particle sizes are discussed. The straight channel has a width of 450 μm and height of 50 μm. Two different particle with sizes of 2 and 10 μm are considered for the simulation. Analogous to the previous simulation for aspect ratio 2, a short length of the channel was modeled in COMSOL Multi-physics and the data was used for the rest of the channel. Laminar inflow with flow rates of 10 mL/h, 20 mL/h, 40 mL/h, 80 mL/h and 120 mL/h which correspond to channel Reynolds number of 16, 33, 66, 133 and 200 respectively are assigned for the inlet. It is worth mentioning that in order to reduce the computational effort of COMSOL, just a quarter of the channel is modeled due to the symmetry.

Figures 2.9 and 2.11 show the inlet and outlet cross section of the channel for 2 μm and 10 μm particles respectively. In order to have a better picture of particle distribution, bar plots for spatial distribution of particles both for inlet and outlet are depicted in Figures 2.10 and 2.12 for 2 and 10 μm respectively. One of the interesting observations that can be made is the focusing position of different size particles. As it can be clearly seen in bar plots, 2 μm particles tend to focus on the short axis of the channel, however, 10 μm particles tend to focus on the long axis of the channel. Focusing quality in width of the channel for both particle sizes is low for low flow rates, however, focusing is virtually achieved in height of channel for both particle sizes even at low flow rates. Due to the high aspect ratio of the channel, the velocity in the width direction is virtually uniform except for the region in the vicinity of the vertical walls. Semi uniform velocity profile (Figure 2.13) has a very small velocity gradient in that direction, and it results in very small inertial lift force. On the other hand, due to the infinity

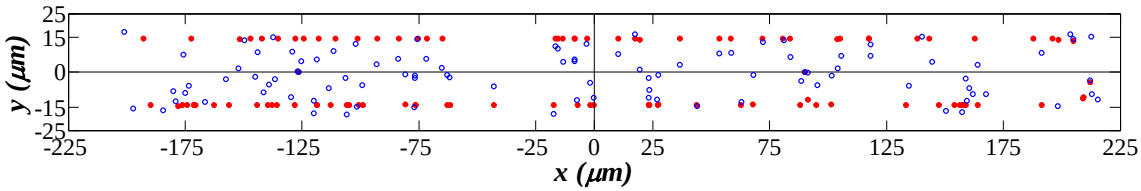

(a) Q=10 mL/h

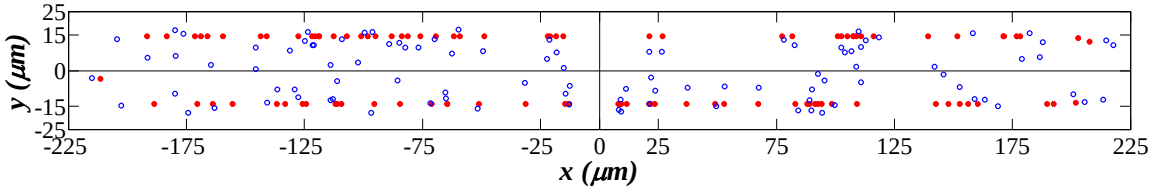

(b) Q=20 mL/h

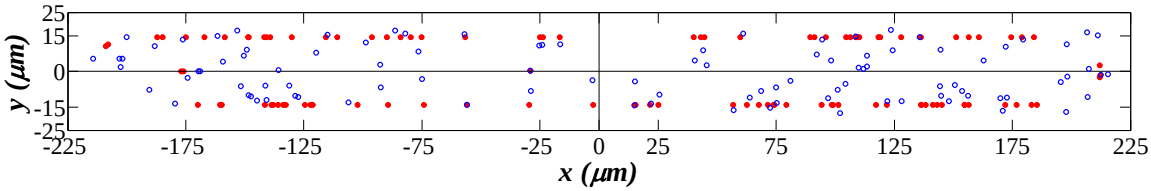

(c) Q=40 mL/h

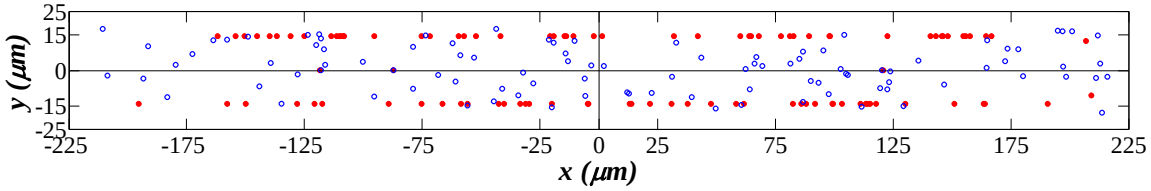

(d) Q=80 mL/h

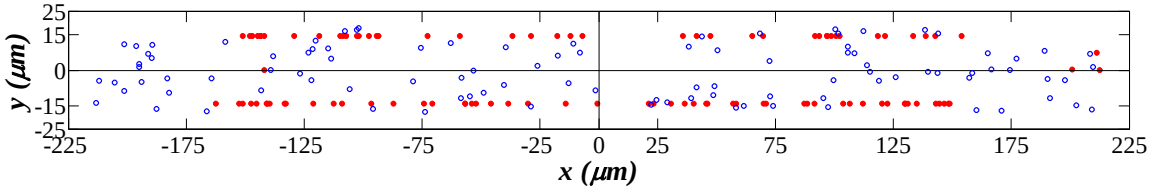

(e) Q=120 mL/h

Figure 2.9: Particle distribution at the inlet and the outlet in the height and width directions for different flow rates (Straight channel with AR 9, 2 μm particles)

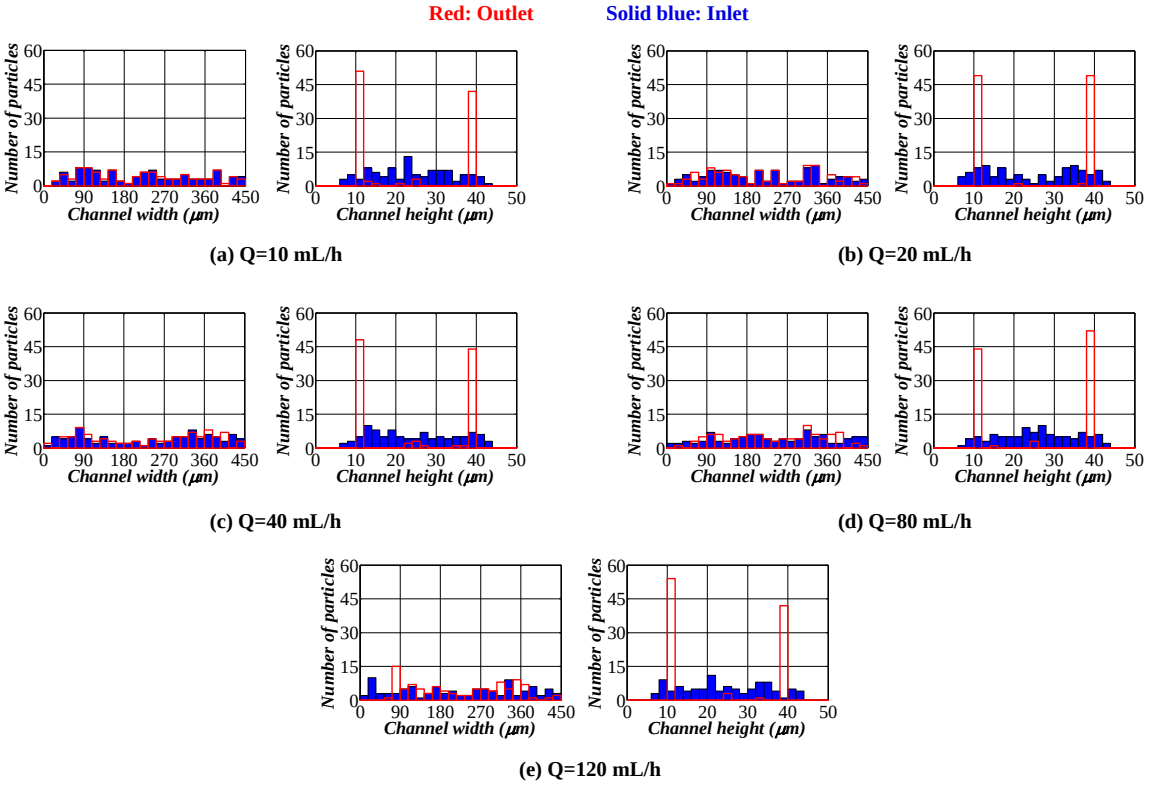

Figure 2.10: Particle distribution at the inlet and the outlet in the height and width directions for different flow rates (Straight channel with AR 9, 2 μm particles)

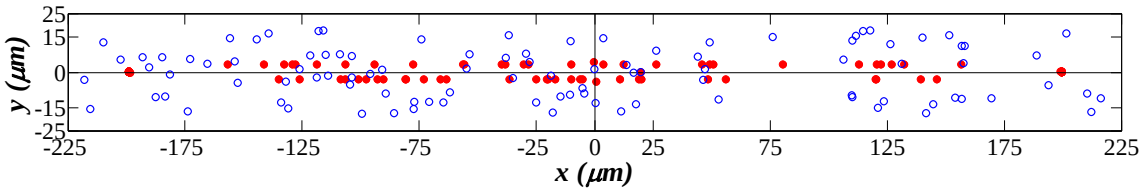

(a) Q=10 mL/h

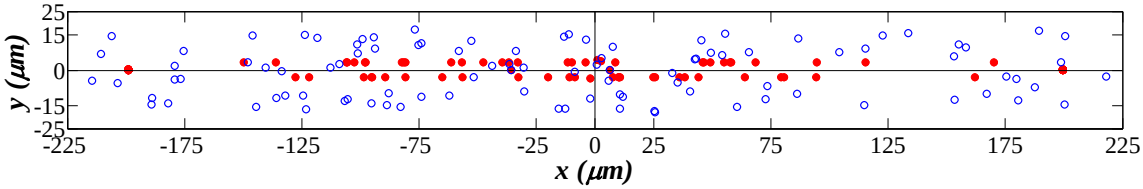

(b) Q=20 mL/h

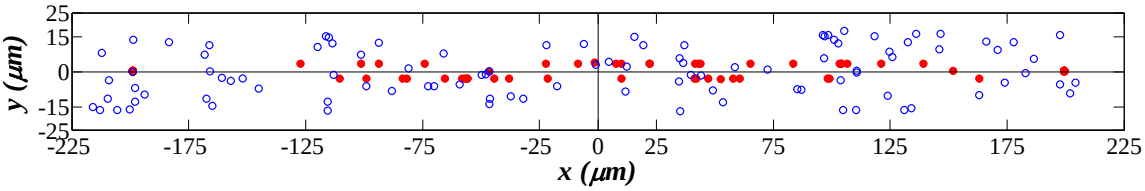

(c) Q=40 mL/h

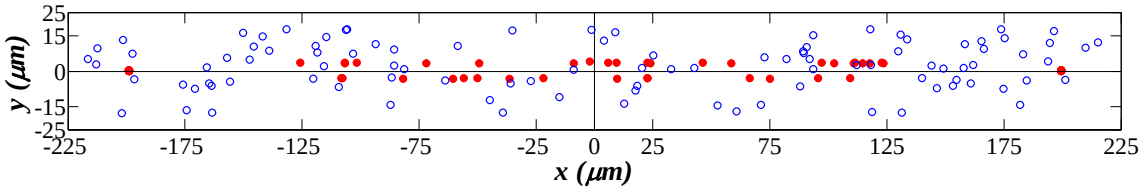

(d) Q=80 mL/h

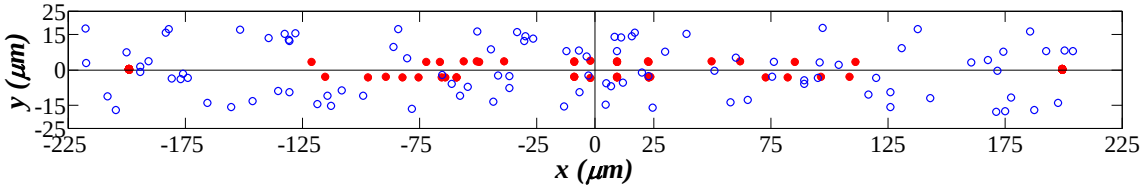

(e) Q=120 mL/h

Figure 2.11: Particle distribution at the inlet and the outlet in the height and width directions for different flow rates (Straight channel with AR 9, 10 μm particles)

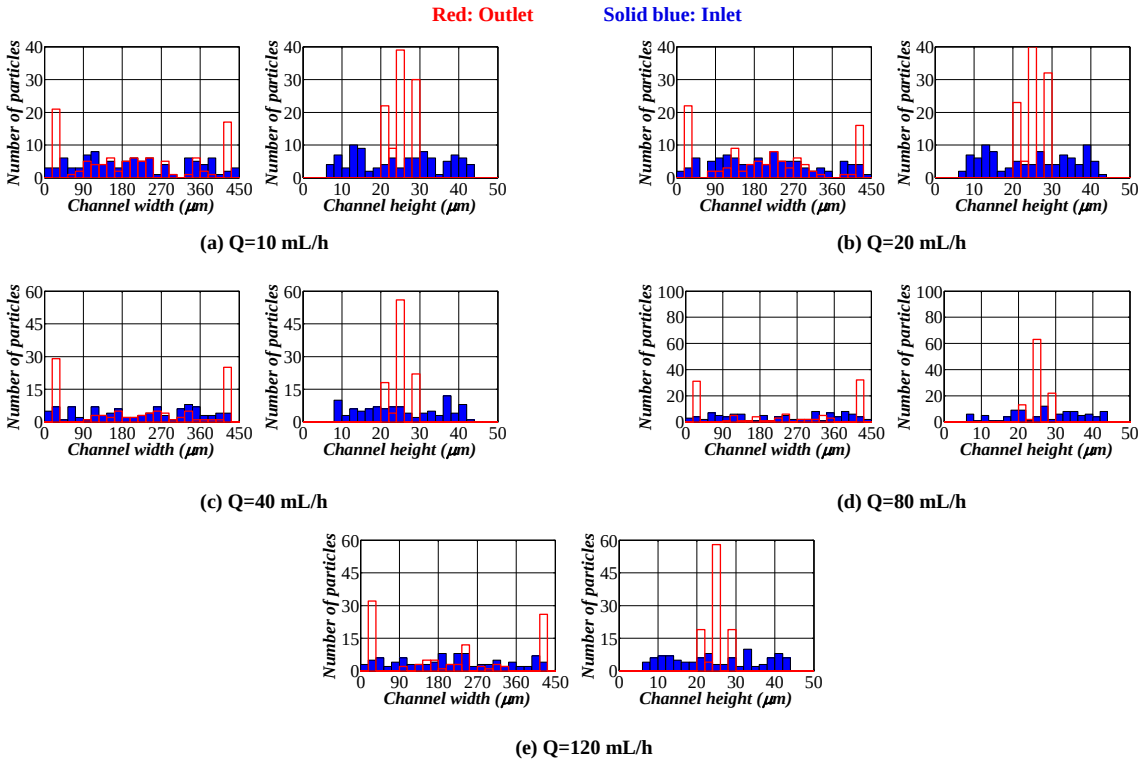

Figure 2.12: Particle distribution at the inlet and the outlet in the height and width directions for different flow rates (Straight channel with AR 9, 10 μm particles)

in radius of curvature in straight channels, there is no Dean flow in the cross section. The inertial lift force is the only force acting on the particle. That is why we do not observe high quality focusing in the width direction especially for the small size particles. In height of the channel due to the high velocity gradient, particle focusing is practically achieved. In order to increase the inertial lift force especially for the small particles which results in higher lateral migration velocity, channel Reynolds number can be increased. Improvement of focusing mechanism by increasing channel Reynolds number is more effective for the larger particles in comparison with smaller particles. It can be deduced that for high aspect ratio micro-channels, focusing mechanism in width of the channel for particles which are in the vicinity of channel vertical walls is fast due to high velocity gradient in width direction. Furthermore, for the particles which are away from the channel vertical walls, focusing mechanism in width direction is too slow especially for the small particles due o the semi uniform velocity profile in width direction and consequently low inertial lift force which results in low migration velocity in width direction. According to these observation one suggestion can be made for particle separation in straight channels. A high aspect ratio rectangular straight channel with greater height than width can be fabricated. For instance a design similar to the simulated channel in this section but with height of 450 μm and width of 50 μm. This channel design may encounter some difficulties in the fabrication process, however, it can be considered as an efficient particle separator chip. In this design, three different outlet can be placed. larger particles can be collected from the center of the channel, while smaller particles can be collected from two side corners of the channel.

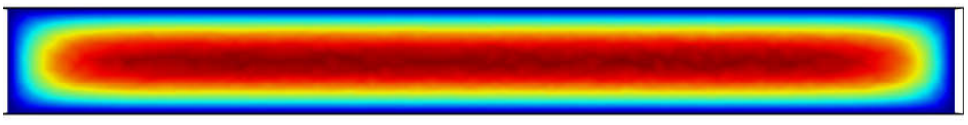

Figure 2.13: Velocity profile at the cross section of the channel: semi-uniform velocity profile can be observed in the width direction

2.3.4 Spiral Channel with AR 2

In this section, we have done the simulation of particle focusing for two different size particles. The study corresponds to a spiral channel with rectangular cross section. This cross section has a width of 100 μm and height of 50 μm. The starting radius of the spiral is 3 mm and the spacing between two adjacent spiral turns is 200 μm. The simulations are carried out for 4 different flow rates which corresponds to 4 different channel Reynolds number. Particles with the size of 1.9 and 7.2 μm are considered for the simulation. As it was mentioned formerly, the channel design and particle size are taken from a literature research paper [75]. In each simulation 100 particles are released from the inlet of channel with a random distribution. The simulation is only performed for the upper half of the spiral channel due to the symmetry and finally the results were copied symmetrically for the lower half of the channel.

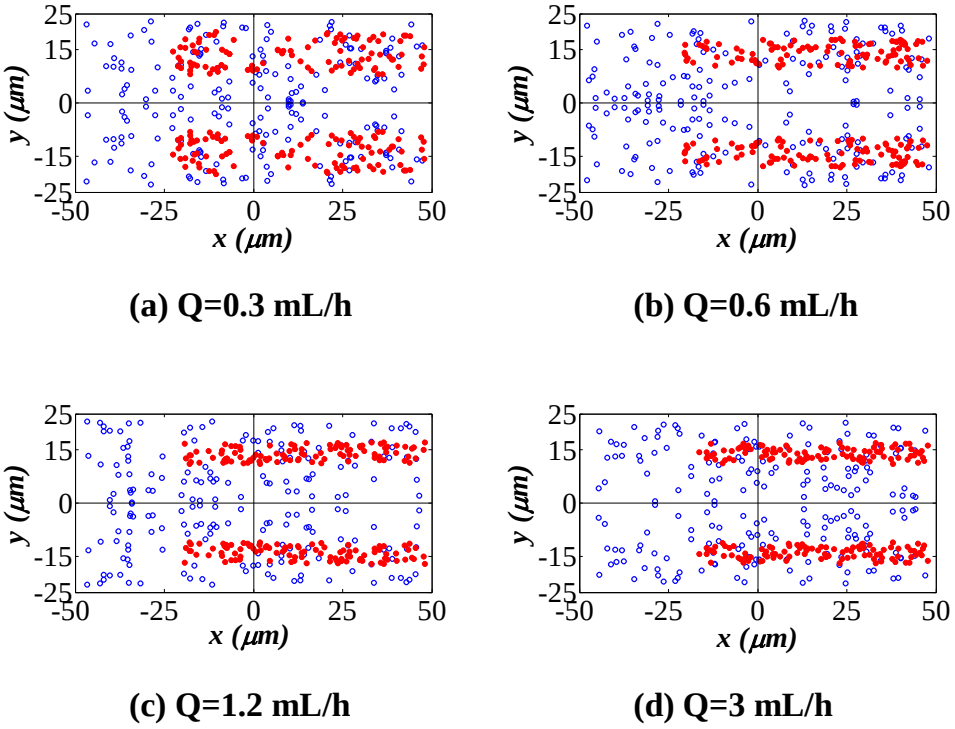

Figure 2.14: Particle distribution at the inlet and the outlet in the height and width directions for different flow rates (Spiral channel with AR 2, 1.9 μm particles)

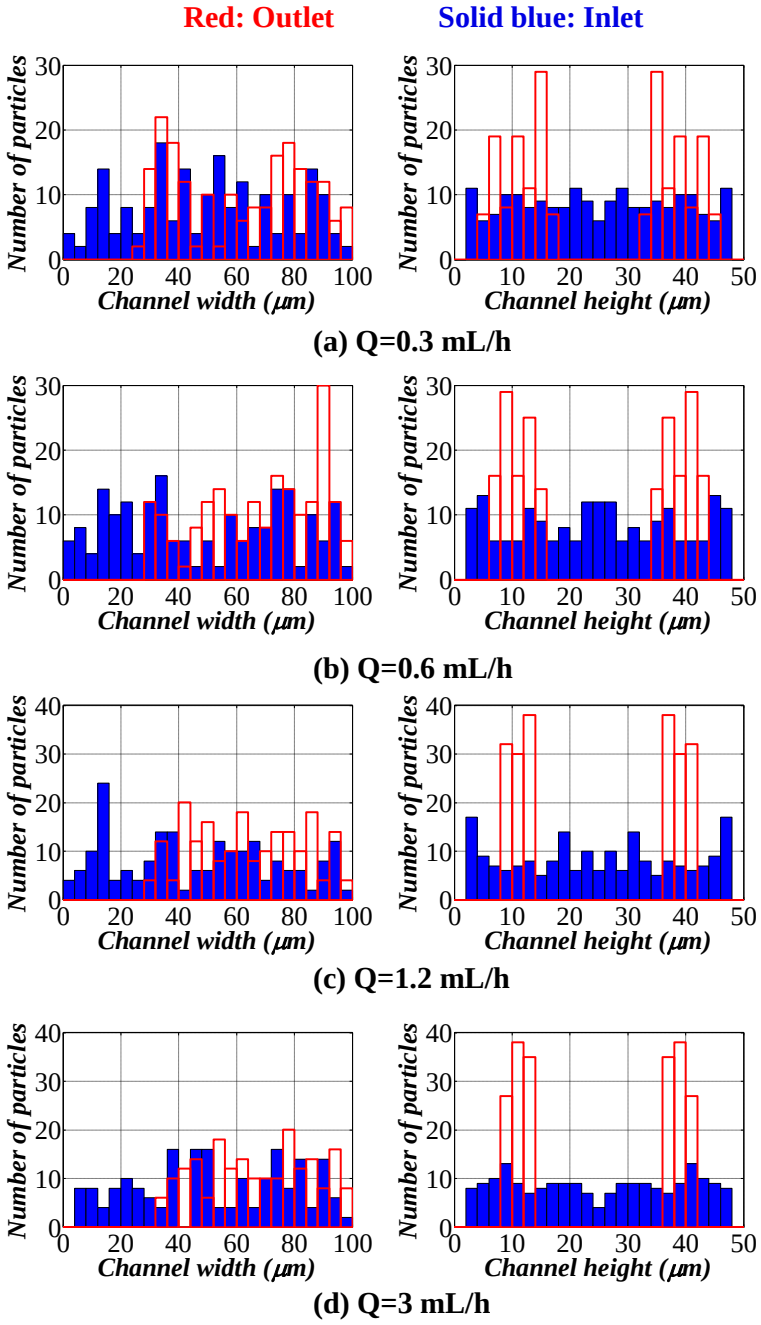

Figure 2.15: Particle distribution at the inlet and the outlet in the height and width directions for different flow rates (Spiral channel with AR 2, 1.9 μm particles)

Figure 2.14 shows the cross section of inlet and outlet of the spiral channel. In order to make the figure clear and not crowded, the size of the circles in these figures was not set as the real size of particles and only show the position of particle centers in the cross section. 4 different flow rates of 0.3, 0.6, 1.2 and 3 mL/h are used which correspond to channel Reynolds number of 1.67, 3.34, 6.67 and 16.67 respectively. According to the Figure 2.14, the simulation shows that for the low Reynolds number flows (flow rates 0.3 and 0.6 mL/h) the focusing in height of the channel can not be achieved for the 1.9 μm particles, however, the focusing in the width is practically achieved. In curved micro-channels due to the existence of non zero radius of curvature, a velocity mismatch occurs for the fluid elements in the vicinity of the channel walls and central core. The mentioned velocity mismatch creates two symmetric circulating vortices in cross section of the channel. The presence of the mentioned vortices which are known as Dean or secondary flow vortices, exerts a drag force known as Dean drag on the particles. The existence of Dean drag can be considered as a basis and plays a substantial role for size based particle separation and fast focusing process. The focusing mechanism in curved micro-channels can be justified considering the interaction between inertial lift force and Dean vortices. As it was observed for straight channel, lateral migration velocity is solely dependent on the magnitude of inertial lift forces acting on the particles. Therefore, the focusing mechanism of particles at the presence of Dean flow can be explained on the balance of these two forces. Magnitude of these forces is the key point in determination of the possibility and position of equilibrium points.

As it can be observed in Figure 2.14 which is the cross sectional view of channel inlet and outlet for 1.9 μm particles and also in Figure 2.15 which is the bar plot for spatial distribution of 1.9 μm particles, focusing of particles is practically achieved, however, the focusing quality is not high. In this case, instead of focusing line we observe a focusing region for 1.9 μm particles. Similarly, the focusing of 7.2 μm particles can be observed in Figure 2.16 which is cross sectional view of channel inlet and outlet and the bar plot can be seen in Figure 2.17. Unlike 1.9 μm particles, 7.2 μm particles show much better focusing pattern in comparison with 1.9 μm particles. Line focusing of 7.2 μm particles can be clearly seen

in these figures which indicates a high focusing quality. The different focusing quality of these two different size particles can be explained based on the balance of Dean drag and inertial lift force. The magnitude of Dean drag and inertial lift force is highly dependent on the channel Reynolds number, particle size and hydraulic diameter of the channel. For focusing possibility, the magnitude of these two forces needs to virtually be in the same order. High difference in the magnitude of these forces reduces the feasibility of particle focusing. In the other words, the more difference in the magnitude of Dean drag and inertial lift force, the less possibility and quality of particle focusing.

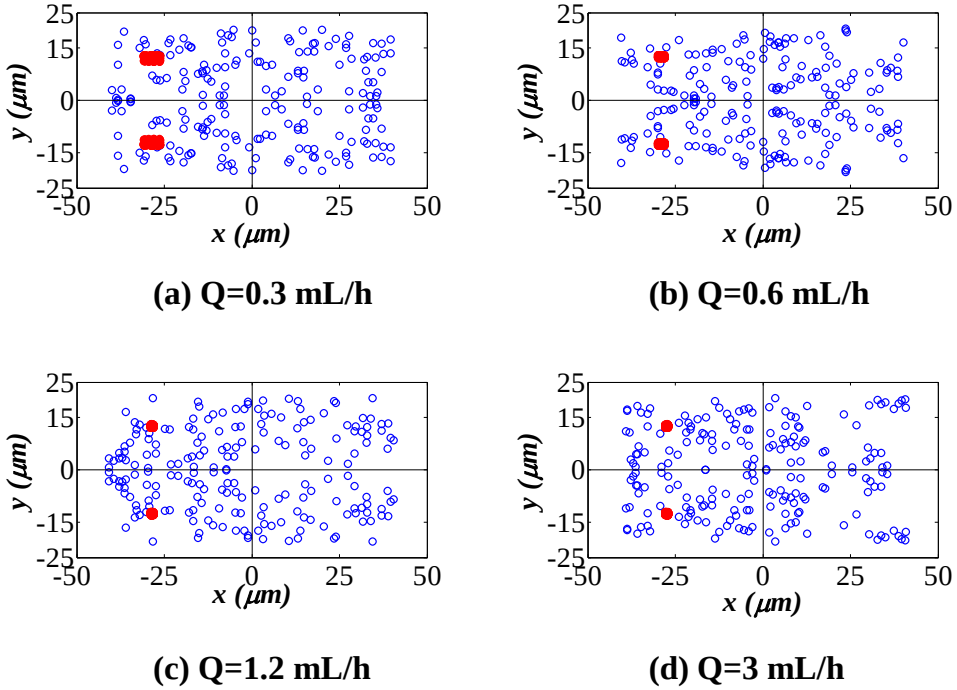

Figure 2.16: Particle distribution at the inlet and the outlet in the height and width directions for different flow rates (Spiral channel with AR 2, 7.2 μm particles)

Due to low inertial lift for small particles, the Dean drag dominates and it causes the particles trap and circulate in Dean vortices. This fact can be clearly seen in the prediction of simulation for 1.9 μm particles. A focusing region which occupies more than half of channel and closer to outer wall. One can expect that by increasing the flow rate which increases the channel Reynolds number, the focusing quality can be improved. This expectation is not satisfied in the

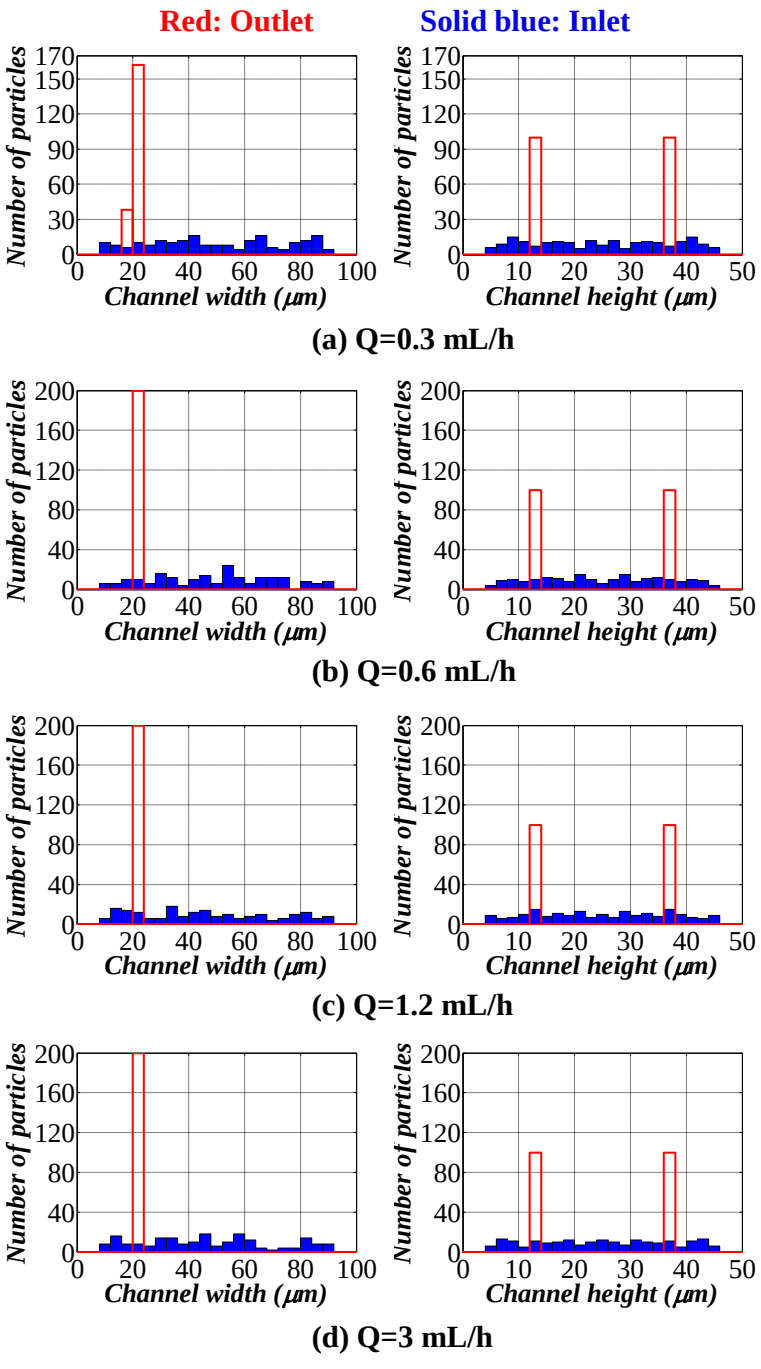

Figure 2.17: Particle distribution at the inlet and the outlet in the height and width directions for different flow rates (Spiral channel with AR 2, 7.2 μm particles)

simulation results. By increasing the channel Reynolds number, both inertial lift force and Dean drag are affected and results in rising of magnitude of both forces simultaneously. Simultaneous increase in the magnitude of both inertial lift force and secondary drag still keeps the ratio of inertial lift and secondary drag much far from unity. The focusing pattern is different in 7.2 μm particles. In this case, inertial lift force and Dean drag are virtually in the same order and this causes the particles to focus almost on a line. As it can be observed in Figures 2.16 and 2.17, the focusing is achieved even for low channel flow rates. Furthermore, by increasing the channel flow rate, the focusing quality is improved due to the better balance of inertial lift and Dean drag.

Another interesting observation that can be made from these simulation results is the focusing pattern of particles in the height of the channel. It can be obviously understood from the cross sectional view of the channel for 1.9 μm particles, focusing pattern has a better efficiency and quality in the height of the channel. It should be pointed out that in the height of the channel the velocity profile has a higher gradient in comparison with the width of the channel. Moreover, due to this fact that shear gradient lift force and wall induced lift are two dominant inertial lift forces in the height direction, higher velocity shear gradient results in higher magnitude of the mentioned forces. This issue yields a better balance of inertial lift with Dean drag in the height direction of the channel and consequently results in a better focusing quality of particles. Moreover, By increasing the channel Reynolds number, a better focusing quality has been obtained. High channel Reynolds number results in high velocity shear gradient magnitude in the height direction and it causes particles focus in height of the channel faster.

2.3.5 Spiral Channel with AR 9

In this section the particle focusing simulation has been performed for a channel with high aspect ratio. The channel is a spiral channel with 5 turns. The starting radius of the spiral is 3000 μm. The channel has a width of 600 μm and height of 70 μm. The spacing between two adjacent turns is 400 μm. Three different

particle sizes with different flow rates are considered for the simulation. particle with size of 2 μm with flow rates of 20 mL/h, 40 mL/h, 80 mL/h and 120 mL/h. particle of size 10 μm with flow rates of 30 mL/h, 40 mL/h, 60 mL/h, 80 mL/h, 100 mL/h and 120 mL/h. Particle of size 20 μm with flow rates of 60 mL/h, 80 mL/h and 100 mL/h. Flow rates of 30 mL/h, 40 mL/h, 60 mL/h, 80 mL/h, 100 mL/h and 120 mL/h correspond to channel Reynolds number of 37, 49, 74, 99, 124, 149 respectively. 100 particles are released from the inlet of the channel with a random distribution. The channel outlet is placed at the end of fifth turn of the spiral. Once the particles are reached to the channel outlet, they will be freezed in their position.

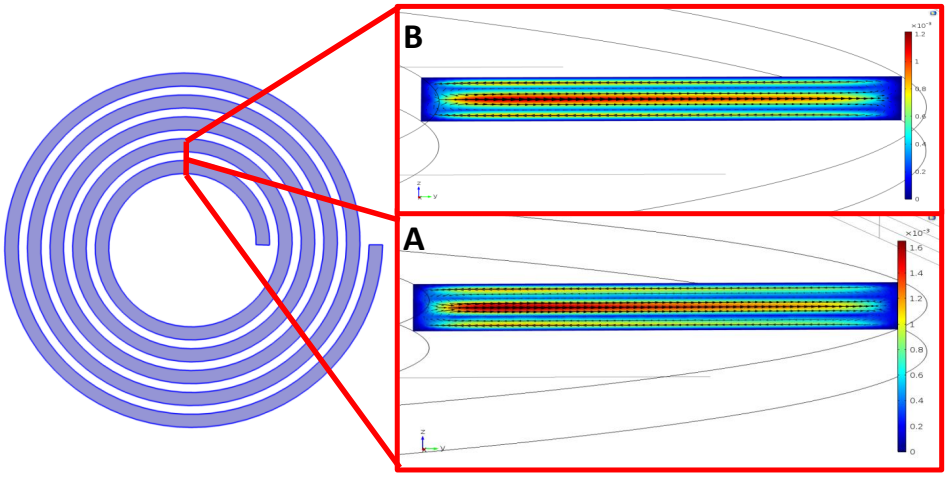

Figure 2.18: Dean flow visualization from COMSOL solution with flow rate of 40 mL/h

Figures 2.19 and 2.20 depict the cross sectional view of channel inlet and outlet and bar plot of spatial distribution of particles both for inlet and outlet respectively. According to these results, 10 μm particles are focused on the long axis of the channel in the vicinity of the inner wall. The reason that why 10 μm particles are focused on the long axis of the channel can be easily found by looking at the particle equilibrium position in a straight channel with the same aspect ratio. As it was observed formerly for a straight channel with aspect ratio of 2, 10 μm particles were focused on the long axis of the channel and symmetrically placed in the vicinity of two vertical walls. Thus, in the spiral channel the particles should focus on the long axis. The existence of secondary

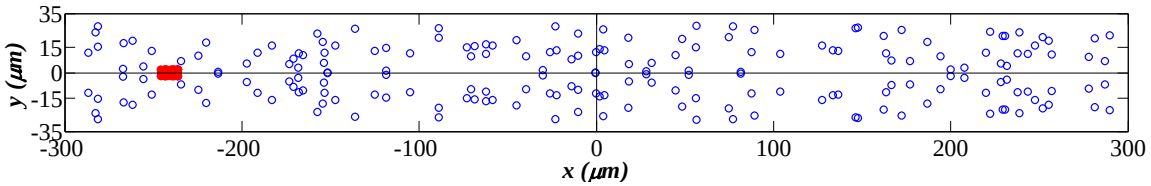

(a) Q=30 mL/h

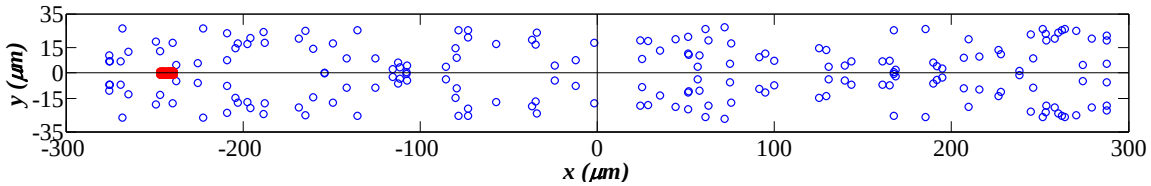

(b) Q=40 mL/h

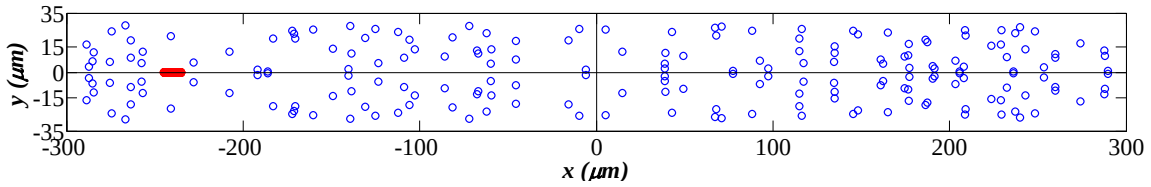

(c) Q=60 mL/h

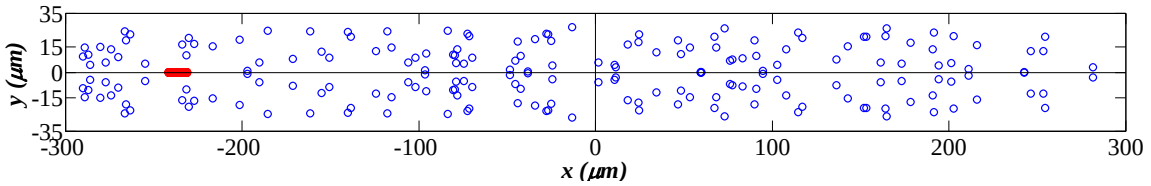

(d) Q=80 mL/h

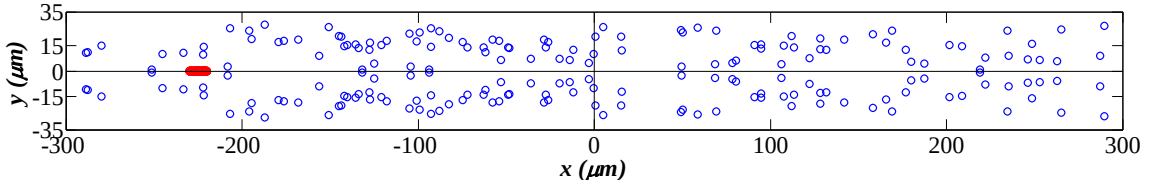

(e) Q=100 mL/h

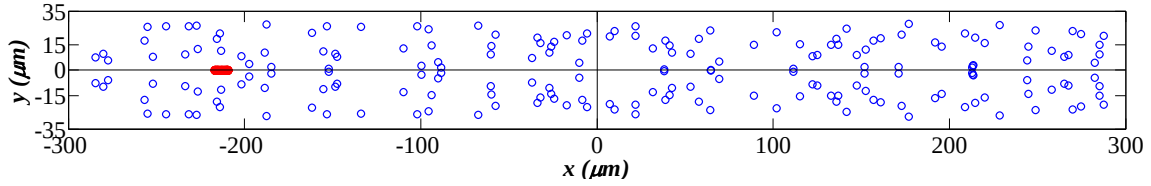

(e) Q=120 mL/h

Figure 2.19: Particle distribution at the inlet and the outlet in the height and width directions for different flow rates (Spiral channel with AR 9, 10 μm particles)

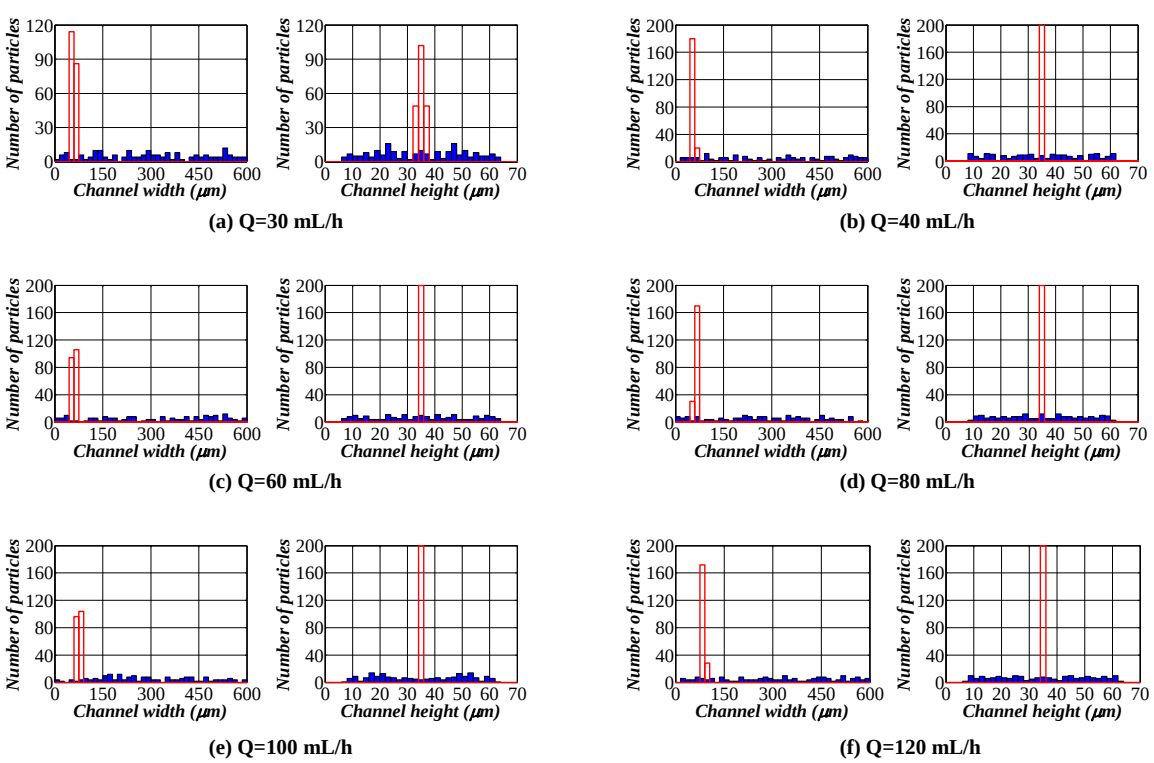

Figure 2.20: Particle distribution at the inlet and the outlet in the height and width directions for different flow rates (Spiral channel with AR 9, 10 μm particles)

flow just relocates the particles in places with better force balances. One may ask that why the particles are focusing in the vicinity of inner walls, while, in the simulation of straight channel there is another equilibrium point in the vicinity of outer wall.The answer can be explained based on the direction of secondary flow and also the inertial lift force.

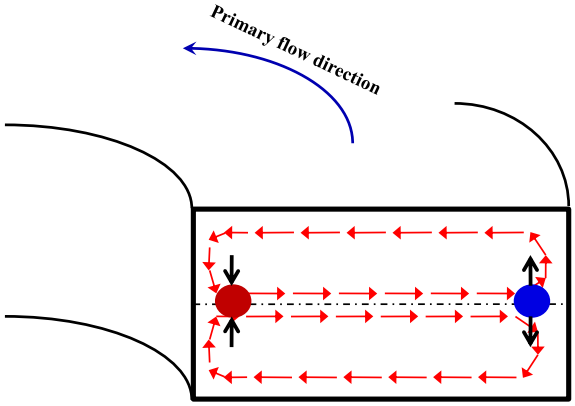

Figure 2.21: Dean flow vortices at the cross section of spiral channel

Figure 2.21 shows the secondary or Dean flow vortices at the cross section of the channel. Two solid circles in this figure indicates two possible position for the particle equilibrium. The blue circle indicates the equilibrium position in the vicinity of outer wall and the red circle indicates the equilibrium position near the inner wall. The red arrays in the figure shows the secondary flow vortices which is from inner wall to outer wall on the long axis of the channel. The black arrays indicate the secondary flow drag acting on the particle in height direction of channel. As it can be clearly observed in this figure, the blue circle position is an unstable equilibrium position since any small deviation from this position will make particle never return to its initial position due to the direction of secondary flow drag in the height direction. On the contrary, the red circle position is a stable equilibrium position since the direction of Dean drag in height direction is inward and causes the particle return to its initial position after any deviation. More interesting, particles in the unstable position (blue circle) with any deflection from this position will be trapped in the Dean vortices and will migrate to the stable equilibrium position (red circle)

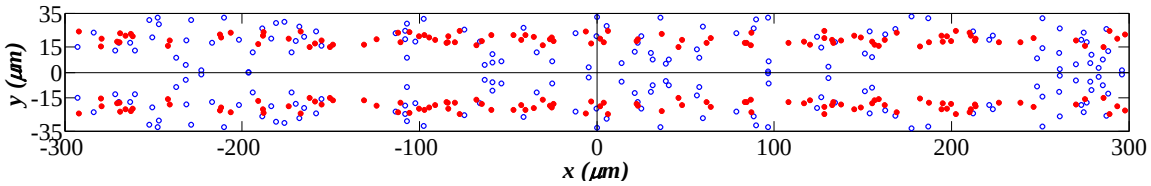

(a) Q=20 mL/h

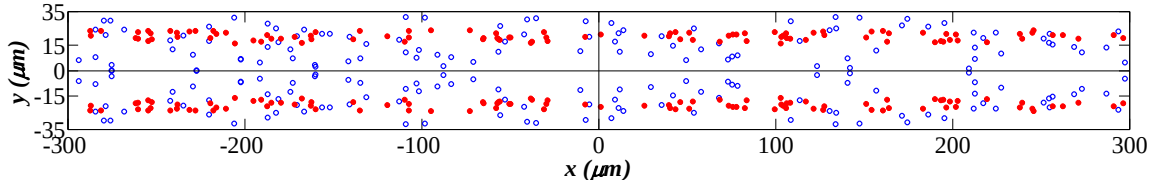

(b) Q=40 mL/h

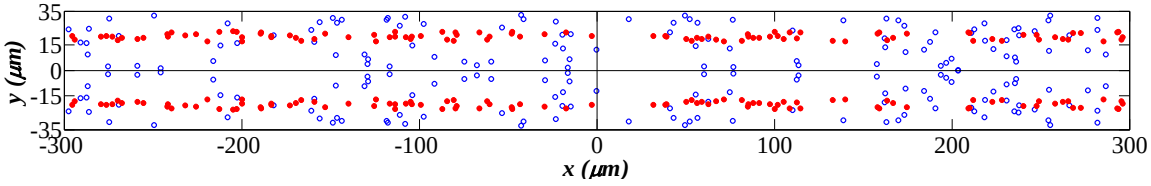

(c) Q=80 mL/h

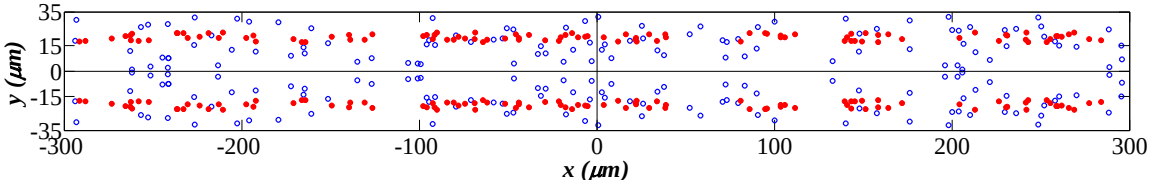

(d) Q=120 mL/h

Figure 2.22: Particle distribution at the inlet and the outlet in the height and width directions for different flow rates (Spiral channel with AR 9, 2 μm particles)

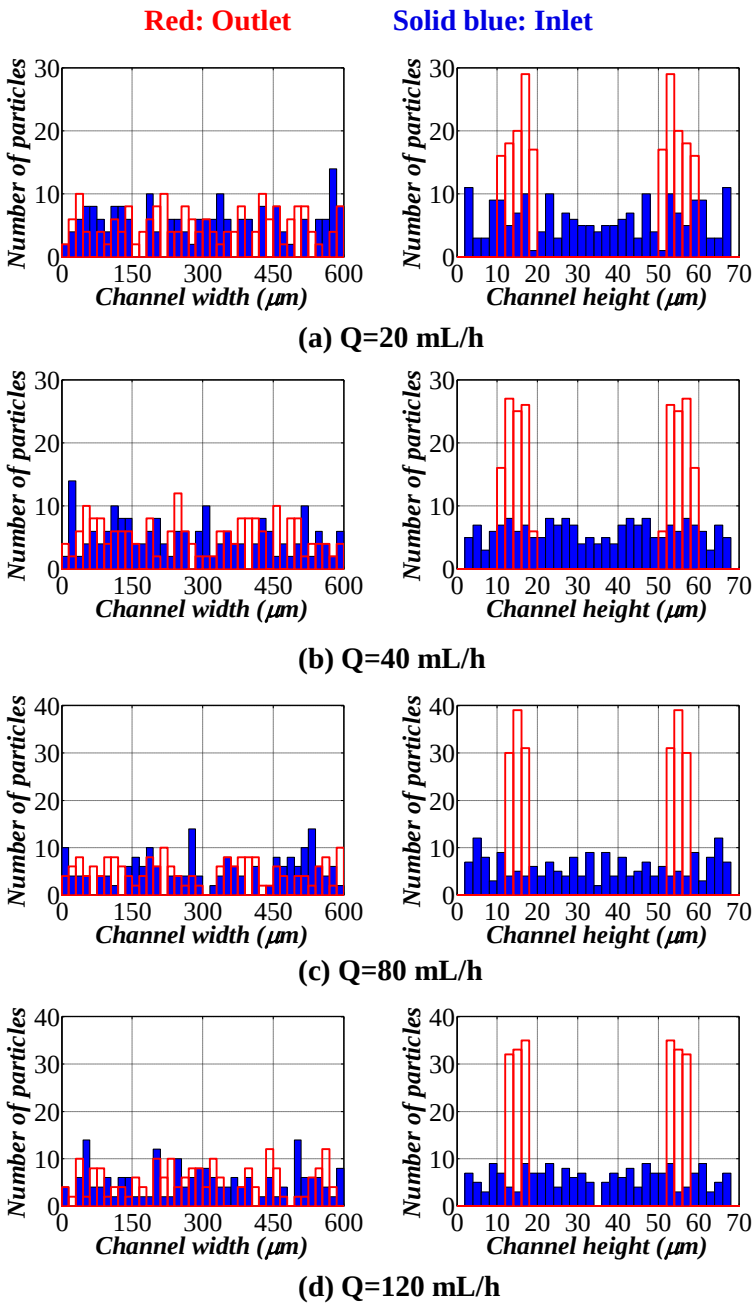

Figure 2.23: Particle distribution at the inlet and the outlet in the height and width directions for different flow rates (Spiral channel with AR 9, 2 μm particles)

Figure 2.22 depicts the cross sectional view of the channel for the 2 μm particles. The bar plot of the particle intensity can be also found in Figure 2.23. As it can be observed from these figures, focusing of 2 μm particles has not been achieved in this channel design. The reason of particle focusing failure for 2 μm particle can be justified through the balance of inertial lift and secondary flow drag. As it was discussed formerly, for small particles, inertial lift force drops substantially and this issue violates the balance of inertial lift and Dean drag. In this case, the particles locate in positions where the balance of mentioned forces is more provided. In this channel design, due to the high channel hydraulic diameter and small particle size, the balance of inertial lift and Dean drag can be occurred in any region of the channel. Therefore, the particles trap in the Dean vortices and circulate in the cross section. Moreover, in the height of the channel due to much higher velocity shear gradient and since the dominant inertial forces in the height direction are shear gradient induced and wall induced lift forces and they are strongly dependent on the velocity shear gradient, particles focus in their equilibrium positions. In the other words, 2 μm particles firstly focus in the height of the channel due to the high velocity shear gradient. Second, they start focusing in the width, however, due to the weaker inertial lift than Dean drag, they trap in the Dean vortices and circulates at their equilibrium position in the height of the channel. The focusing of 20 μm particles is also included and depicted in the Figures 2.24 and 2.25. The same discussion presented for 10 μm particles is also valid for these particles focusing.

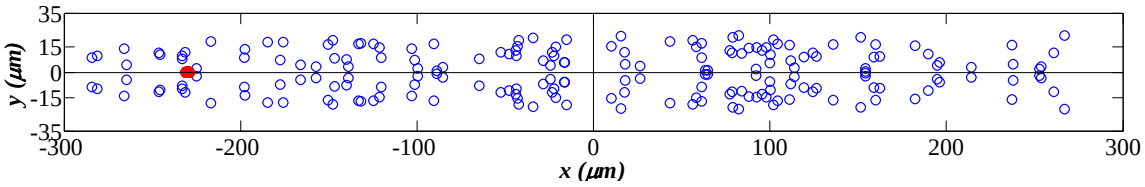

(a) Q=60 mL/h

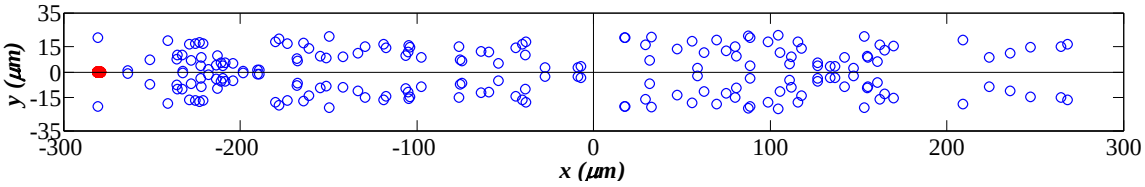

(b) Q=80 mL/h

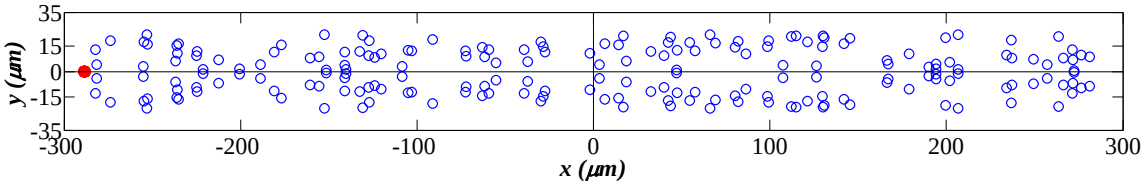

(c) Q=100 mL/h

Figure 2.24: Particle distribution at the inlet and the outlet in the height and width directions for different flow rates (Spiral channel with AR 9, 20 μm particles)

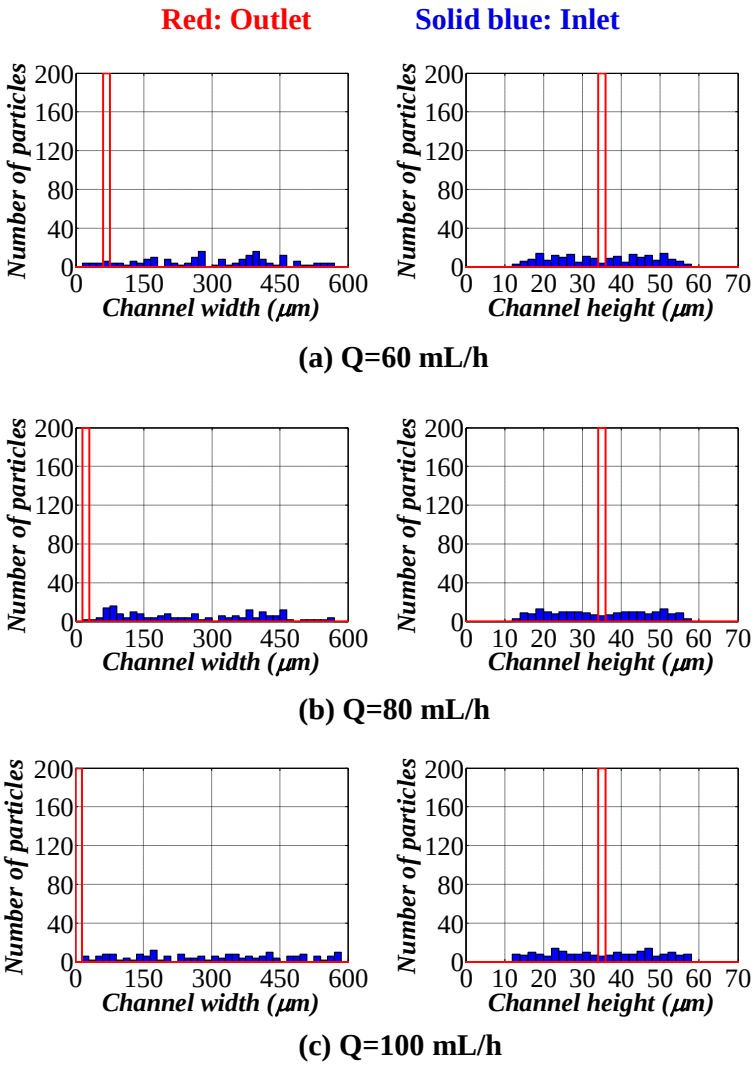

Figure 2.25: Particle distribution at the inlet and the outlet in the height and width directions for different flow rates (Spiral channel with AR 9, 20 μm particles)

2.4 Experimentation

2.4.1 Experimental Setup and Procedure

In order to authenticate the developed computational model used for simulation of particle tracking in the previous section, some experimental investigations are also carried out. Experimental investigations are performed for a spiral channel with desired channel geometry. In this design, a high aspect ratio spiral channel with rectangular cross section of aspect ratio 9 and height of $70\mu m$ was considered. Starting radius of spiral is assigned as 3000 μm to ensure sufficient space for punching as inlet. A spacing distance of 400 μm is assigned for the distance between two adjacent turns. A mold-base method is exploited for usage of PDMS. Due to the channel geometry, a metallic mold using micro-machining CNC machine is manufactured. Spiral micro-channel is fabricated using a mixture of PDMS with 10% curing agent and baked in oven incubator for 80 minutes at the temperature of 80 Celsius. Baked PDMS is carefully peeled from the metallic mold and then bonded on a microscope glass using plasma bonding method. Prior to plasma bonding, the peeled PDMS and microscope glass are carefully washed by IPA and DI water to guarantee purified surfaces free of dust and contaminant. Finally, places for inlet and outlet are punched and Tubing for inlet and outlet are also inserted in the bonded PDMS. To prevent the chip from leakage due to high pressure at the inlet, a layer of PDMS is put on top of the chip and again baked for half an hour. To perform the experiment, a solution of micro-particle and DI water with desired concentration which ensures low number of particle concentration in the sample solution is prepared. Due to the low concentration, the effect of particles on the flow field can be neglected which is a key point for our simulation assumption. The sample solution is pumped into the micro-channel using a syringe pump with desired flow rates. In order to visualize the particle trajectories and final equilibrium positions, Fluorescent latex particles with different sizes together with a custom-made epi-fluorescence microscope are used for small particles of size 10 and 2 μm. Different flow rates are assigned at the inlet of channel to investigate the role of Reynolds number on the focusing mechanism of particle with different sizes. It is worth mentioning that the chip

should be cleaned by pumping DI water into the micro-channel. Particles may sediment in the channel and obstruct the channel entrance.

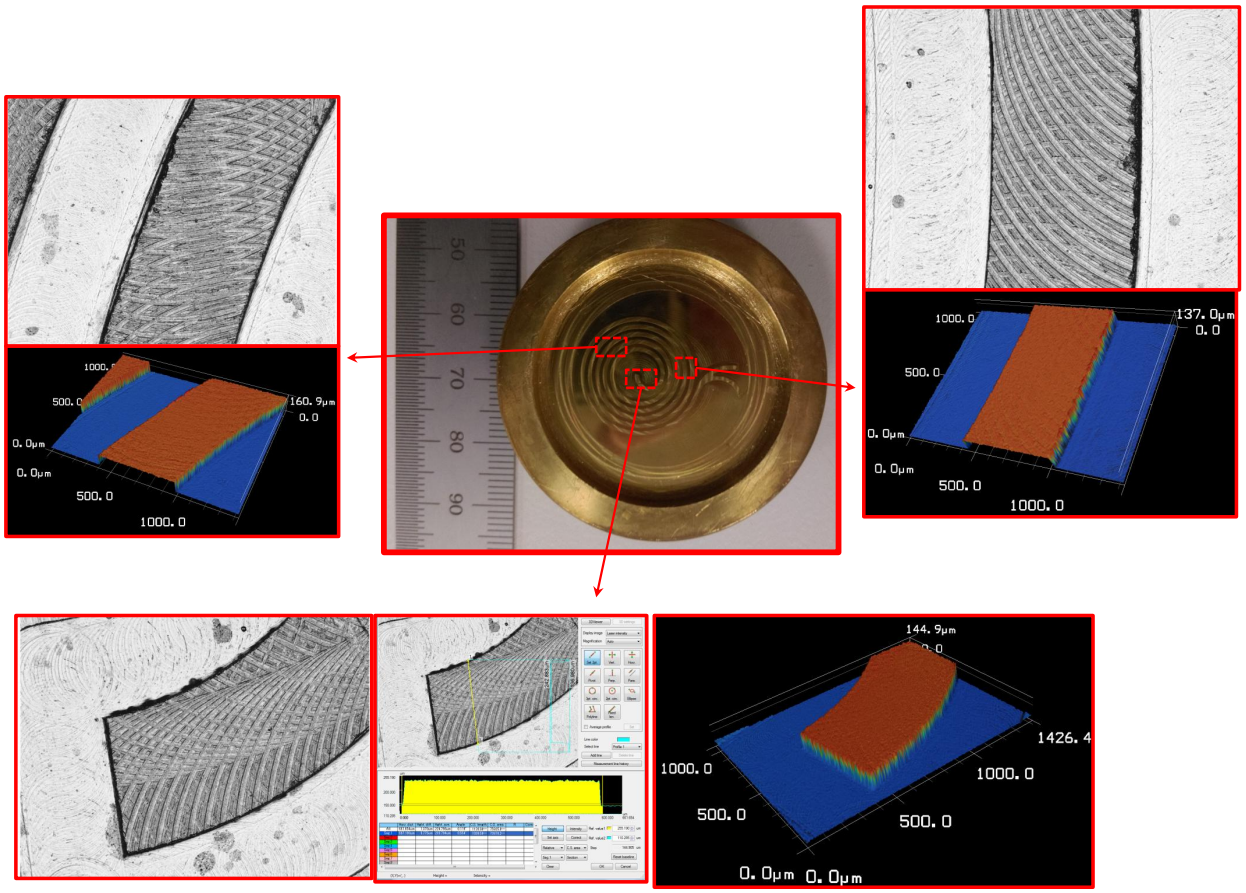

Figure 2.26: Spiral micro-channel metallic mold manufactured using micro-machining CNC machine together with laser microscope images

2.4.2 Experimental Upshots

Figure 2.26 shows the metallic mold for the spiral micro-channel designed for the experiment. The mold is made of brass and the laser microscope images indicate high quality of wall roughness and dimensions accuracy. The mold consists of 5 loops with spacing of 400 μm between two adjacent turns. Three different latex particles with different sizes are considered for the experiment. For 2 and 10 μm sizes, Fluorescent latex particles are used to ease the visualization of particle trajectories. For 20 μm size, normal latex particle is utilized due to the large

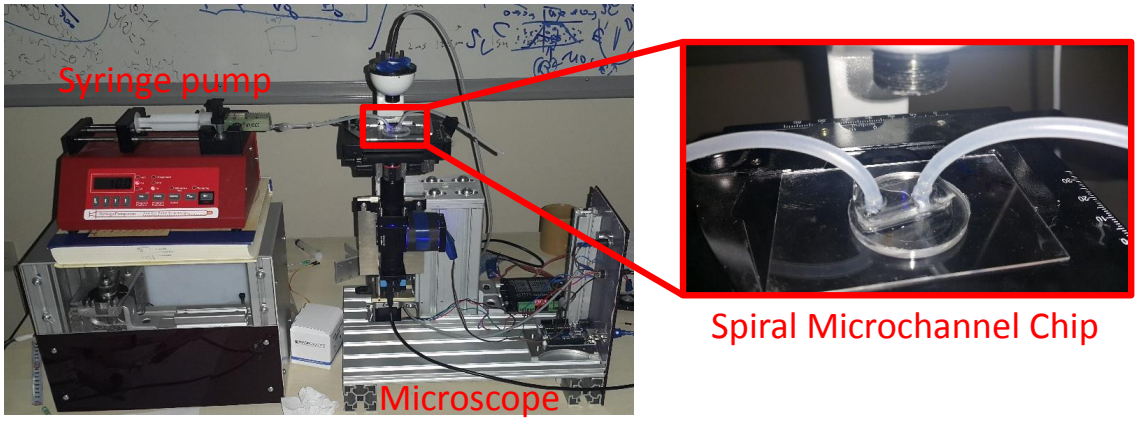

Figure 2.27: Experimental setup

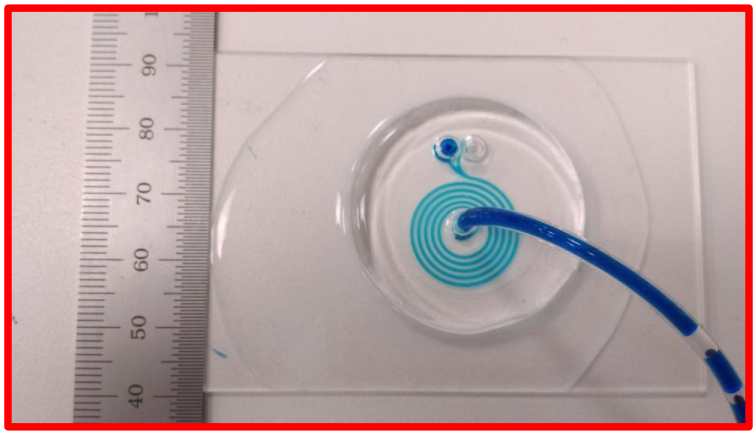

Figure 2.28: Fabricated chip for spiral micro-channel with AR 9

size of the particle and simplicity in visualization. For the 10 μm particle flow rates of 30, 40, 60, 80, 100 and 120 ml/h are considered to observe the focusing mechanism relation with flow rate.

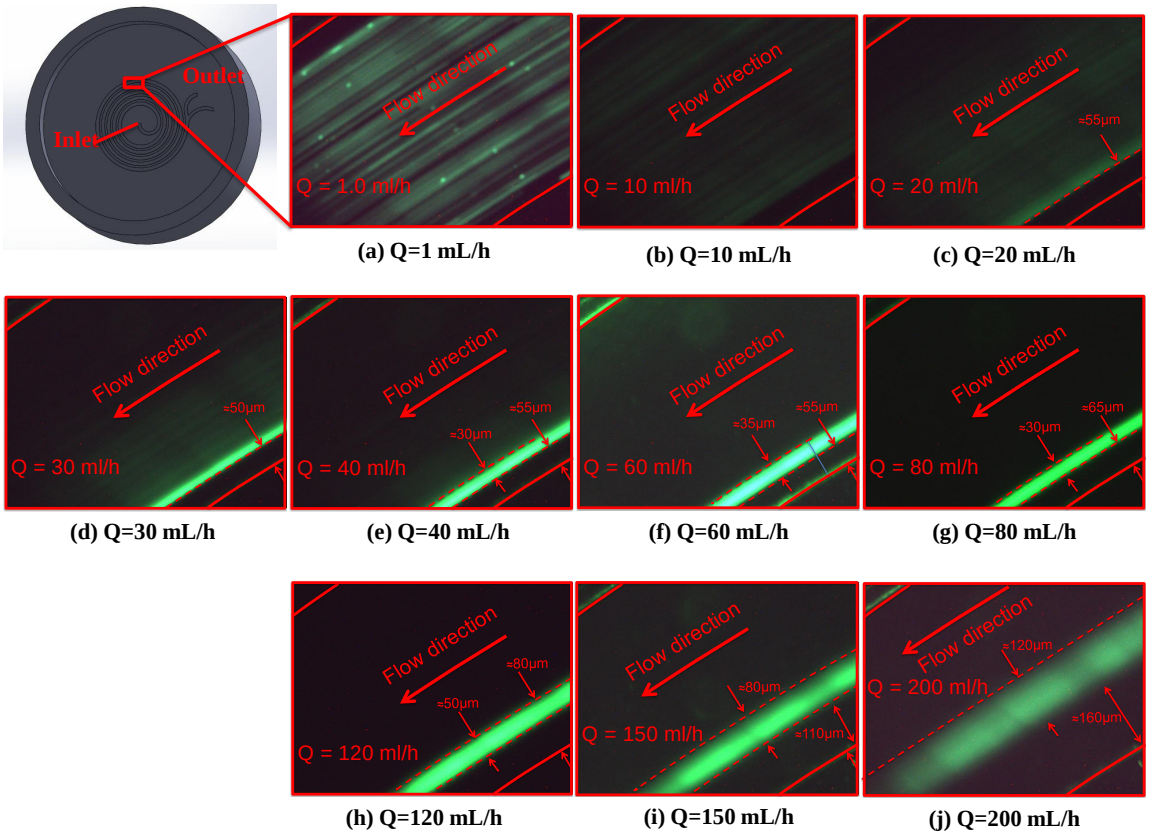

Figure 2.29: Experiment results for 10 μm fluorescence particles in spiral channel of AR 9 with different flow rates

Figure 2.29 shows the experiment results for 10 μm particles focusing in the spiral channel with aspect ratio of 9. The experiment is conducted for different flow rates as indicated in the figure. The experiment is performed for a wide range of flow rates and consequently channel Reynolds number starting with flow rate of 1 mL/h. As it can be observed in this figure, for flow rate of 1 mL/h, the focusing of 10 μm particles is not achieved. This issue is due to this fact that the balance between inertial lift and secondary flow drag has not been obtained yet. By increasing the flow rate to 10 mL/h, the focusing is still not achieved. The accumulation of particles can be partially observed once the channel flow rate reaches to 20 mL/h. For this case, particles start accumulating in the vicinity of

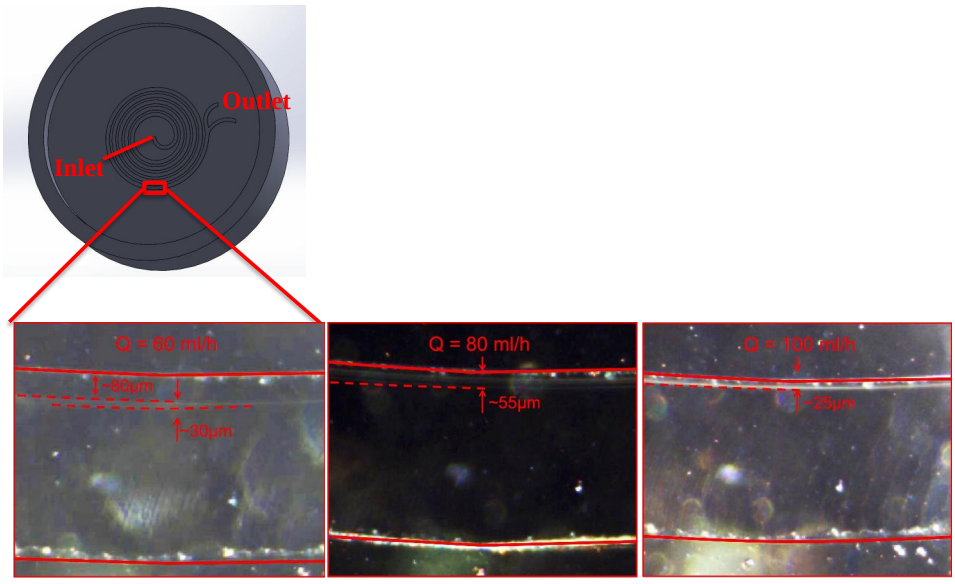

(a) Q=60 mL/h **(b) Q=80 mL/h** **(c) Q=100 mL/h**

Figure 2.30: Experiment results for 20 μm particles in spiral channel of AR 9 with different flow rates

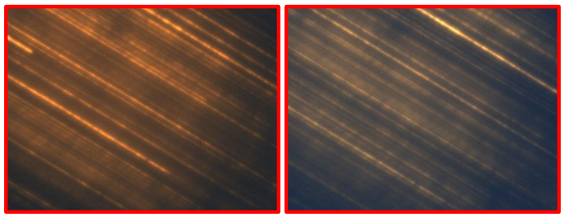

(a) Q=20 mL/h **(b) Q=40 mL/h**

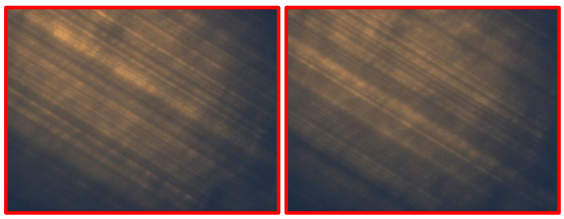

(c) Q=80 mL/h **(d) Q=120 mL/h**

Figure 2.31: Experiment results for 2 μm fluorescence particles in spiral channel of AR 9 with different flow rates

inner wall which the balance of Dean drag and inertial lift is well provided. By increasing the channel flow rate to 30 mL/h, concentration and accumulation of particles can be clearly observed. For the higher flow rates such as 40 mL/h, 60 mL/h and 80 mL/h the focusing of particles is fully achieved. This observation shows that for these specific flow rates, the balance of inertial lift and Dean drag is strongly obtained. The quality of focusing is also very high for these flow rates since the particles focus on the line with the width of approximately three times the particles size. By further rising the channel flow rate, an interesting observation was made. In higher flow rates the width of the focusing line increases and the focusing quality drops. For instance, at the flow rate of 80 mL/h the width of focusing line is three times the particle size. By increasing the flow rate to 150 mL/h and 200 mL/h the width of focusing line becomes 8 and 12 times the particle size. At these flow rate since the channel Reynolds number is high, secondary flow vortices velocity and consequently the Dean drag is high. This issue makes the particles unable to find a narrow line where the force balancing is well provided. In a more clear and conclusive way, particles tend to focus in positions where the balancing of secondary flow Dean drag and inertial lift force is well satisfied. In an optimized channel design and also proper flow rate, the balancing occurs on the a narrow line which is the focusing line of particles. In this case, the best focusing quality can be achieved like what we observed in this experiment for 10 μm particles and flow rates of 40, 60 and 80 mL/h. When these conditions are violated whether the channel design or proper experiment conditions such as flow rate, particles find a wider region to focus where the balancing of forces is somehow provided in that region.

For further understanding the aforementioned explanation, the results of the experiment for 2 μm particle which is depicted in Figure 2.31 are useful. As it can be seen in this figure, the experiment is carried out for 4 different flow rates starting from low to high flow rate. We can clearly see in this figure the failure of focusing of 2μm particles. This is due to this fact that the channel design is not proper for focusing of 2 μm particles. For small particles,the inertial lift force magnitude drops significantly and it causes particles be unable to find a region where the balancing of inertial lift and Dean drag is satisfied. This observation

transparently shows the key effect of Dean drag and inertial lift balancing on the position and also the quality of focusing. The simulation results agreed with this observation as was discussed in the former section. Moreover, the simulation results show that the 2 μm particles fill whole the channel width, however, they fill a specific region in the height of the channel. Unfortunately, we were unable to scan the channel height to authenticate the simulation results about this issue.

2.4.3 Comparison of the Results

The comparison between simulation and experimental results is depicted in Figure 2.32. The comparison is made for the particles of size 10 and 20 μm with three different flow rates. As it can observed in this figure, simulation prediction is in line with the experiment results.

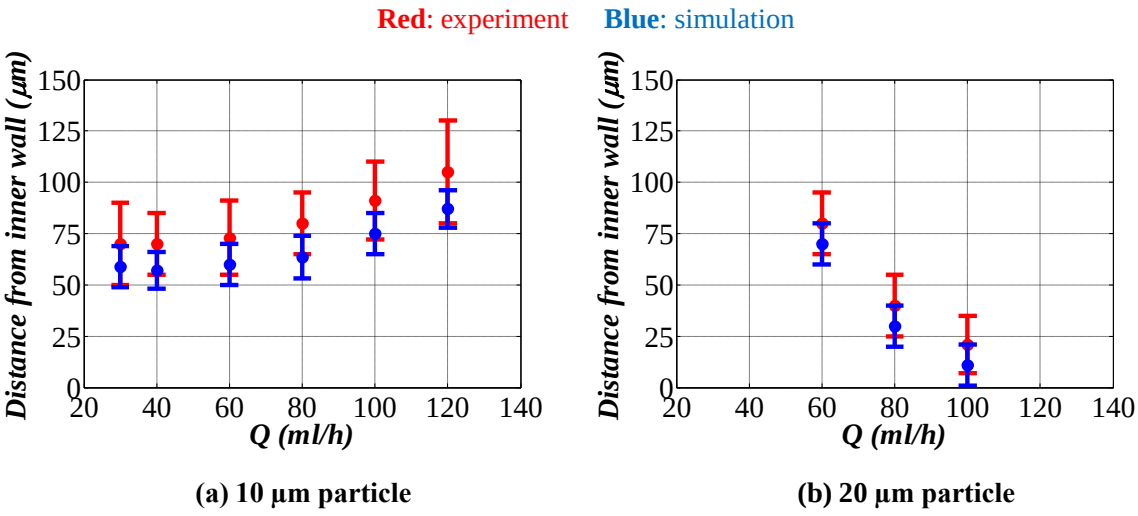

Figure 2.32: Comparison of numerical and experimental results for 10 and 20 μm particles

2.5 Concluding Remarks

Inertial microfluidics has recently attracted increasing attentions of scientists and researchers due to it promising capability in particle manipulation and separation. On the other hand, simplicity, low cost and more importantly high throughput, make inertial microfluidics a unique and powerful tool for biomedical and biological applications. Inertial microfluidics is constructed on two important phenomena: inertial migration and secondary flow. Inertial migration is the migration of randomly dispersed particles at the inlet to several certain positions at the outlet due to existence of inertial lift force. Secondary flow which occurs in curved micro-channels is two symmetric counter rotating vortices in the channel cross-section due to velocity mismatch at the channel centerline and vicinity of wall and centrifugal effects. Secondary or Dean flow plays a substantial important role in size based particle separation.

Numerous studies and researches have been carried out in the literature and different type of particle separation with different type of channel geometry have been reported. However, most of these studies are experimental and based on some order-of-magnitude estimation for the channel design. The better way for channel design is to perform numerical analyses to simulate the channel and find the optimized channel geometry with desired characteristics. Very few studies have been devoted in the literature to develop a numerical and computational model for particle tracking in inertial microfluidics. On the other hand, those studies do not make a clear picture of the numerical model to be implemented for a general case.

In this chapter of the present thesis, the mechanisms of particle focusing in inertial microfluidics were clearly and comprehensively discussed. Furthermore, a general computational model for many particle tracking in inertial microfluidics was developed and validated via different experimental results both from literature and performed by the author. The developed computational model exploits Lagrangian discrete phase model together with temporal integration techniques. LDPM is an easy-to-use model with clear and simple physics and structure. Point-particle assumption is implemented in this model which dictates a particle volume

fraction less than %10. Basically, this model is based on force balance integration for the discrete phase. For this purpose, the flow field needs to be solved without presence of particle and finally particle tracking is performed in a post processing step. Also, our computational model utilizes the inertial lift from a very recent paper for a 3D Poiseuille flow which makes the model even more accurate and realistic. After verifying the computational model, different case studies were performed and the results were compared via experimental observations.

Chapter 3

Modeling of Entry Gas Flow

Progresses in micro-fabrication technology have open up countless opportunities for applications to the theoretical micro scale science by enabling the fabrication of micro-scale devices using photolithographic [1], mechanical machining-based [1, 82] and laser machining methods [83, 84] in recent decades. Through this progress, even the fabrication of structures containing tubes with the diameters of nanometers have become possible [85]. Micro-channels and micro-tubes are inseparable part of microfluidic devices and play a crucial role which necessitates the fundamental knowledge of flow behavior at micro-scale for the effective and optimal design of these devices. Many theoretical investigations have been made on the physics of fluid flow in channels and ducts at micro-scale [45–47].

Considering the pressure-driven flow in micro-channels, on top of the rarefaction effect, the low-Mach-number compressibility effect comes to into picture due to the high viscous resistance leading to a nonlinear streamwise pressure variation [86–88]. That is to say, the fluid needs to be compressible to be able to observe this non-linear streamwise pressure. However, considering short micro-channels and/or micro-channel flow with low inlet/exit pressure ratio, the compressibility effect may be negligible and the flow can be modeled as incompressible. Moreover, the length-over-diameter ratio is typically large for micro-channels which implies the entrance effects are negligible. However, the entrance effects may become quite significant for the channels for short micro-channels.

Entrance region problem for an incompressible flow was well studied for macroscale by many researchers several decades ago [55, 89–91]. Same problem has been recently re-visited for micro-scale [47, 52, 92, 93] for different geometries. Although the hydrodynamic entrance problem is not a true boundary layer problem, boundary layer idealizations which neglect axial diffusion of momentum and radial pressure gradient, are reasonable approximations for laminar flow problems in ducts [55, 89, 93]. In analysis of incompressible entry macro-channel flow, Prandtl's boundary layer approximations have been widely exploited both numerically and analytically. In the mentioned boundary layer approximations, the axial diffusive term in the momentum equation is neglected. Furthermore, pressure variation in transverse direction of channel is considered negligible and the pressure distribution is assumed as a function of axial coordinate only. Utilization of such approximations most often results in a solution independent of Reynolds number and suitable for sufficiently high Reynolds number to neglect the axial diffusive term. Thus, in industrial or scientific applications which deal with highly viscous fluids, the solution obtained based on boundary layer idealizations is not valid due to the moderate Reynolds number and significant effect of axial diffusive term. Moreover, aforementioned idealizations result in a solution which is unable to capture velocity overshoot phenomena. Velocity overshoot or velocity bulges is a phenomena occurs in entrance region and in the vicinity of inlet and causes two symmetric maxima off the centerline in the velocity profile. Velocity overshoot is due to the abrupt change of velocity from uniform at the inlet to the no-slip condition at the solid walls. Observation of velocity overshoot has been reported in the literature using both numerical analyses for slit channel [94], rectangular channel [92], concentric annular channel [95] and experimental investigations [96]. Comparison of obtained solution of Navier-Stokes equation using finite difference method with and without including axial diffusive term for an annular tube [95] clearly shows that the axial diffusion is the key term is prediction of velocity overshoot in analytical and numerical analyses. The velocity overshoot is significant especially for the strictly uniform velocity inlet which is actually an idealization for practical applications. It was observed that the velocity overshoot are much weaker for the irrotational inlet velocity profiles or for the inlet velocity profiles which are approximated to a uniform one. Moreover, the overshoots are only

significant in the vicinity of the entrance, and the zone where this overshoot can be observed is a function of Re number. Therefore, if the measurement data is not taken close to the inlet, the velocity overshoot cannot be detected experimentally [97]. One would expect a weaker velocity overshoot for the flows in microchannel, since the sudden change of the velocity at the inlet due to no-slip boundary condition also reduces due to the slip-velocity at the wall [92].

Three different methods have been used in the literature based on boundary layer approximations in macro-scale and can be classified as: 1) linearization methods, 2)momentum integral method and 3) finite difference method, 4)matching method (based on perturbation analysis). Matching and integral method results in discontinuous solutions for the velocity gradients and the pressure distributions. On the other hand, linearization methods yield a continuous solution albeit the transverse velocity component may not be predicted rigorously. In linearization methods, an expression is proposed for replacement with the convective term which linearizes the axial momentum equation. Usage of such linearizations most often results in a closed form solution for the developing velocity profile. Targ's linearization [98], Langhaar's linearization [55] and Sparrow's linearization [89] are three different important methods that have been mostly implemented in literature for entrance problems. In Targ's method, the convective term is linearized by axial gradient of axial velocity. However,in Langhaar's method the inertia term is replaced with the axial velocity times an unknown function which is a function of axial coordinate. The relation of the unknown function with the axial coordinate is determined by integrating the momentum equation over cross section of channel which leads to an integral type solution. Sparrow's method can be considered as a combination of two former methods. The first and the last methods require the solution of an eigenvalue problem which may have some convergence problems especially close to the inlet. Alternatively, Langhaar's linearization offers an integral type solution with a satisfactory solution at the centerline, in the vicinity of the inlet and far downstream. Langhaar's method has been implemented for different geometries in macro-scale such as circular [55], concentric annular [99], parallel plates and rectangular [98, pp. 69-70].

Many researchers devoted great effort on the experimental investigations and proposed different techniques and different experimental protocols [86, 87, 100, 101], but still measurement of different flow parameters to understand fluid physics is challenging. At this point, analytical and numerical models serve as a basis for the fundamental understanding of the phenomena despite the fact that they require some empirical input in the form of slip-coefficients. In addition, they serve as a fast way to investigate different scenarios. Present study reports an analytical solution of a 2D incompressible, isothermal flow in a developing region of a micro-channel considered both in cylindrical and cartesian coordinates based on Langhaar's linearization. For the rarefaction effect, different second-order models are included in the analysis. Moreover, the general velocity-slip boundary condition proposed by Beskok and Karniadakis [2] for which the general slip-coefficient is evaluated with high accuracy following the reported method for the no-slip case, is implemented. The analytical model is verified by some results available in the literature, and the hydrodynamic entrance length, apparent friction factor and excess pressure drop which are the quantities of interest for many engineering calculations are presented. The proposed solution may be used for the evaluation of thermal characteristics inside micro-channels in the combined entrance region. The unique contribution of the present study is the inclusion of the high-order slip models for the determination of the velocity profile, hydrodynamic entrance length and apparent friction factor at the incompressible and isothermal limit. The analytical nature of the model enables the implementation of Beskok general slip-model with high accuracy, and a fast evaluation of the velocity field without any need for the calculation of eigenvalues. The proposed model can be used for the exploration of heat transfer problems at the incompressible limit (which has been studied extensively in the literature [102–104]) for micro-channels in the combined entrance region without any need for numerical calculation of the flow field.

3.1 Mathematical Modeling

3.1.1 Velocity Profile

Assuming the fluid is incompressible with constant properties, following the Prandtl boundary layer idealizations, the equation of motion in the axial direction (x being the axial direction) together with continuity equation in 2D can be written as:

$$\boldsymbol{\nabla} \cdot \boldsymbol{u} = 0, \tag{3.1}$$

$$\boldsymbol{u} \cdot \boldsymbol{\nabla} u_x = \frac{1}{\rho}\partial_x p + \nu \nabla^2 u_x, \tag{3.2}$$

where $\boldsymbol{u}$ is the velocity field, p is the pressure field, u_x is the velocity component in the axial direction, ρ is the density and ν is the dynamic viscosity. Moreover, following the boundary layer idealization (i) the diffusive term in the axial direction can be neglected compared to the components in the transverse direction, (ii) the transverse velocities velocities within the channel are assumed to be small compared to the axial velocity, and (iii) the pressure gradient in the axial direction is a function of axial coordinate only [55, 105].

3.1.1.1 Micro-tube and Slit Channel

The flow field is first determined for a micro-tube and a slit channel. The schematic of the problem is given in Figure 3.1. With the following dimensionless parameters

$$\lambda = \frac{u_x}{U_m},\ \eta = \frac{u_l}{U_m},\ q = \frac{r}{a},\ \sigma = \frac{x}{Re_{D_h} \cdot D_h},\ \tilde{p} = \frac{p}{1/2\rho U_m^2}, \tag{3.3}$$

where U_m is the mean velocity (which is also the uniform inlet velocity), u_l is the velocity in the transverse direction, a is the scale for the channel height ($a = R$ for a microtube and half of the channel height for parallel plates) and Re_{D_h} is the Re based on hydraulic diameter, Eqs. (3.1) and (3.2) can be non-dimensionalized as:

$$2^{k-2}\frac{\partial \lambda}{\partial \sigma} + \frac{Re_{D_h}}{q^k}\frac{\partial(\eta q^k)}{\partial q} = 0, \tag{3.4}$$

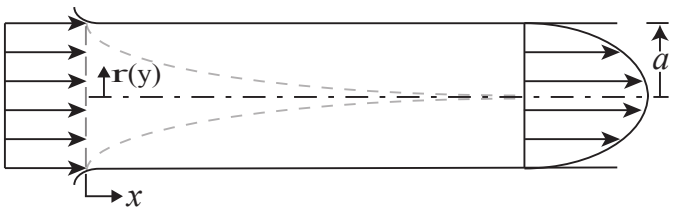

Figure 3.1: Schematics of the microtube and slit channel problem

$$4^{k-2}\lambda\frac{\partial\lambda}{\partial\sigma}+2^{k-2}Re_{D_h}\eta\frac{\partial\lambda}{\partial q}=-2^{2k-5}\frac{\partial\tilde{p}}{\partial\sigma}+\frac{1}{q^k}\frac{\partial}{\partial q}\Big(q^k\frac{\partial\lambda}{\partial q}\Big), \tag{3.5}$$

where $k=0$ corresponds to flow between slit channels (i.e. parallel plates) and $k=1$ corresponds to the flow in a micro-tube.

At this point, following Langhaar's linearization [55,105], the convective terms on the right hand side can be replaced by $(\gamma^2\lambda)$, and the Eq. (3.28) can be written as:

$$\frac{1}{q^k}\frac{\partial}{\partial q}\Big(q^k\frac{\partial\lambda}{\partial q}\Big)-\gamma^2\lambda=2^{2k-5}\frac{\partial\tilde{p}}{\partial\sigma}. \tag{3.6}$$

The solution can be expressed as a combination of modified Bessel's and hyperbolic functions as:

$$\lambda(\gamma,q)=\mathcal{A}(\gamma)\mathcal{G}_1(\gamma q)+\mathcal{B}(\gamma)\mathcal{G}_2(\gamma q)+\mathcal{C}(\gamma) \tag{3.7}$$

where

$$\begin{aligned}\mathcal{G}_1(\gamma q)&=k\ \mathrm{I}_0(\gamma q)+(1-k)\cosh(\gamma q)\\ \mathcal{G}_2(\gamma q)&=k\ \mathrm{I}_1(\gamma q)+(1-k)\sinh(\gamma q)\\ \mathcal{C}(\gamma)&=-\frac{2^{2k-5}}{\gamma^2}\frac{\partial\tilde{p}}{\partial\sigma}\end{aligned} \tag{3.8}$$

Coefficients $\mathcal{A}(\gamma)$, $\mathcal{B}(\gamma)$ and $\mathcal{C}(\gamma)$ can be obtained using the boundary condition at the channel wall,

$$\lambda^{(s)}(\gamma)=-2^{2-k}A_1\mathrm{Kn}\frac{\partial\lambda}{\partial q}\Big|_{q=1}+4^{2-k}A_2\mathrm{Kn}^2\frac{\partial^2\lambda}{\partial q^2}\Big|_{q=1}, \tag{3.9}$$

$$\lambda^{(g)}(\gamma)=-2^{2-k}\frac{\mathrm{Kn}}{1-b\mathrm{Kn}}\frac{\partial\lambda}{\partial q}\Big|_{q=1}, \tag{3.10}$$

the symmetry boundary condition at the centerline, and the continuity equation:

$$\int_0^1 q^k\lambda dq=2^{-k}. \tag{3.11}$$

The subscript (s) stands for the second-order slip in generic form, and (g) stands for the general-slip model. Note that b is a function of (σ) in the entrance region and reaches a value of (-2) at the region far from the entrance (i.e. fully-developed region).

Velocity profile can be obtained as:

$$\lambda(\gamma, q) = \frac{\alpha_1 \gamma^m \mathcal{G}_1(\gamma) + \alpha_2 \mathcal{G}_2(\gamma) - \gamma \alpha_1^m \mathcal{G}_1(\gamma q)}{\alpha_1 \gamma^m \mathcal{G}_1(\gamma) + (\alpha_2 - 2^k \alpha_1^m)\mathcal{G}_2(\gamma)}, \tag{3.12}$$

where

$$\begin{aligned} \alpha_1 &= (1-m)\gamma\ (1 - 4^{2-k} A_2 \gamma^2 \mathrm{Kn}^2) + m(1 - b\mathrm{Kn}), \\ \alpha_2 &= (1-m)\gamma^2\ (2^{2-k} A_1 \mathrm{Kn} + k 4^k A_2 \mathrm{Kn}^2) + 2^{2-k} m \gamma^2 \mathrm{Kn}. \end{aligned} \tag{3.13}$$

$m = 0$ corresponds to second-order slip and $m = 1$ corresponds to general-slip model.

The coefficient b can be derived using definition, Eq. (1.3):

$$b = -2\gamma \frac{\mathcal{G}_1(\gamma)}{\mathcal{G}_2(\gamma)} + 2k \tag{3.14}$$

it should be pointed out that the coefficient b is derived using Taylor's series expansion and is dependent on definition of Kn number and coordinate system. According to our definition of Kn number (ratio of mean free path of gas molecules over hydraulic diameter of channel) and chosen coordinate system, the equation above was re-derived using Taylor's series expansion. Thus, the difference of equation above with original form proposed by Beskok is due to the different definition of Kn number and coordinate system. It also results in different fully developed value of b.

To complete the solution, the relation between the parameters γ and σ needs to be determined. For this purpose, equation of motion, Eq. (3.28) can be integrated over the cross-section as:

$$\begin{aligned} \int_0^1 \Big(4^{k-2}\lambda \frac{\partial \lambda}{\partial \sigma} + 2^{k-2} Re_{D_h} \eta \frac{\partial \lambda}{\partial q}\Big) q^k dq = &- \int_0^1 \Big(2^{2k-5} \frac{\partial \tilde{p}}{\partial \sigma}\Big) q^k dq \\ &+ \int_0^1 \frac{1}{q^k} \frac{\partial}{\partial q}\Big(q^k \frac{\partial \lambda}{\partial q}\Big) q^k dq \end{aligned} \tag{3.15}$$

The first integral can be simplified using continuity equation, Eq. (3.27) as:

$$\int_0^1 \big(4^{k-2}\lambda\frac{\partial\lambda}{\partial\sigma} + 2^{k-2}Re_{D_h}\eta\frac{\partial\lambda}{\partial q}\big)q^k dq = 4^{k-2}\frac{d}{d\sigma}\int_0^1 \lambda^2 q^k dq, \tag{3.16}$$

and the second integral can be simplified by writing equation of motion for the central core of the channel:

$$-\int_0^1 \Big(2^{2k-5}\frac{\partial\tilde{p}}{\partial\sigma}\Big)q^k dq = \frac{2^{2k-5}}{k+1}\frac{d\lambda_0^2}{d\sigma} - \frac{\partial^2\lambda}{\partial q^2}\Big|_{q=0}, \tag{3.17}$$

where the subscript ("o") refers to the values at the centerline. Introducing two new functions F and G:

$$\begin{aligned} F(\gamma) &= 2\int_0^1 \lambda^2 q^k dq - \frac{\lambda_0^2}{k+1}, \\ G(\gamma) &= 2^{5-2k}\Big(\frac{\partial\lambda}{\partial q}\Big|_{q=1} - \frac{\partial^2\lambda}{\partial q^2}\Big|_{q=0}\Big) \end{aligned} \tag{3.18}$$

Eq. (3.37) can be written as:

$$\frac{d\sigma}{d\gamma} = \frac{F\prime(\gamma)}{G(\gamma)}. \tag{3.19}$$

Functions $F(\gamma)$ and $G(\gamma)$ in closed form are derived as:

$$F(\gamma) = \frac{2}{\mathcal{H}^2}\Big[\frac{\mathcal{S}^2}{k+1} - 2\mathcal{S}\alpha_1^m\mathcal{G}_2 + \frac{1}{2}\gamma^2\alpha_1^{2m}\big[\mathcal{G}_1^2 - \mathcal{G}_2^2 + \frac{1-k}{\gamma}\mathcal{G}_1\mathcal{G}_2\big]\Big] - \frac{1}{k+1}\big(\frac{\mathcal{S}-\gamma\alpha_1^m}{\mathcal{H}}\big)^2 \tag{3.20}$$

$$G(\gamma) = 2^{5-2k}\frac{\gamma^2\alpha_1^m(\gamma-\mathcal{G}_2)}{\mathcal{H}} \tag{3.21}$$

where

$$\begin{aligned} \mathcal{S}(\gamma) &= \gamma^m\alpha_1\mathcal{G}_1 + \alpha_2\mathcal{G}_2, \\ \mathcal{H}(\gamma) &= \mathcal{S} - 2^k\alpha_1^m\mathcal{G}_2. \end{aligned} \tag{3.22}$$

Integration of Eq. (3.43), the relation between σ and γ can be defined:

$$\sigma = -\int_\gamma^\infty \frac{F'(\tilde{\gamma})}{G(\tilde{\gamma})}d\tilde{\gamma}. \tag{3.23}$$

Once the γ value is selected, Eqs. (3.12) and (3.44) defines the velocity profile within the micro-channel.

Using Eqs. (3.27) and (3.43), the lateral velocity can be obtained as:

$$\eta = -\frac{1}{4Re_{D_h}}\frac{G(\gamma)}{F'(\gamma)}\frac{\partial}{\partial\gamma}\mathcal{Q}(\gamma,q) \tag{3.24}$$

where the function $\mathcal{Q}(\gamma,q)$ is expressed as:

$$\mathcal{Q}(\gamma,q) = \frac{q\mathcal{S}(\gamma) - 2^k\alpha_1^m\mathcal{G}_2(\gamma q)}{\mathcal{H}(\gamma)} \tag{3.25}$$

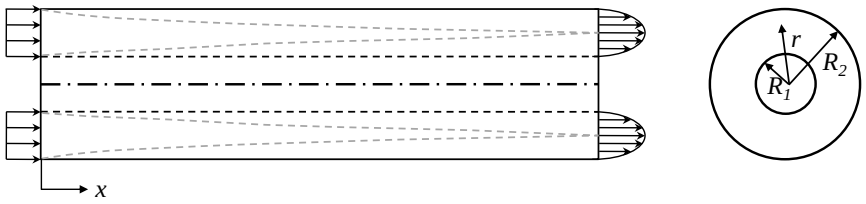

Figure 3.2: Schematics of the concentric annular microtube problem

3.1.1.2 Concentric Annular Micro-channel

As a separate case, the flow field is also determined for he flow in a concentric annular micro-channel. The schematic of the problem is given in Figure 3.2. With the following dimensionless parameters:

$$\lambda = \frac{u_x}{U_m},\ \eta = \frac{u_l}{U_m},\ q = \frac{r}{R_2},\ \sigma = \frac{x}{Re \cdot R_2},\ \tilde{p} = \frac{p}{1/2\rho U_m^2}, \tag{3.26}$$

where U_m is the mean velocity (which is also the uniform inlet velocity), u_l is the velocity in the transverse direction, R_1 is the inner radius, R_2 is the outer radius and Re is the Reynolds number based on outer radius of channel, Eqs. (3.1) and (3.2) can be non-dimensionalized as:

$$\frac{\partial \lambda}{\partial \sigma} + \frac{Re}{q}\frac{\partial (\eta q)}{\partial q} = 0, \tag{3.27}$$

$$\lambda \frac{\partial \lambda}{\partial \sigma} + Re\ \eta \frac{\partial \lambda}{\partial q} = -\frac{1}{2}\frac{\partial \tilde{p}}{\partial \sigma} + \frac{1}{q}\frac{\partial}{\partial q}\Big(q\frac{\partial \lambda}{\partial q}\Big), \tag{3.28}$$

By exploiting Langhaar's linearization method [55, 105], the left hand side term (convective term) can be replaced by $(\gamma^2 \lambda)$, and the Eq. (3.28) can be written as:

$$\frac{1}{q}\frac{\partial}{\partial q}\Big(q\frac{\partial \lambda}{\partial q}\Big) - \gamma^2 \lambda = -\frac{1}{2}\frac{\partial \tilde{p}}{\partial \sigma}. \tag{3.29}$$

The solution is obtained as a combination of modified Bessel's functions of first and second kind as:

$$\lambda(\gamma, q) = \mathcal{A}(\gamma) I_0(\gamma q) + \mathcal{B}(\gamma) K_0(\gamma q) + \mathcal{C}(\gamma) \tag{3.30}$$

Coefficients $\mathcal{A}(\gamma)$, $\mathcal{B}(\gamma)$ and $\mathcal{C}(\gamma)$ can be found using the boundary condition at the channel wall,

$$\begin{aligned} \lambda^f(q=1) &= -2\mathrm{Kn}(\frac{\partial\lambda}{\partial q})_{q=1} \\ \lambda^f(q=m) &= 2\mathrm{Kn}(\frac{\partial\lambda}{\partial q})_{q=m} \end{aligned} \tag{3.31}$$

$$\begin{aligned} \lambda^g(q=1) &= -2\frac{\mathrm{Kn}}{1-b_1\mathrm{Kn}}(\frac{\partial\lambda}{\partial q})_{q=1} \\ \lambda^g(q=m) &= 2\frac{\mathrm{Kn}}{1-b_2\mathrm{Kn}}(\frac{\partial\lambda}{\partial q})_{q=m} \end{aligned} \tag{3.32}$$

and the continuity equation:

$$\int_m^1 q\lambda dq = \frac{1}{2}(1-m^2). \tag{3.33}$$

where m is the radii ratio of the channel ($m = R_1/R_2$). The superscripts (f) and (g) stand for the first-order slip and general-slip model respectively. The parameter b used in the general slip velocity is a function of axial coordinate and reached a constant value at a far distance downstream (Fully-developed region).

Velocity profile is obtained using Eqs. (3.30) – (3.33) both for first-order and general slip velocity. Closed form solution of velocity profile is not stated here due to lack of space and can be found in the Appendix.

The coefficient b can be written both for inner and outer walls using definition, Eq. (1.3):

$$\begin{aligned} b_1 &= 2\left(\frac{u_0''}{u_0'}\right)_{q=m} \\ b_2 &= -2\left(\frac{u_0''}{u_0'}\right)_{q=1} \end{aligned} \tag{3.34}$$

and can be derived in closed form as:

$$\begin{aligned} b_1 &= \frac{2\gamma^2 m\Big(K_0(\gamma)I_0(\gamma m) - I_0(\gamma)K_0(\gamma m)\Big)}{\gamma m\Big(K_0(\gamma)I_1(\gamma m) + I_0(\gamma)K_1(\gamma m)\Big) - 1} - \frac{2}{m} \\ b_2 &= 2\left[\frac{\gamma^2\Big(K_0(\gamma)I_0(\gamma m) - I_0(\gamma)K_0(\gamma m)\Big)}{\gamma I_1(\gamma)K_0(\gamma m) + \gamma K_1(\gamma)I_0(\gamma m) - 1} + 1\right] \end{aligned} \tag{3.35}$$

Furthermore, the constant values of b_1 and b_2 in far distance downstream (Fully-developed region) can be found as:

$$\begin{aligned} b_1^{fd} &= 2\frac{m^2 + 2m^2\log(m) - 1}{\Big(m - m^3 + 2m^3\log(m)\Big)} \\ b_2^{fd} &= 2\frac{m^2 + 2\log(m) - 1}{\Big(-1 + m^2 - 2\log(m)\Big)} \end{aligned} \tag{3.36}$$

It is worth mentioning that the coefficient b_1 and b_2 are derived by using Taylor's series expansion to ensure second-order accuracy of the general slip velocity. The equation above is derived by re-writing the Taylor's series expansion based on our chosen coordinate system and definition of Kn. Thus, the difference between the equation above and its original form proposed by Beskok [2] is due to the difference in the definition of Kn.

In order to complete the solution of velocity profile, the relation between parameters σ and γ should be found. For this purpose, axial momentum equation, Eq. (3.28) should be integrated over the cross-section of channel as:

$$\int_m^1 \Big(\lambda\frac{\partial\lambda}{\partial\sigma} + Re\ \eta\frac{\partial\lambda}{\partial q}\Big)qdq = \int_m^1 \Big(-\frac{1}{2}\frac{\partial\tilde{p}}{\partial\sigma}\Big)qdq + \int_m^1 \frac{1}{q}\frac{\partial}{\partial q}\Big(q\frac{\partial\lambda}{\partial q}\Big)qdq, \tag{3.37}$$

Using continuity equation, Eq. (3.27) and some mathematical manipulation, the left hand side integral can be replaced as:

$$\int_m^1 \Big(\lambda\frac{\partial\lambda}{\partial\sigma} + Re\ \eta\frac{\partial\lambda}{\partial q}\Big)qdq = \frac{d}{d\sigma}\int_m^1 \lambda^2 qdq, \tag{3.38}$$

It is assumed that the central core of the velocity is not affected by viscous effects. Then, for the pressure gradient, axial momentum equation can be written for the central core of channel and the first integral in the right hand side can be simplified as:

$$\int_m^1 \Big(-\frac{1}{2}\frac{\partial\tilde{p}}{\partial\sigma}\Big)qdq = \frac{1}{2}\frac{d}{d\sigma}\int_m^1 \bar{\lambda}^2 qdq - \frac{1}{2}(1-m^2)\lambda_{qq}\big|_{q=\frac{m+1}{2}}, \tag{3.39}$$

where the bar values refer to the values at the mean radius of the pipe. The last integral can also be readily evaluated as:

$$\int_m^1 \frac{1}{q}\frac{\partial}{\partial q}\Big(q\frac{\partial\lambda}{\partial q}\Big)qdq = \lambda_q\big|_{q=1} - m\lambda_q\big|_{q=m}, \tag{3.40}$$

Substituting all these equations in the Eq. (3.37) and re-arranging results in:

$$\frac{d}{d\sigma}\int_m^1 \left(\lambda^2 - \frac{\bar{\lambda}^2}{2}\right) qdq = \lambda_q\big|_{q=1} - m\lambda_q\big|_{q=m} - \frac{1}{2}(1-m^2)\lambda_{qq}\big|_{q=\frac{m+1}{2}} \tag{3.41}$$

Defining new functions $F(\gamma)$ and $G(\gamma)$ such as:

$$\begin{aligned} F(\gamma) &= \int_m^1 \left(\lambda^2 - \frac{\bar{\lambda}^2}{2}\right) qdq, \\ G(\gamma) &= \lambda_q\big|_{q=1} - m\lambda_q\big|_{q=m} - \frac{1}{2}(1-m^2)\lambda_{qq}\big|_{q=\frac{m+1}{2}} \end{aligned} \tag{3.42}$$

Eq. (3.41) can be written as:

$$\frac{d\sigma}{d\gamma} = \frac{F'(\gamma)}{G(\gamma)}. \tag{3.43}$$

Integration of Eq. (3.43), the relation between σ and γ can be defined:

$$\sigma = -\int_\gamma^\infty \frac{F'(\tilde{\gamma})}{G(\tilde{\gamma})} d\tilde{\gamma}. \tag{3.44}$$

By assigning a value to parameter γ, using Eq.(3.43) the value of dimensionless axial coordinate (σ) can be obtained and finally the velocity profile is known using closed form solution available in Appendix.

3.1.2 Pressure Drop and Friction Factor

3.1.2.1 Micro-tube and Slit Channel

To evaluate the pressure drop along the channel, Eq. (3.28) needs to be integrated over the cross-sectional area as:

$$-\frac{2^{2k-5}}{k+1}\frac{\partial \tilde{p}}{\partial \sigma} = 4^{k-2}\frac{d}{d\sigma}\int_0^1 \lambda^2 q^k dq - \frac{\partial \lambda}{\partial q}\Big|_{q=1}, \tag{3.45}$$

and then integrated in the σ-direction:

$$\Delta\tilde{p} = 2(k+1)\int_0^1 q^k\lambda^2 dq - 2 + 2^{5-2k}(k+1)\int_\gamma^\infty \frac{\partial \lambda}{\partial q}\Big|_{q=1}\frac{F'(\tilde{\gamma})}{G(\tilde{\gamma})} d\tilde{\gamma} \tag{3.46}$$

One important parameter for the engineering calculations is the Fanning friction factor and the apparent friction factor. The fanning friction factor can be defined as:

$$f \cdot Re_{D_h} = -2^{3-k}\Big(\frac{\partial \lambda}{\partial q}\Big)_{q=1}, \tag{3.47}$$

using the derived velocity profiles, the Fanning friction factor can be written as:

$$f \cdot Re_{D_h} = \frac{-\gamma^2 \alpha_1^m \mathcal{G}_2(\gamma)}{\mathcal{H}(\gamma)} \tag{3.48}$$

The apparent friction factor which considers frictional loss together with the effect of acceleration in the developing region can be derived as:

$$f_{app} \cdot Re_{D_h} = \frac{\Delta\tilde{p}}{4\sigma} \tag{3.49}$$

where $\Delta\tilde{p}$ is given in Eq. (3.51).

3.1.2.2 Concentric Annular Micro-channel

Similarly, to find the pressure drop along the channel, again, Eq. (3.28) should be integrated over the cross-sectional area of channel as:

$$-\frac{1}{4}\frac{\partial\tilde{p}}{\partial\sigma}(1-m^2) = \frac{d}{d\sigma}\int_m^1 \lambda^2 q dq + m\lambda_q|_{q=m} - \lambda_q|_{q=1}, \tag{3.50}$$

Integrating along the axial direction of channel results in:

$$\Delta\tilde{p} = \frac{4}{1-m^2}\int_m^1 q\lambda^2 dq - 2 - \frac{4}{1-m^2}\int_\gamma^\infty (m\lambda_q|_{q=m} - \lambda_q|_{q=1})\frac{F'(\tilde{\gamma})}{G(\tilde{\gamma})}d\tilde{\gamma} \tag{3.51}$$

The fanning friction factor can be defined as:

$$\begin{aligned} f^{(1)} \cdot Re &= -\frac{2}{1-m}\Big(\frac{\partial\lambda}{\partial q}\Big)_{q=m} \\ f^{(2)} \cdot Re &= -\frac{2}{1-m}\Big(\frac{\partial\lambda}{\partial q}\Big)_{q=1} \end{aligned} \tag{3.52}$$

Furthermore, the apparent friction factor which combines the entrance effects together with frictional loss can be calculated as:

$$f_{app} \cdot Re_{D_h} = \frac{\Delta\tilde{p}}{4\sigma} \tag{3.53}$$

where $\Delta\tilde{p}$ is given in Eq. (3.51).

3.2 Results and Discussion

The mathematical modeling discussed in Section 2 is coded by the help of the *Mathematica*® software. One critical point in the evaluation is the improper integrals given in Equations (3.44) and (3.51). The evaluation of these integrals may be problematic as ($\sigma \to \infty$). Although these integrals necessarily need be integrated to infinity, it is known that the flow is fully developed after a certain σ value. In this case, a value was assigned to the σ beyond the fully developed value and pressure drop was evaluated as:

$$\Delta\tilde{p}(\sigma > \sigma_e) = \Delta\tilde{p}(\sigma_e) + \frac{4}{1-m^2}(m\lambda_q^{fd}|_{q=m} - \lambda_q^{fd}|_{q=1})(\sigma - \sigma_e) \tag{3.54}$$

for concentric annular microchannel and:

$$\Delta\tilde{p}(\sigma > \sigma_e) = \Delta\tilde{p}(\sigma_e) + 2^{5-2k}(k+1)\frac{\partial\lambda}{\partial q}\Big|_{q=1}(\sigma - \sigma_e) \tag{3.55}$$

for slit and circular microchannel. Superscript "fd" refers to fully-developed velocity profile and σ_e refers to the distance downstream in which the velocity becomes fully-developed. Once the flow flow is fully-developed, the integrals can be evaluated without any problem since the fully-developed velocity profile is known. The whole calculations takes about a minute on a laptop computer.

3.2.1 Verification of the Model

3.2.1.1 Micro-tube and Slit Channel

Centerline velocity which is an important parameter in determination of entrance length and boundary layers growth is calculated and compared with available data in literature for continuum gas flow in Figure 3.3 to verify the accuracy of the present model. For comparison, full solution of Navier-Stokes equation together with continuity using finite element method based simulation environment *COMSOL Multiphysics*®, an analytical method based on eigenvalue expansion [93] and numerical result based on finite difference method from the literature [98] are included in Figure 3.3. Although not presented, COMSOL model and Liu's results

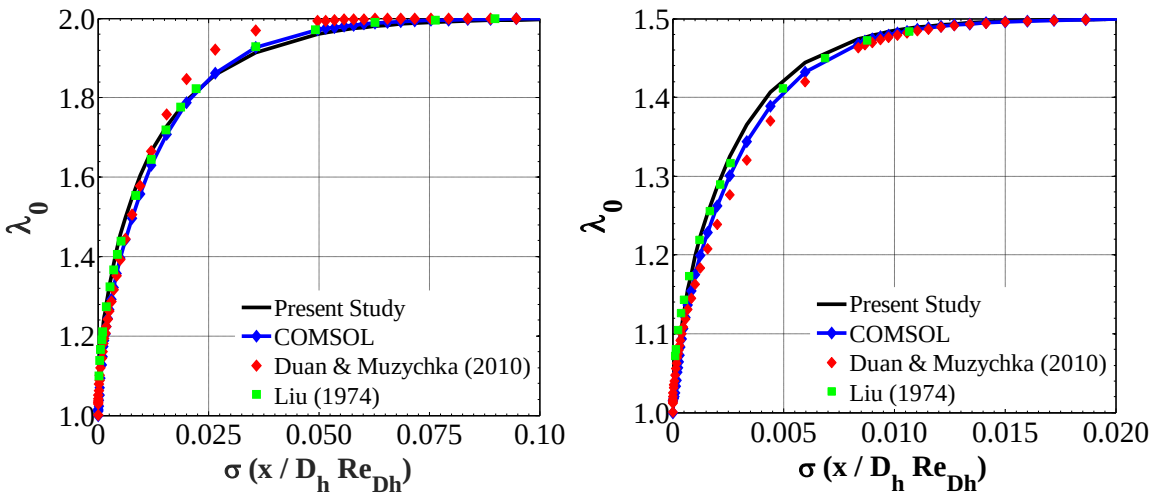

(a) Micro-tube **(b)** Slit channel

Figure 3.3: Development of centerline velocity for continuum gas flow

can predict the velocity overshoot. However, a linearization is used in the solution of [93]. As seen from the graph, all solutions merge the same centerline velocity in the fully-developed limit. COMSOL and Liu's results are very close to each other, and the present study and the results by [93] are on two opposite side of the numerical curves. The discrepancy is in the entrance region. All the results are within $\pm 3\%$ uncertainty, which means the results are in good agreement, regardless of the linearization.

A recent experimental data obtained by laser doppler velocimetry [97] is also compared against the result of present study for a macro-scale tube at different axial locations. The experimental data is taken at both the locations above and below the centerline. As seen from the figure, the results are in good agreement. Following these verifications, it is evident that Langhaar's linearization can be implemented for the modeling of velocity field within the entrance region with a reasonable accuracy.

3.2.1.2 Concentric Annular Micro-channel

Velocity profile development is illustrated in Figure 3.5 for two different radii ratios $m = 0.1$ and $m = 0.8$ for macro-scale (continuum regime) at different

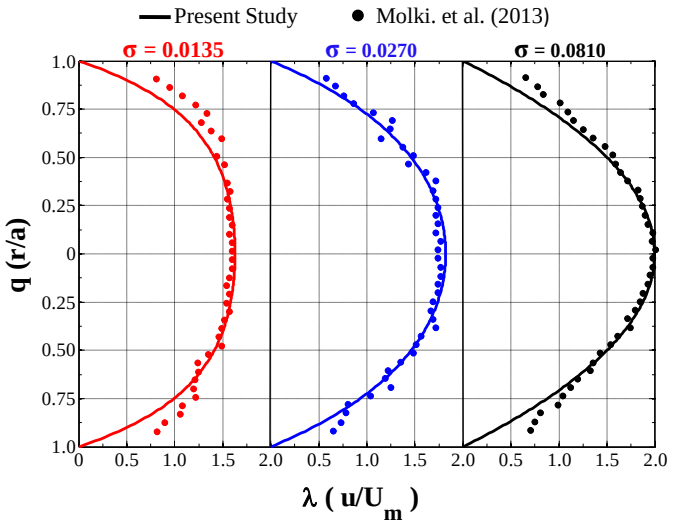

Figure 3.4: Velocity profile in the entrance region of a macro-tube

cross sections of channel. The velocity is also compared with the results using COMSOL Multiphysics software and good agreement is achieved. As it can be readily observed, our model is unable to capture the velocity overshoot in the vicinity of inlet as expected. However, COMSOL results show the velocity bulges at cross sections sufficiently close to inlet. As explained formerly, neglecting axial diffusive term in momentum equation results in inability of observing the velocity overshoot. Moreover, velocity overshoot can only be observed at cross sections sufficiently close to inlet. On the other hand, the velocity overshoot region decreases by increasing the Reynolds number [94] and since our model is valid for high Reynolds numbers, practically the effect of velocity overshoot becomes negligible. According to the aforementioned figure, by comparing velocity profiles at the same cross section for radii ratios of 0.1 and 0.8, a faster velocity development can be seen for the higher radii ratio. In the other words, annular pipes with higher radii ratio experience faster velocity development and consequently less entrance effects. Symmetry of velocity profile is also another interesting issue can be observed in Figure 3.5. For $m = 0.1$, the velocity is not distributed symmetrically around the central core. This issue can be seen more clearly in the fully-developed velocity profile ($\sigma = 5 \times 10^{-2}$). However, for the case of $m = 0.8$, the velocity is fully symmetric and also follows a parabolic distribution with virtually the same pattern as it can be seen in fully-developed flow for slit

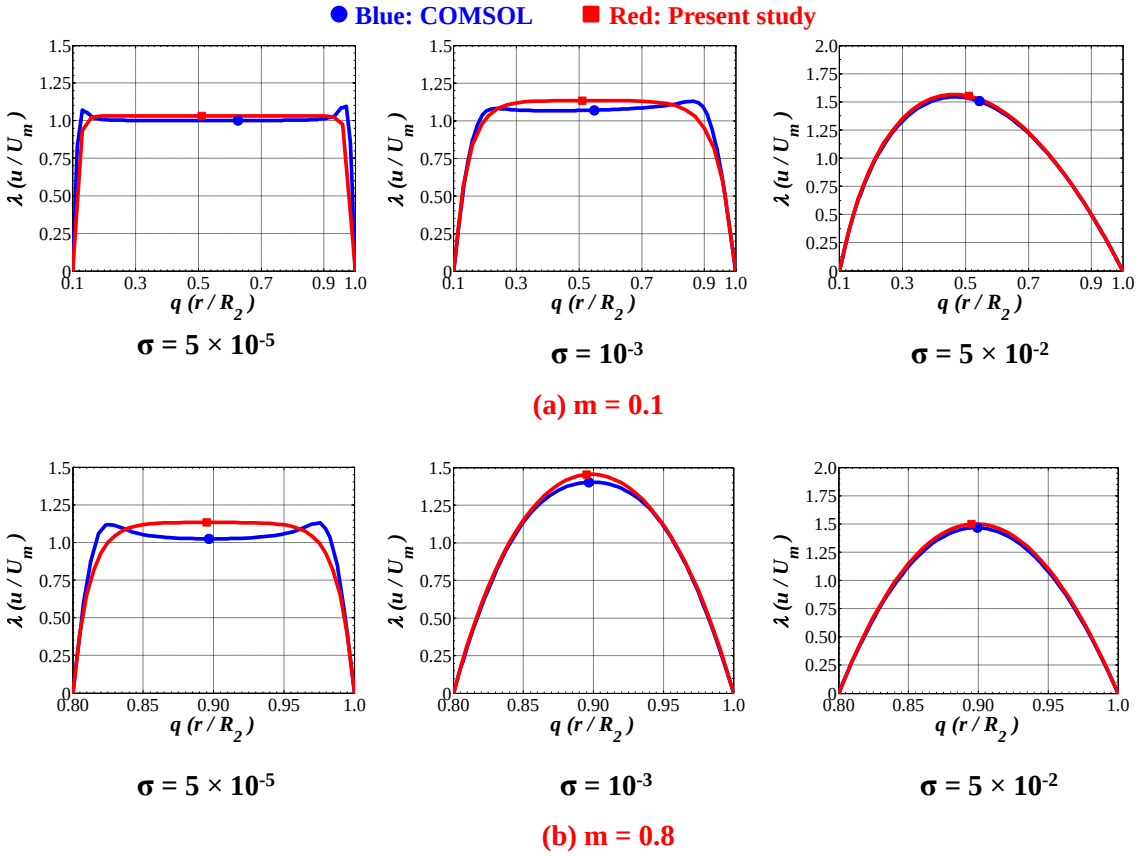

Figure 3.5: Velocity profile in the entrance region of a macro-channel for different radii ratios

channel.

3.2.2 Velocity Profile and Entrance Length

The velocity profiles within the entrance region for a micro-tube and slit channel is shown in Figure 3.6 for different slip models. At $\sigma = 0$ which corresponds to the inlet, a uniform velocity profile is obtained which is an inherent assumption of the boundary layer idealizations. As σ increases, boundary layers start growing. At a certain distance downstream they will be merged together and fully-developed velocity profile which is a smooth unchanged parabola is achieved. In the slip-flow regime, this parabola is more flat than the that of a continuum gas flow due to the reduction of shear stresses on the solid walls with increased Kn. Although

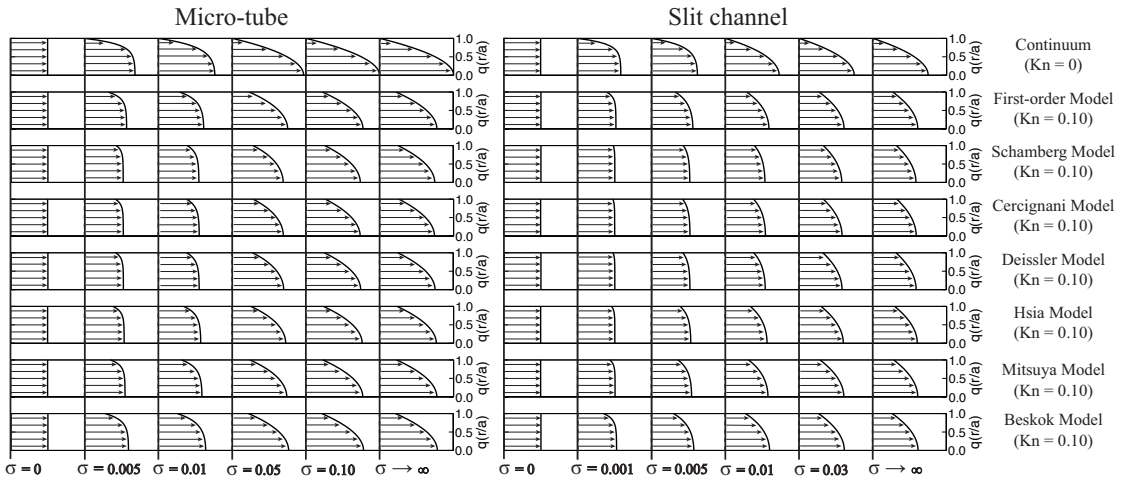

Figure 3.6: Developing velocity profile within the micro-channel

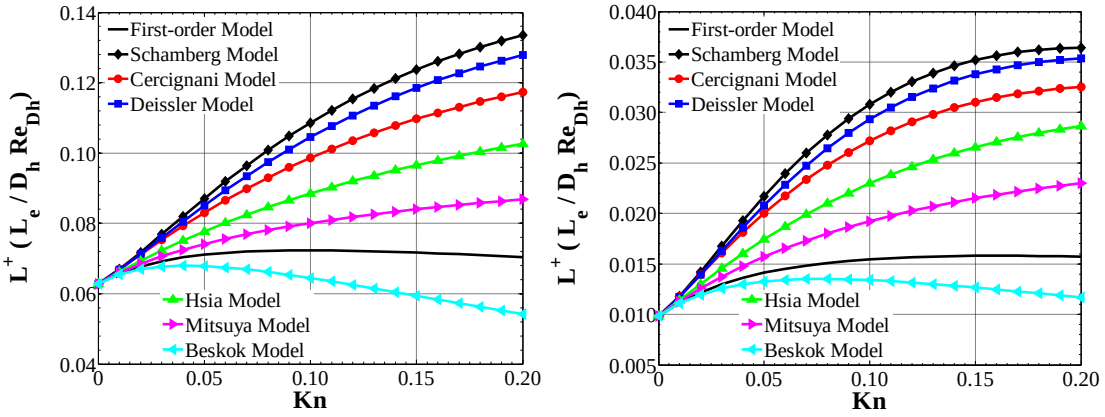

(a) Micro-tube **(b)** Slit channel

Figure 3.7: Variation of entrance length versus Kn using different slip models

the fully-developed profiles are similar for different models, the velocity profiles within the entrance region are quite different at some certain σ values which will result in quite different pressure drop and friction factor. In addition to these discussions, it is also clear that our model cannot capture the velocity overshoot as expected. However, as discussed earlier, especially for the cases with higher slip velocity, the overshoots would be very weak.

One parameter which is important to characterize the flow in the developing region is the entrance length, which can be defined as the required distance to downstream for which the centerline velocity reaches to 99% of the fully-developed

value. The effect of slip velocity and Kn on the entrance length for micro-tube and slit channel is illustrated in Figure 3.7. All models except Beskok predict slower velocity development as Kn increases. However, Beskok model predicts a reduction in entrance length after a certain Kn. It can be justified considering less friction on the solid walls in high Kn. On the other hand, high Kn results in a more flat fully developed parabola which may reduce the entrance length. One important observation is that for small Kn, more or less all the models predict similar entrance length which is in the vicinity of the value predicted by the first-order model. However, as Kn increases, different models predict different entrance length values. Although the velocity profiles in Figure 3.6 seems not to much different for different models, different models predict different behavior for the apparent friction factor. At this point, an important question raises, which slip model is better? The best way to verify is to compare the results against an experimental data. However, to obtain a velocity data within a micro-channel is still a challenging task even with today's hardware and software. To compare the slip-models, the fully-developed velocity profiles for different Kn is compared against the DSMC data, available in the literature. DSMC is a reliable method for micro-channel flows in the slip-flow and transition regime. The comparison is given for three different Kn numbers. For small Kn, the difference is indistinguishable, and all the models give the same velocity profile. For small Kn, even first-order model is accurate enough. As the Kn increases, the deviation starts. For $Kn = 0.1$ which can be recognized as the upper limit for the slip-flow regime, the first-order model deviates from the DSMC data. However, some high-order slip models deviates even more than the first-order model. The second-order model except Beskok model shift towards the left of the first-order model, but the Beskok model shifts towards the right side, and gives a closer result to DSMC data. The shifting behavior also explains the reason of the behavior observed in Figure 3.7. The velocity profile for $Kn = 0.5$ is also included in the figure which is in the transition regime. Although the validity of the NS equations is questionable at this limit, as discussed in the literature [48], Beskok model can predict the non-dimensional form of the velocity profile also at high Kn regime. With the appropriate coefficient, Beskok model gives the most reliable data in comparison with the DSMC data. Therefore, for the concentric

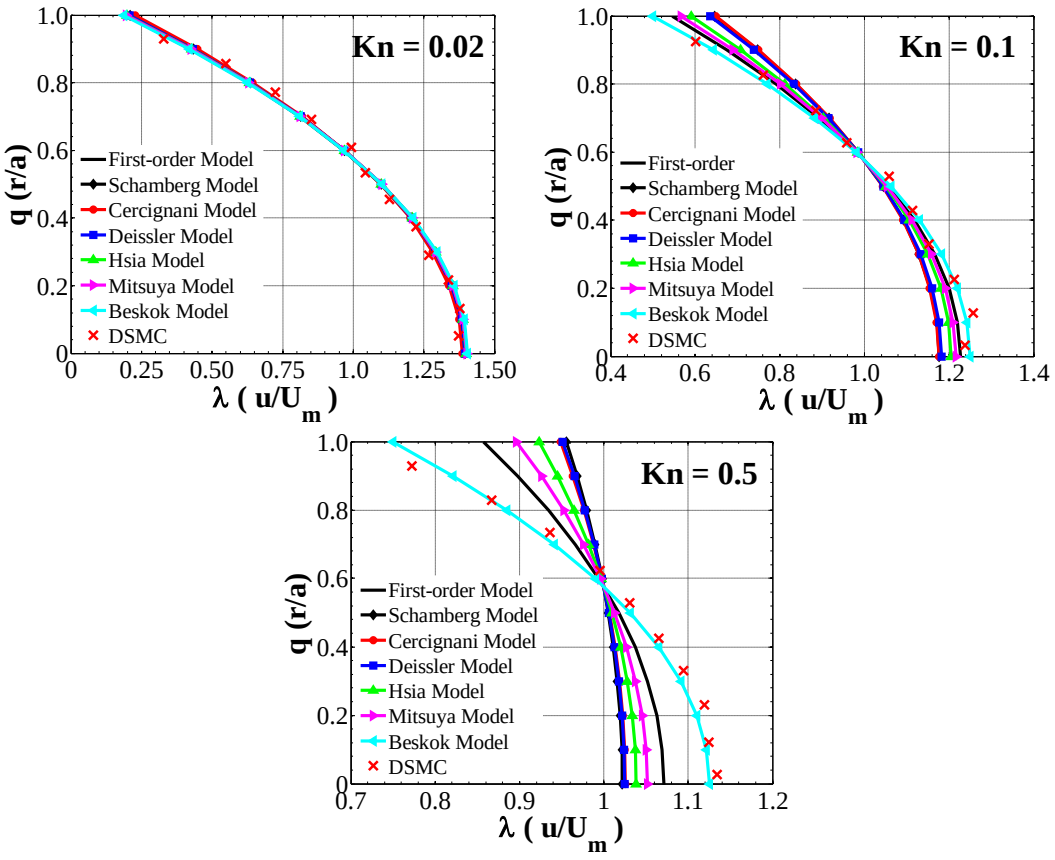

Figure 3.8: Comparison of velocity profile with DSMC solution for far distance downstream

annular micro-channel only the results of the general slip model is given.

The velocity profiles within the entrance region for a concentric annular micro-channel is shown in Figure 3.9 for $Kn = 0.01$ and radii ratio of $m = 0.5$. The figure shows the velocity development at different cross sections both using first-order model and general velocity-slip. The cross sections were chosen from the distance in the vicinity of inlet ($\sigma = 7.1 \times 10^{-5}$) to sufficiently far downstream ($\sigma = 1.7 \times 10^{-2}$) to ensure fully-developed velocity profile. Slip velocity on the inner and outer walls are different in magnitude. This issue is due to this fact that the velocity gradients are different on inner and outer walls which results in different slip velocities and shear stresses. In addition, different slip velocities on the solid walls cause nonsymmetrical distribution of velocity profile around the central core. Carefully looking at the figure, different slip velocity on the walls

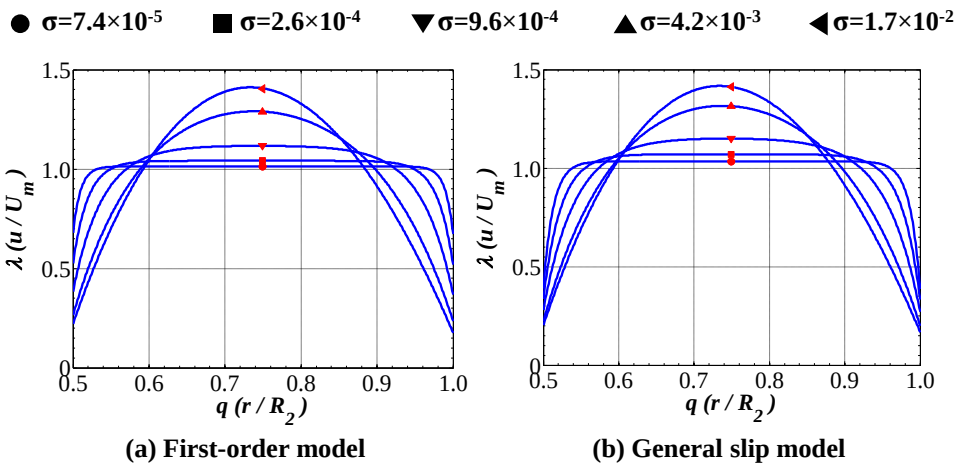

Figure 3.9: Developing velocity profile for $Kn = 0.01$ using first-order and general velocity-slip with radii ratio of m=0.5

predicted by different slip models can be observed. First-order model predicts higher slip velocity both on the inner and outer walls in comparison with general velocity-slip model. In the other words, at a same distance downstream, first-order model yields a more flat velocity profile than general slip model. This issue can also justifies faster velocity development predicted by general slip model. More importantly, discrepancy among two different slip models rises in the entrance region of channel and reduces drastically in the fully-developed region.

Figure 3.10 illustrates the entrance length with respect to Kn using first-order and general slip velocity for aconcentric annular micro-channel. General velocity-slip predicts faster velocity development or in the other words less entrance length in comparison with first-order model. This discrepancy reduces by increasing the radii ratio of channel. Furthermore, first-order yields a monotonic increase in the entrance length by increasing Kn, however, general slip model predicts a reduction after a certain Kn. This certain Kn is also a function of radii ratio and reduces as radii ratio increases. Moreover, the intensity of variation of entrance length is strongly dependent on radii ratio. For example, for the case of $m = 0.1$, entrance length varies considerably from $Kn = 0$ to $Kn = 0.2$, however, for $m = 0.8$ it is practically constant. This issue is also depicted in Figure 3.10 which shows the variation of entrance length versus Kn number for three different radii ratios. Entrance length or transition length which is an important parameter in

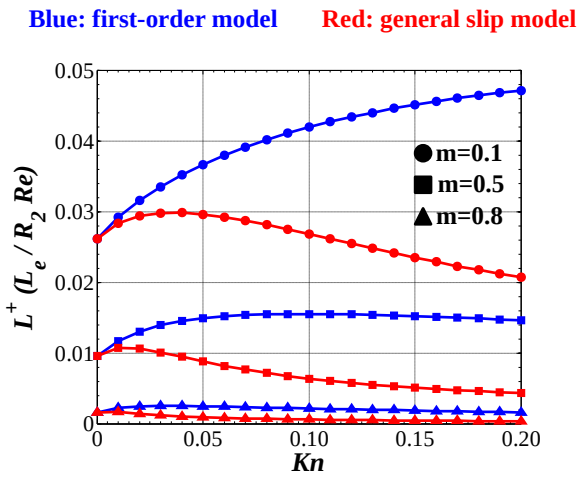

Figure 3.10: Variation of entrance length versus Kn using different slip models

engineering applications is defined as the required distance downstream in which the central core velocity value reaches %99 of the fully-developed value. Ergo, for annular channels with high radii ratio, the velocity can be considered as fully-developed for whole channel due to negligible entrance effects.

3.2.3 Pressure Drop and Friction Factor

Apparent friction factor which combines both frictional loss and velocity acceleration in the entrance region, is also one of the important parameters for engineering applications. Pressure drop in the form of apparent friction factor is shown in Figure 3.11 both for micro-tube and slit channel using different slip models and Kn. Apparent friction is also compared with available data in the literature for continuum gas flow and at the limit of the slip-flow regime. In continuum gas flow, the present model predicts apparent friction in good agreement with the data in literature. For $Kn = 0.10$, the data of [92], which uses a first-order slip, is also included for micro-tube and slit-channel. For slit-channel, the result for a rectangular channel with an aspect ration of 2.0 is included. The discrepancy between the present model and the data of [92] is due to the velocity overshoot. That is the reason, the discrepancy exists at the vicinity of the inlet, and the results converge to the same curve after a certain σ. It can be also seen that the

discrepancy diminishes as the Kn increases, and the curves merge at a location closer to the inlet.

The figure also shows a reduction in apparent friction with increased Kn which can be explained by considering the reduction of shear stresses on the solid walls. Similar to the entrance length results, Beskok model predicts the apparent friction higher than the that of the first-order model where all other high-order models predict the opposite. The high-order models deviate from the first-order model as Kn increases. Moreover, the asymptotic limit of the each curve is different. Again, the difference in this asymptotic value also increases with increasing Kn. Although the asymptotic values are close to each other, the apparent friction factor in the entrance region is quite different for different slip models. The apparent friction factor is more sensitive ot the used slip model for short micro-channels. After all, considering discussion on DSMC data, the most reliable data may be concluded as the that of Beskok model although a reliable experimental data is needed for further elaboration.

Apparent friction factor for a concentric annular micro-channel is presented in Figure 3.12 for different slip models, Kn and radii ratio. Variation of apparent friction along the channel from a cross-section sufficiently close to inlet to far distance downstream is illustrated. Reduction of apparent friction can be transparently observed as Kn increases. This issue can be justified considering less friction and shear stress on the solid walls for higher Kn numbers. In the case of continuum regime flow ($Kn = 0$), apparent friction has a monotonic increase by approaching to inlet, however, slip flow yields a virtually constant value in the vicinity of inlet. Three different regions can be recognized in the variation of apparent friction for the slip flow. The region sufficiently close to inlet with a constant value for the apparent friction, the transition region which velocity profile converts to fully-developed with a variable apparent friction and the fully-developed region which apparent friction again reaches to a constant value. Another important observation from the figure is the level of variation of apparent friction along the channel. As Kn number rises, the variation of apparent friction decreases drastically along the channel. For instance, in the case of continuum flow, the figure shows a significant variation in the apparent friction from inlet to

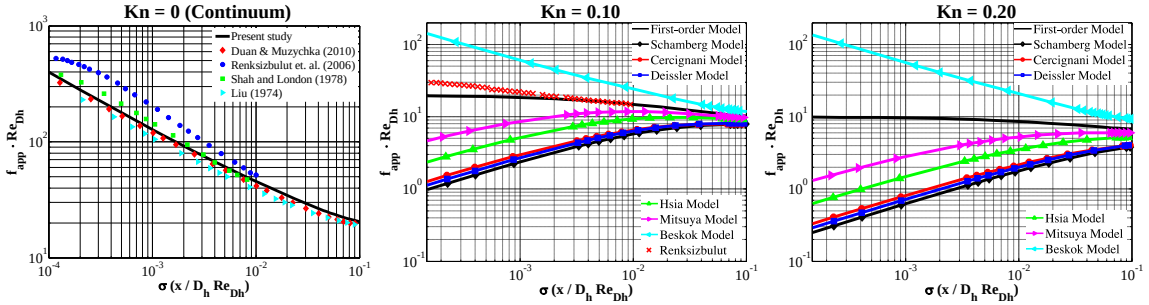

(a) Micro-tube

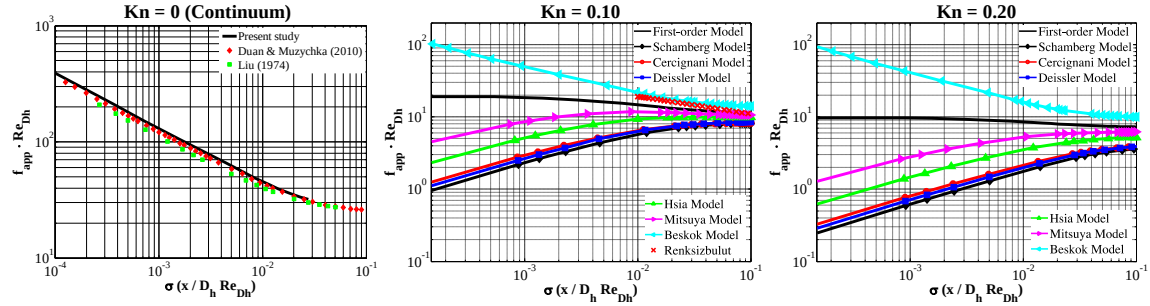

(b) Slit channel

Figure 3.11: Apparent friction factor using different models and different Kn

the fully-developed region, however, for the case of $Kn = 0.2$ apparent friction experiences a very smooth variation and it can be practically considered constant along the channel.

Higher radii ratio results in higher apparent friction both in entrance and fully-developed region. For low Kn, the apparent friction predicted by different slip models are virtually the same with a negligible deviation. As Kn increases, the deviation starts increasing. For instance, for the case of $Kn = 0.01$, a small deviation can be observed in the region close to inlet and reduces by approaching to fully-developed region. On the contrary, for the case of $Kn = 0.2$, a considerable discrepancy can be seen both in entrance and fully-developed region, however, it is more significant in the entrance region. Another interesting observation is the discrepancy among fully-developed apparent friction for different

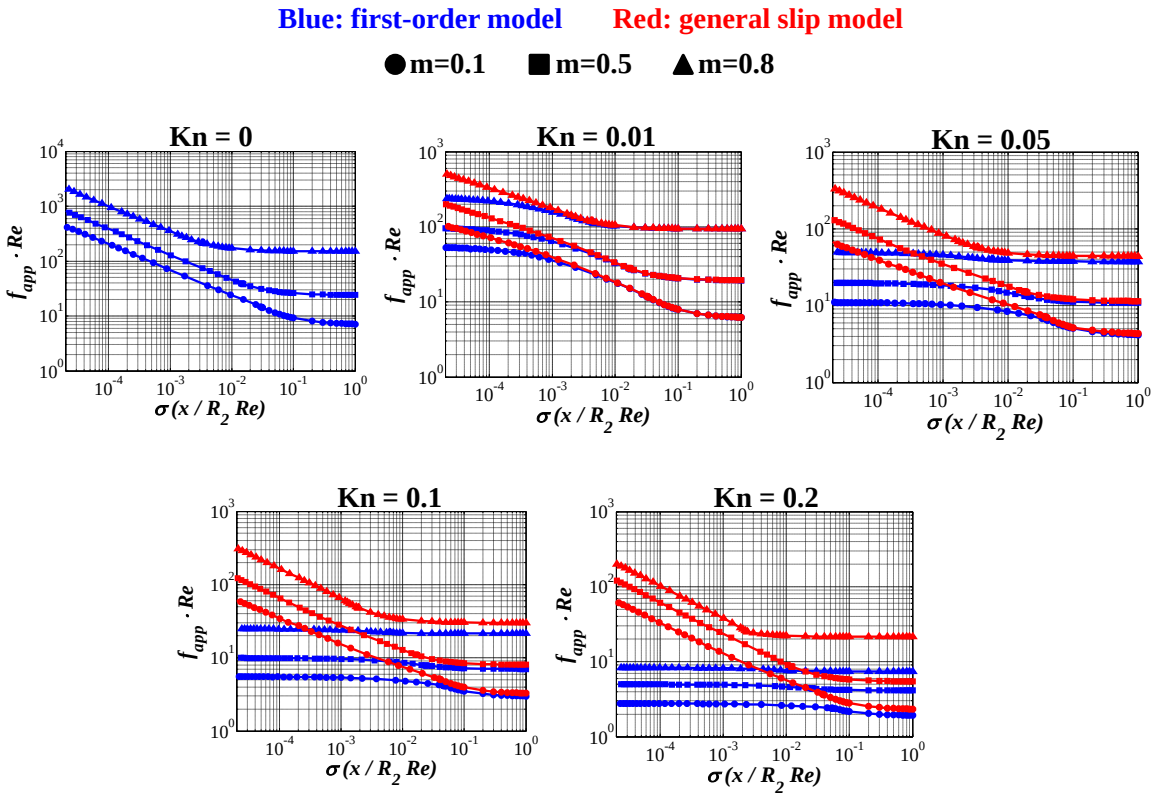

Figure 3.12: Apparent friction factor using different models, different Kn and different radii ratio

radii ratios predicted by different slip models. For higher radii ratios, the discrepancy among fully-developed values is quit higher than lower radii ratios. Unlike first-order model which yields a constant value for apparent friction in he vicinity of inlet, general slip model shows a monotonic increasing behavior by approaching to inlet.

To facilitate the exploitation of the data in the present study for engineering applications, we propose a relation for the non-dimensional group $f_{app} \cdot Re_{D_h}$ for micro-tube and slit channel as a function of σ as:

$$f_{app} \cdot Re_{D_h} = A\sigma^B + C \tag{3.56}$$

where coefficients A, B and C can be calculated using curve fitting techniques for different Kn with a ($R^2 > 0.999$). It is also observed that the coefficients for

micro-tube and slit channel can be obtained a relation in the following form:

$$\begin{bmatrix} A \\ B \\ C \end{bmatrix} = D_1 \exp\left(D_2 \times \mathrm{Kn}\right) + D_3 \exp\left(D_4 \times \mathrm{Kn}\right) \tag{3.57}$$

where the coefficients D_1 through D_4 are calculated using curve fit techniques with a ($R^2 > 0.999$). The coefficients are tabulated in Tables 3.1 and 3.2.

Table 3.1: Coefficients of A, B and C for micro-tube

	D_1	D_2	D_3	D_4
A	5.462	−43.16	2.151	−0.6728
B	−0.4785	0.0497	0.1151	−28.38
C	9.394	−5.593	−10.43	−63.48

Table 3.2: Coefficients of A, B and C for slit channel

	D_1	D_2	D_3	D_4
A	6.541	−32.25	1.846	−2.216
B	−0.6140	−0.6378	0.2743	−8.101
C	13.33	−4.670	−12.53	−40.20

3.3 Concluding Remarks

Measurement of different flow parameters to understand fluid physics at micro-scale is still challenging. Therefore, analytical and numerical models serve as a basis for the fundamental understanding of the phenomena. Present study presents an analytical solution for a 2D incompressible, isothermal flow in a developing region of a micro-channel based on Langhaar's linearization. The analytical model is verified for the flows in macro-scale, and validity of the certain assumptions have been discussed. Hydrodynamic entrance length and apparent friction factor which are the quantities of interest for many engineering calculations are presented. To extend the applicability of the model, different second-order models together with the general velocity-slip boundary condition [2] are included in the analysis. To discuss the validity of the several slip models, the velocity profiles for the fully-developed flow are compared against the available DSMC data. It is

found that the Beskok model gives the closest result to the DSMC data. In addition, Beskok model predicts apparent friction factor and entrance length quite differently compared to the other slip models. A correlation for the prediction of non-dimensional group, $f_{app} \cdot Re_{D_h}$, is proposed with a quite high $R - square$ value. The analytical nature of the presented model enables the implementation of Beskok general slip-model with high accuracy, and a fast evaluation of the velocity field which can be used for the exploration of the combined entrance heat transfer problems for micro-channels.

Chapter 4

Summary and Outlook

In this thesis, the fluid flow both liquid and gas modeling was performed inside the microchannels. As the first part of the thesis, rarefied gas flow was analytically studied at the hydrodynamic entrance region of slit, circular and concentric annular microchannels. The governing equations of motion including Navier-Stokes and continuity equation for an isothermal incompressible gas flow were linearized using Langhaar linearization method [55]. Slip boundary condition using first order, second order and Beskok model with high accuracy were implemented in the derivation of closed form velocity profile. Finally, pressure drop, entrance length and apparent friction factor which are the quantities of interest for engineering applications were derived and compared for different slip models.

In the second part of the thesis, the simulation and modeling of particle focusing was carried out using inertial microfluidics for both straight and spiral microchannels. In inertial microfluidics, due to the existence of inertial lift force field at the lateral direction of the channel, randomly distributed particles at the inlet of channel occupy several equilibrium positions after some distance downstream which is known as inertial migration. Moreover, in curved microchannels, due to the introduction of channel curvature, centrifugal effects will come into picture. The effect of centrifugal forces is the velocity mismatch for the fluid element in the vicinity of inner and our walls of channel. This velocity mismatch causes a centrifugal pressure difference which consequently creates two symmetric

counter rotating vortices at the cross section of channel known as secondary or Dean flow. Dean flow changes the equilibrium positions of particle obtained in straight channel and has a substantial role in size based particle separation.

To track the particles, the flow field inside the microchannel was first modeled in COMSOL mutiphysics commercial software at the absence of particles. Then, the data was utilized to find the flow velocity at a given point. A Lagrangian discrete phase model was implemented to track the particles. The computational was developed for general case and then formulations were stated for our specific case. In this model, Stokes drag expression together with inertial lift taken from a recent research study [42,43] were implemented. The computational model was first verified with experimental results from literature for spiral channel [75] and the validity of the developed computational model was confirmed. Finally, using our model, different simulations for different channel geometries such as straight and spiral with different cross-sections were carried out. Finally, experimental investigations were performed for high aspect ratio spiral channel and the results were compared with developed computational model predictions.

As future research directions for these topics, different type of suggestions can be made. For the gas flow, due to the rarefaction effect, incompressible assumption of gas behaviour can be different from the realistic model. To give a more realistic model, the compressibility consideration can be implemented into the governing equations. In such a case, the density of gas will be a function of pressure and temperature. Using isothermal assumption, the role of temperature on the gas density can be neglected and the density becomes a function of pressure. For simplification, ideal gas assumption can be made and equation of state for ideal gas which relates the pressure to the gas density can be exploited. It is worth mentioning that Navier-Stokes equations need to be written for a compressible gas which additional terms will come into picture. Moreover, the same analyses can be performed to study the entrance region of rectangular microchannels. Rectangular microchannels are the most common used channel geometries in microfluidics due to simplicity of micro-fabrication process. Ergo, deriving an analytical solution for the velocity and also apparent friction factor can be very useful specially for combined entrance problems.

In inertial microfluidics, the separation of sub micron particles can be appealing and interesting. Since nano-particle dimension can resemble different types of viruses, it can have a great application in biomedical and biological fields. It is worth mentioning that for nano particles due to the small size of particles, Brownian motion or diffusion of particles has to be taken into consideration for the simulation. To implement the effect of diffusion into the computational model, the Brownian force must be added to the force balance relation of particles. Due to the random nature of Brownian motion of particles, it can be deduced that inclusion of Brownian force into the force balance relations may be cumbersome or problematic. On the other hand, focusing of nano-particles in a microchannel can virtually be considered as impossible using inertial microfluidics and newtonian fluids. For this purpose, recently by using visco-elastic non-Newtonian fluids, focusing of nano-particles in microchannels has been achieved. As a future research work, it can be expected to develop a computational model for prediction of particle motion in inertial non-Newtonian fluids. In my point of view, this research can be very hard and cumbersome due to complicated nature and behaviour of non-Newtonian fluids.

Bibliography

[1] B. Cetin, M. B. Ozer, and M. E. Solmaz. Microfluidic bio-particle manipulation for biotechnology. *Biochem. Eng. J.*, 92:63–82, 2014.

[2] A. Beskok and G. E. Karniadakis. Report: A model for flows in channels, pipes, and ducts at micro and nano scales. *Microscale Thermophys. Eng.*, 3(1):43–77, 1999.

[3] K. H. Kang, X. Xuan, Y. Kang, and D. Li. Effects of DC-dielectrophoretic force on particle trajectories in microchannels. *J. Applied Physics*, 99(064702):1–8, 2006.

[4] Y. Kang, B. Cetin, Z. Wu, and D. Li. Continuous particle separation with localized AC-dielectrophoresis using embedded electrodes and an insulating hurdle. *Electrochim. Acta*, 54:1715–1720, 2009.

[5] B. Cetin, Y. Kang, Z. Wu, and D. Li. Continuous particle separation by size via AC-dielectrophoresis using a lab-on-a-chip device with 3D electrodes. *Electrophoresis*, 30:766–772, 2009.

[6] B. Cetin and D. Li. Continuous particle separation based on electrical properties using AC-dielectrophoresis. *Electrophoresis*, 30:3124–3133, 2009.

[7] B. Cetin and D. Li. Lab-on-a-chip device for continuous particle and cell separation based on electrical properties via AC-dielectrophoresis. *Electrophoresis*, 31:3035–3043, 2010.

[8] S. Zeinali, B. Cetin, S. Oliaei, and Y. Karpat. Fabrication of continuous flow microfluidic device with 3D electrode structures for high throughput DEP

applications using mechanical machining. *Electrophoresis*, 36:1432–1442, 2015.

[9] B. Cetin, S. D. Oner, and B. Baranoglu. Modeling of dielectrophoretic particle motion: Point particle vs finite-sized particle. *Electrophoresis*, In press, 2017.

[10] B. Cetin, S. Buyukkocak, S. Zeinali, and M. B. Ozer. Simulation of an integrated microfluidic device for bioparticle wash, separation and concentration. In *ASME 4^{th} International Conference on Micro/Nanoscale Heat and Mass Transfer*, number 22181, 11–14 December 2013.

[11] S. Buyukkocak, M. B. Ozer, and B. Cetin. Numerical modeling of ultrasonic particle manipulation for microfluidic applications. *Microfluid Nanofluid*, 17(6):1025–1037, 2014.

[12] Y. Ai, S. W. Joo, Y. Jiang, X. Xuan, and S. Qian. Transient electrophoretic motion of a charged particle through a converging-diverging microchannel: Effect of direct current-deielectrophoretic force. *Electrophoresis*, 30:2499–2506, 2009.

[13] Y. Ai, A. Beskok, D. T. Gauthier, S. W. Joo, and S. Qiani. DC electrokinetic transport of cylindrical cells in straight microchannels. *Biomicrofluidics*, 3(4):044110, 2009.

[14] Y. Ai and S. Qian. DC-dielectrophoretic particle-particle interactions and their relative motions. *J. Colloid Interf. Sci.*, 346:448–454, 2010.

[15] Y. Ai, Z. Zeng, and S. Qian. Direct numerical simulation of ac dielectrophoretic particle-particle interactive motions. *J. Colloid Interf. Sci.*, 417:72–79, 2014.

[16] S. Kang. Direct numerical simulations on the electrophoretic motion of multiple charged particles using an immersed boundary method. *Comput. Fluids*, 73:10–23, 2013.

[17] S. Kang. Dielectrophoretic motion of two particles with diverse sets of the electric conductivity under a uniform electric field. *Comput. Fluids*, 105:231–243, 2014.

[18] S. Kang. Dielectrophoretic motions of multiple particles under an alternating-current electric field. *Eur. J. Mech. B-Fluid*, 54:53–68, 2015.

[19] Y. Shi, Z. Yu, and X. Shao. Combination of direct-forcing fictitious domain method and sharp interface method for dielectrophoresis of particles. *Particuology*, 8(4):351 – 359, 2010.

[20] Y. Shi, Z. Yu, and X. Shao. Combination of the direct-forcing fictitious domain method and the sharp interface method for the three-dimensional dielectrophoresis of particles. *Powder Technol.*, 210(1):52 – 59, 2011.

[21] D. L. House and H. Luo. Electrophoretic mobility of a colloidal cylinder between two parallel walls. *Eng. Anal. Bound. Elem.*, 34(5):471 – 476, 2010.

[22] D.L. House, H. Luo, and S. Chang. Numerical study on dielectrophoretic chaining of two ellipsoidal particles. *J. Colloid Interf. Sci*, 374(1):141 – 149, 2012.

[23] Z. Karakaya, B. Baranoglu, B. Cetin, and A. Yazici. A parallel boundary element formulation for tracking multiple particle trajectories in Stoke's flow for microfluidic applications. *CMES-Computer Modeling in Engineering and Science*, 104:227–249, 2015.

[24] M. E.Solmaz, B. Cetin, B. Baranoglu, M. Serhathoglu, and N. Biyikli. Boundary element method for optical force calibration in microfluidic dual-beam optical trap. *Proc. SPIE*, 9548:95481D–95481D–8, 2015.

[25] B. Cetin and B. Baranoglu. Boundary-element method in microfluidics. In Dongqing Li, editor, *Encyclopedia of Microfluidics and Nanofluidics*, pages 202–213. Springer US, Boston, MA, 2 edition, 2015.

[26] D. Di Carlo. Inertial microfluidics. *Lab Chip*, 9(21):3038–3046, 2009.

[27] B. Chun and A. J. C. Ladd. Inertial migration of neutrally buoyant particles in a square duct: An investigation of multiple equilibrium positions. *Physics of Fluids*, 18(3):031704, 2006.

[28] D. Di Carlo, J. F. Edd, K. J. Humphry, H. A. Stoneand, and M. Toner. Particle segregation and dynamics in confined flows. *Physical Review Letters*, 102(9):094503, 2009.

[29] W. Lee, H. Amini, HA. Stone, and D. Di Carlo. Dynamic self-assembly and control of microfluidic particle crystals. *Proceedings of the National Academy of Sciences*, 107(52):22413–22418, 2010.

[30] A. A. S. Bhagat, S. S. Kuntaegowdanahalli, N. Kaval, C. J. Seliskar, and I. Papautsky. Inertial microfluidics for sheath-less high-throughput flow cytometry. *Biomedical Microdevices*, 12(2):187–195, 2010.

[31] A. J. Mach and D. Di Carlo. Continuous scalable blood filtration device using inertial microfluidics. *Biotechnology and bioengineering*, 107(2):302–311, 2010.

[32] S. C. Hur, H. T. K. Tse, and D. Di Carlo. Sheathless inertial cell ordering for extreme throughput flow cytometry. *Lab on a Chip*, 10(3):274–280, 2010.

[33] H. Amini, E. Sollier, W. M. Weaver, and D. Di Carlo. Intrinsic particle-induced lateral transport in microchannels. *Proceedings of the National Academy of Sciences*, 109(29):11593–11598, 2012.

[34] S. C. Hur, T. Z. Brinckerhoff, C. M. Walthers, J. C. Y. Dunn, and D. Di Carlo. Label-free enrichment of adrenal cortical progenitor cells using inertial microfluidics. *PLoS One*, 7(10):e46550, 2012.

[35] J. Sun, M. Li, C. Liu, Y. Zhang, D. Liu, W. Liu, G. Huand, and X. Jiang. Double spiral microchannel for label-free tumor cell separation and enrichment. *Lab on a chip*, 12(20):3952–3960, 2012.

[36] H. W. Hou, M. E. Warkiani, B. L. Khoo, Z. R. Li, R. A. Soo, D. S. W. Tan, W. T. Lim, J. Han, A. A. S. Bhagat, and c. T. Lim. Isolation and retrieval

of circulating tumor cells using centrifugal forces. *Scientific Reports*, 3:1259 EP –, 02 2013.

[37] M. E. Warkiani, G. Guan, K. B. Luan, W. C. Lee, A. A. S. Bhagat, P. K. Chaudhuri, D. S. W. Tan, W. T. Lim, S. C. Lee, P. C. Y. Chen, et al. Slanted spiral microfluidics for the ultra-fast, label-free isolation of circulating tumor cells. *Lab Chip*, 14(1):128–137, 2014.

[38] M. Dhar, J. Wong, A. Karimi, J. Che, C. Renier, M. Matsumoto, M. Triboulet, E. B. Garon, J. W. Goldman, M. B. Rettig, S. S. Jeffrey, R. P. Kulkarni, E. Sollier, and D. Di Carlo. High efficiency vortex trapping of circulating tumor cells. *Biomicrofluidics*, 9(6):064116, 2015.

[39] C. Liu, G. Hu, X. Jiang, and J. Sun. Inertial focusing of spherical particles in rectangular microchannels over a wide range of reynolds numbers. *Lab on a Chip*, 15(4):1168–1177, 2015.

[40] K. Hood, S. Kahkeshani, D. Di Carlo, and M. Roper. Direct measurement of particle inertial migration in rectangular microchannels. *Lab Chip*, 16:2840–2850, 2016.

[41] M. E. Warkiani, B. L. Khoo, L. Wu, A. K. P. Tay, A. A. S. Bhagat, J. Han, and C. T. Lim. Ultra-fast, label-free isolation of circulating tumor cells from blood using spiral microfluidics. *Nat. Protocols*, 11(1):134–148, 01 2016.

[42] K. Hood, S. Lee, and M. Roper. Inertial migration of a rigid sphere in three-dimensional poiseuille flow. *Journal of Fluid Mechanics*, 765:452–479, 2015.

[43] K. Hood, S. Kahkeshani, D. Di Carlo, , and M. Roper. Direct measurement of particle inertial migration in rectangular microchannels. *arXiv preprint arXiv:1509.01643*, 2015.

[44] E. S. Asmolov. The inertial lift on a spherical particle in a plane poiseuille flow at large channel reynolds number. *Journal of Fluid Mechanics*, 381:63–87, 1999.

[45] M. Gad el Hak. The fluid mechanics of microdevices—the freeman scholar lecture. *Journal of Fluids Engineering*, 121(1):5–33, 03 1999.

[46] S. Colin. Rarefaction and compressibility effects on steady and transient gas flows in microchannels. *Microfluidics and Nanofluidics*, 1(3):268–279, 2005.

[47] A. Agrawal. A comprehensive review on gas flow in microchannels. *Int. J. Micro-Nano Scale Transport*, 2(1):1–40, 2011.

[48] G. E. Karniadakis, A. Beskok, and N. Aluru. *Microflows and nanoflows: fundamentals and simulation*, volume 29. Springer Science & Business Media, 2006.

[49] N. Dongari, A. Agrawal, and A. Agrawal. Analytical solution of gaseous slip flow in long microchannels. *Int. J. Heat Mass Transfer*, 50(17–18):3411–3421, 2007.

[50] W. M. Zhang, G. Meng, and X. Wei. A review on slip models for gas microflows. *Microfluid. Nanofluid.*, 13(6):845–882, 2012.

[51] S. Colin, P. Lalonde, and R. Caen. Validation of a second-order slip flow model in rectangular microchannels. *Heat Transfer Engineering*, 25(3):23–30, 2004.

[52] Z. Duan. Second-order gaseous slip flow models in long circular and noncircular microchannels and nanochannels. *Microfluid. Nanofluid.*, 12(5):805–820, 2012.

[53] H. Xue and Q. Fan. A new analytic solution of the navier-stokes equations for microchannel flows. *Microscale Thermophysical Engineering*, 4(2):125–143, 2000.

[54] M. Gad el Hak. The fluid mechanics of microdevices-the freeman scholar lecture. *Transactions-American Society of Mechanical Engineers Journal of FLUIDS Engineering*, 121:5–33, 1999.

[55] H. L. Langhaar. Steady flow in the transition length of a straight tube. *J. Appl. Mech.*, 9(2):55–58, 1942.

[56] B. Çetin and D. Li. Dielectrophoresis in microfluidics technology. *Electrophoresis*, 32(18):2410–2427, 2011.

[57] T. P. Forbes and S. P. Forry. Microfluidic magnetophoretic separations of immunomagnetically labeled rare mammalian cells. *Lab on a Chip*, 12(8):1471–1479, 2012.

[58] B. Cetin, M. B. Ozer, E. Cagatay, and S. Buyukkocak. An integrated acoustic and dielec- trophoretic particle manipulation in a microfluidic device for particle wash and separation fabricated by mechanical machining. *Biomicrofluidics*, 10(014112), 2016.

[59] Z. Wang and J. Zhe. Recent advances in particle and droplet manipulation for lab-on-a-chip devices based on surface acoustic waves. *Lab on a Chip*, 11(7):1280–1285, 2011.

[60] D. G. Grier. A revolution in optical manipulation. *Nature*, 424(6950):810–816, 2003.

[61] M. Yamada, M. Nakashima, and M. Seki. Pinched flow fractionation: continuous size separation of particles utilizing a laminar flow profile in a pinched microchannel. *Analytical chemistry*, 76(18):5465–5471, 2004.

[62] L. R. Huang, E.C. Cox, R. H. Austin, and J. C. Sturm. Continuous particle separation through deterministic lateral displacement. *Science*, 304(5673):987–990, 2004.

[63] G Segre. Radial particle displacements in poiseuille flow of suspensions. *Nature*, 189:209–210, 1961.

[64] G Segre and A Silberberg. Behaviour of macroscopic rigid spheres in poiseuille flow part 2. experimental results and interpretation. *Journal of Fluid Mechanics*, 14(01):136–157, 1962.

[65] Jean-Philippe Matas, Jeffrey F Morris, and Élisabeth Guazzelli. Inertial migration of rigid spherical particles in poiseuille flow. *Journal of Fluid Mechanics*, 515:171–195, 2004.

[66] M. JP, M. JF, and E. Guazzelli. Lateral forces on a sphere. *Oil & gas science and technology*, 59(1):59–70, 2004.

[67] SI. Rubinow and J. B. Keller. The transverse force on a spinning sphere moving in a viscous fluid. *Journal of Fluid Mechanics*, 11(03):447–459, 1961.

[68] P. G. T. Saffman. The lift on a small sphere in a slow shear flow. *Journal of fluid mechanics*, 22(02):385–400, 1965.

[69] N. Nakagawa, T. Yabu, R.Otomo, A. Kase, M. Makino, T. Itano, and M. Sugihara-Seki. Inertial migration of a spherical particle in laminar square channel flows from low to high reynolds numbers. *J. Fluid Mech*, 779:776, 2015.

[70] C. Lium, C. Xue, J. Sun, and G. Hu. A generalized formula for inertial lift on a sphere in microchannels. *Lab on a Chip*, 16(5):884–892, 2016.

[71] Y. S. Choi, K. W. Seo, and S. J. Lee. Lateral and cross-lateral focusing of spherical particles in a square microchannel. *Lab on a Chip*, 11(3):460–465, 2011.

[72] J. Zhou and I. Papautsky. Fundamentals of inertial focusing in microchannels. *Lab on a Chip*, 13(6):1121–1132, 2013.

[73] A. J. Chung, D. R. Gossett, and D. Di Carlo. Three dimensional, sheathless, and high-throughput microparticle inertial focusing through geometry-induced secondary flows. *Small*, 9(5):685–690, 2013.

[74] MG. Lee, S. Choi, and J.K. Park. Inertial separation in a contraction–expansion array microchannel. *Journal of Chromatography A*, 1218(27):4138–4143, 2011.

[75] A. A. S. Bhagat, S. S. Kuntaegowdanahalli, and I. Papautsky. Continuous particle separation in spiral microchannels using dean flows and differential migration. *Lab Chip*, 8(11):1906–1914, 2008.

[76] S. S. Kuntaegowdanahalli, A. A. S. Bhagat, G. Kumar, and I. Papautsky. Inertial microfluidics for continuous particle separation in spiral microchannels. *Lab Chip*, 9(20):2973–2980, 2009.

[77] J. Sun, C. Liu, M. Li, J. Wang, Y. Xianyu, G. Hu, and Xingyu Jiang. Size-based hydrodynamic rare tumor cell separation in curved microfluidic channels. *Biomicrofluidics*, 7(1):011802, 2013.

[78] L. Wu, G. Guan, H. W. Hou, A. A. S. Bhagat, and J. Han. Separation of leukocytes from blood using spiral channel with trapezoid cross-section. *Analytical chemistry*, 84(21):9324–9331, 2012.

[79] G. Guan, L. Wu, A. A. S. Bhagat, Z. Li, P. C. Y. Chen, S. Chao, C. J. Ong, and J. Han. Spiral microchannel with rectangular and trapezoidal cross-sections for size based particle separation. *Scientific reports*, 3:1475, 2013.

[80] A. Özbey, M. Karimzadehkhouei, S. Akgönül, D. Gozuacik, and A. Koşar. Inertial focusing of microparticles in curvilinear microchannels. *Scientific Reports*, 6:38809, 2016.

[81] S. A. Morsi and A. J. Alexander. An investigation of particle trajectories in two-phase flow systems. *Journal of Fluid Mechanics*, 55(02):193–208, 1972.

[82] D. J. Guckenberger, T. E. de Groot, A. M. D. Wan, D. J. Beebe, and E. W. K. Young. Micromilling: a method for ultra-rapid prototyping of plastic microfluidic devices. *Lab Chip*, 15:2364–2378, 2015.

[83] K. Sugioka, J. Xu, D. Wu, Y. Hanada, Z. Wang, Y. Cheng, and K. Midorikawa. Femtosecond laser 3d micromachining: a powerful tool for the fabrication of microfluidic, optofluidic, and electrofluidic devices based on glass. *Lab Chip*, 14:3447–3458, 2014.

[84] H. Kalaycioglu C. Kerse, P. Elahi, B. Cetin, D. K. Kesim, O. Akcaalan, S. Yavas, M. D. Asik, B. Oktem, H. Hoogland, R. Holzwarth, and F. O. Ilday. Ablation-cooled material removal with ultrafast bursts of pulses. *Nature*, 537:84–88, 07 2016.

[85] M. Yaman, T. Khudiyev, E. Ozgur, M. Kanik, O. Aktas, E. O. Ozgur, H. Deniz, E. Korkut, and M. Bayindir. Arrays of indefinitely long uniform nanowires and nanotubes. *Nature Materials*, 10(7):494–501, 2011.

[86] E. B. Arkilic, M. A. Schmidt, and K. S. Breuer. Gaseous slip flow in long microchannels. *J. Microelectromech. S.*, 6(2):167–178, 1997.

[87] Y. Zohar, S. Y. K. Lee, W. Y. Lee, L. Jiang, and P. Tong. Subsonic gas flow in a straight and uniform microchannel. *J. Fluid Mech.*, 472:125–151, 2002.

[88] A. Gat, I. Frankel, and D. Weihs. Gas flows through constricted shallow micro-channels. *J. Fluid Mech.*, 602:427–442, 2008.

[89] E. M. Sparrow, S. H.Lin, and T. S.Lundgren. Flow development in the hydrodynamic entrance region of tubes and ducts. *Phys. Fluids*, 7(3):338–347, 1964.

[90] S. T. McComas. Hydrodynamic entrance lengths for ducts of arbitrary cross section. *J. Basic Eng.*, 89(4):847–850, 1967.

[91] R. Y. Chen. Flow in the entrance region at low reynolds numbers. *J. Fluids Eng.*, 95(1):153–158, 1973.

[92] M. Renksizbulut, H. Niazmand, and G. Tercan. Slip-flow and heat transfer in rectangular microchannels with constant wall temperature. *Int. J. Thermal Sciences*, 45(9):870–881, 2006.

[93] Z. Duan and Y. S. Muzychka. Slip flow in the hydrodynamic entrance region of circular and noncircular microchannels. *J. Fluids Eng.*, 132(1):011201, 2010.

[94] M. Darbandi and G. E. Schneider. Numerical study of the flow behavior in the uniform velocity entry flow problem. *Numerical Heat Transfer, Part A: Applications*, 34(5):479–494, 1998.

[95] C. Nouar, M. Ouldrouis, A. Salem, and J. Legrand. Developing laminar flow in the entrance region of annuli—review and extension of standard resolution methods for the hydrodynamic problem. *International journal of engineering science*, 33(10):1517–1534, 1995.

[96] N. S. Berman and V. A. Santos. Laminar velocity profiles in developing flows using a laser doppler technique. *AIChE J.*, 15:323–327, 1969.

[97] A. Molki, L. Khezzar, and A. Goharzadeh. Measurement of fluid velocity development in laminar pipe flow using laser doppler velocimetry. *Europ. J. Physics*, 34(5):1127, 2013.

[98] R. K.Shah and A. L. London. *Forced Convection in Ducts: A source book for compact heat exchanger Analytical Data*. Academic Press, 1978.

[99] E. SUGINO. Velocity distribution and pressure drop in the laminar inlet of a pipe with annular space. *Bulletin of JSME*, 5(20):651–655, 1962.

[100] J. C. Harley, Y. Huang, H. H. Bau, and J. N. Zemel. Gas flow in micro-channels. *J. Fluid Mech.*, 284:257–274, 1995.

[101] E. B. Arkilic, K. S. Breuer, and M. A. Schmidt. Mass flow and tangential momentum accommodation in silicon micromachined channels. *J. Fluid Mech.*, 437:29–43, 2001.

[102] B. Cetin, A.G. Yazicioglu, and S. Kakac. Fluid flow in microtubes with axial conduction including rarefaction and viscous dissipation. *Int. Comm. Heat and Mass Transfer*, 35:535–544, 2008.

[103] B. Cetin, A.G. Yazicioglu, and S. Kakac. Slip-flow heat transfer in microtubes with axial conduction and viscous dissipation–An extended Graetz problem. *Int. J. Thermal Sciences*, 48:1673–1678, 2009.

[104] B. Cetin and O. Bayer. Evaluation of Nusselt number for a flow in a microtube using second-order slip model. *Thermal Sciences*, 15 Suppl. 1:103–109, 2011.

[105] L. S. Han. Hydrodynamic entrance lengths for incompressible laminar flow in rectangular ducts. *J. Appl. Mech.*, 27(3):403–409, 09 1960.